Dipl.-Ing. Benjamin Marussig

Seamless Integration of Design and Analysis through Boundary Integral Equations

DISSERTATION

zur Erlangung des akademischen Grades

Doktor der technischen Wissenschaften

eingereicht an der

Technischen Universität Graz

Gutachter

Prof. Dipl.-Ing. Dr.techn. Gernot Beer,
Institut für Baustatik, Technische Universität Graz

Prof. Dr.-Ing. Kai-Uwe Bletzinger,
Lehrstuhl für Statik, Technische Universität München

Prof. Dr.-Ing. habil. Thomas-Peter Fries,
Institut für Baustatik, Technische Universität Graz

Graz, September 2015

EIDESSTATTLICHE ERKLÄRUNG

Ich erkläre an Eides statt, dass ich die vorliegende Arbeit selbstständig verfasst, andere als die angegebenen Quellen/Hilfsmittel nicht benutzt, und die den benutzten Quellen wörtlich und inhaltlich entnommenen Stellen als solche kenntlich gemacht habe. Das in TUGRAZonline hochgeladene Textdokument ist mit der vorliegenden Dissertation identisch.

Datum

Unterschrift

Abstract

The direct integration of Computer Aided Geometric Design (CAGD) models into a numerical simulation improves the accuracy of the geometrical representation of the problem as well as the efficiency of the overall analysis process. In this dissertation, the complementary features of isogeometric analysis and boundary integral equations are combined to obtain a coalescence of design and analysis. Following the isogeometric concept, the functions used by CAGD are employed for the simulation. The advantage of boundary integral equations is that the related numerical methods, namely the Nyström and boundary element method, are based on a boundary representation. This holds equally true for the most popular CAGD models in engineering design. An independent field approximation is applied to obtain a more flexible and efficient formulation. In addition, a procedure is presented which allows a stable analysis of trimmed geometries and a straightforward positioning of related collocation points. The convergence behavior of the suggested numerical methods is studied for problems governed by the Laplace and Lamé-Navier equations. Several practical examples demonstrate the characteristics and benefits of the proposed approach as well as its applicability to complex geometries. In particular, independent field approximation improves the computational efficiency and reduces the storage requirements without any loss of accuracy. The flexibility of the isogeometric Nyström method is shown by performing local refinement of tensor product surfaces. The proposed methodology permits a seamless integration of the most common design models into an analysis of linear potential and elasticity problems.

Kurzfassung

Das direkte Einbinden von Computer Aided Geometric Design (CAGD) Modellen in eine numerische Simulation verbessert sowohl die Genauigkeit der Geometriedarstellung als auch die Effizienz des gesamten Simulationsprozesses. In dieser Arbeit werden die isogeometrische Analyse und die Randintegralgleichungen miteinander vereint, um eine nahtlose Überführung vom CAGD Modellen in eine Simulation zu gewährleisten. Die grundlegende Idee der isogeometrischen Analyse besteht darin, die Funktionen des CAGD Modells auch für die Simulation anzuwenden. Numerische Methoden wie die Nyström- und Randelementmethode, welche auf Randintegralgleichungen basieren, bieten den Vorteil, dass sie lediglich die Darstellung der Oberfläche eines Problems benötigen. Dies trifft auch auf die meisten CAGD Modelle zu. Zusätzlich werden die verschiedenen Feldgrößen unabhängig voneinander approximiert, um die Effizienz und Flexibilität der Methode zu erhöhen. Außerdem wird ein Verfahren vorgestellt, welches eine Analyse mit geschnittenen Geometrien ermöglicht. Das Konvergenzverhalten von Laplace und Lamé-Navier Problemen wird untersucht. Die Simulation von praktischen Problemen veranschaulicht den verminderten Speicherbedarf, die erhöhte Effizienz und die Anwendbarkeit für komplexe Geometrien. Weiters erlaubt die isogeometrische Nyström-Methode das lokale Verfeinern von Tensorprodukt-Flächen. Die vorgestellte Simulationsmethode ermöglicht ein Integrieren der am weitest verbreiteten CAGD Modelle in eine Analyse von linearen Potential- und Elastizitätsproblemen.

Acknowledgements

First of all, I want to express my sincerest gratitude to Prof. Dipl.-Ing. Dr.techn. Gernot Beer for his supervision during the last years. His enduring support has greatly influenced my studies and academic development and has been an excellent mixture of guidance and freedom to opt for new and unplanned directions of research.

Furthermore, I would like to address my sincerest thanks to Prof. Dr.-Ing. Kai-Uwe Bletzinger for providing his time to examine this thesis. His interest in my work is gratefully acknowledged.

I am especially grateful to Prof. Dr.-Ing. habil. Thomas-Peter Fries for his valuable advice and our fruitful discussions.

The present work results from a research project supported by the Austrian science fund FWF, provided under Grant Number P24974-N30:'Fast iso-geometric boundary element method'. This support is gratefully acknowledged.

Many thanks are addressed to my colleagues at the Institute of Structural Analysis for the great time I have had working with them. In particular, I want to thank Christian Dünser and Bernhard Lindner for raising my interest in numerical simulations. I very much appreciate the cooperation with Jürgen Zechner during this research project. His way of thinking has been very inspiring.

Special thanks go to my dear Marlies. I am very grateful for the way how we complement each other.

Finally, I want to thank my family for their support and help at all times.

Graz, September 2015 Benjamin Marussig

Contents

1 Introduction

1.1 Motivation

Numerical methods are an important part of both design and analysis, but their principal objectives are diverse. On the one hand, Computer Aided Geometric Design (CAGD) generally sought to optimize the modeling and visualization of geometric objects. On the other hand, engineering is a problem-solving discipline based on predictions by mathematical models of physical phenomena. Consequently, developments in computational analysis focused on improving the mathematical models and the reliability and efficiency of their numerical treatment. Yet, the accuracy of the results obtained depends also on the quality of the geometrical representation. Hence, expertise of both fields is required to efficiently and accurately simulate practical problems. In fact, CAGD models are often the starting point of the simulation process, but in current engineering design they are subsequently approximated by meshes for the computation. This procedure leads to loss of geometric information. In addition, it impacts the overall analysis time. Figure 1.1 indicates basic stages of an engineering analysis and the related normalized time of each step of the numerical simulation involved [58]. It is noteworthy that only 20% is devoted to the problem solving. In light of this and because of the enormously increasing computational power, geometry manipulations and meshing are indeed the bottleneck of numerical simulation.

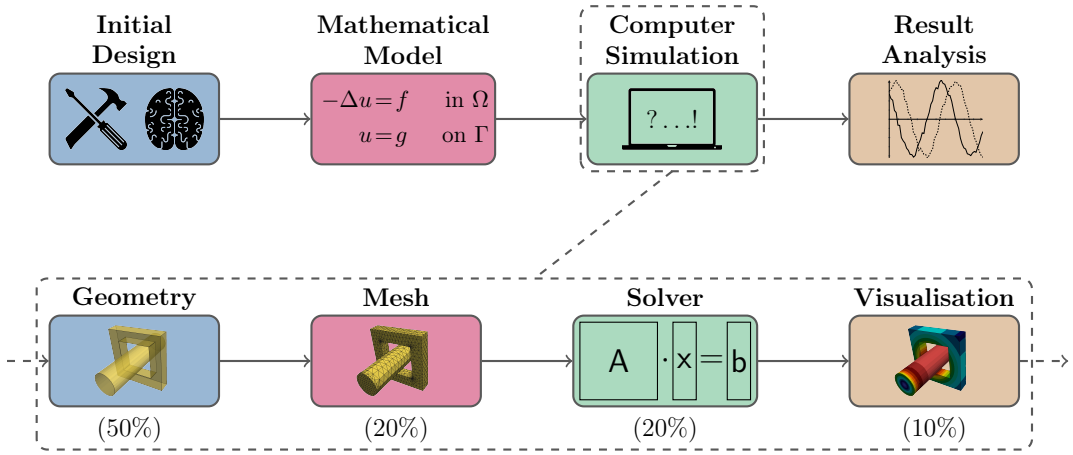

Figure 1.1: Generic model of an engineering analysis process including the normalized time associate with each simulation step according to [58]. Note that a large portion is associated to geometry manipulations and meshing. (Courtesy of TailSiT.)

Isogeometric analysis [37, 66] provides an alternative to the conventional methodology and it has received much attention in recent years. Its primary aim is to enhance numerical simulation by closing the gap between design and analysis. This coalescence shall be accomplished by performing the analysis based on the technologies of CAGD, such

as non-uniform rational B-splines (NURBS) [93, 97], subdivision surfaces [29, 40] and T-splines [111]. As a result, design models can be directly transferred and the process of meshing can be omitted. The desired simulation process is illustrated in Figure 1.2.

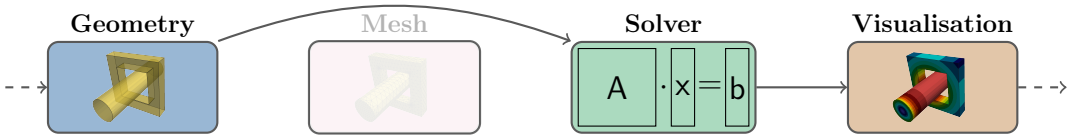

Figure 1.2: Work flow of isogeometric analysis. (Pictures courtesy of TailSiT.)

NURBS are the most popular CAGD approach in engineering design and have become an industry standard for the representation and the data exchange of geometric information [93]. They are included into many exchange standards, like IGES and STEP, which enable the transfer of CAGD models between different software packages. Moreover, it has been demonstrated that NURBS not only fulfill the requirements for the application to analysis, e.g. linear independence, but offer additional computational advantages [35, 36].

However, in order to establish a seamless integration of design and analysis several challenges have to be faced. First of all, engineering design models are usually based on a *boundary representation* (B-Rep), but the most popular numerical simulation method employed in structural mechanics, i.e. the finite element method (FEM), requires a domain discretization. The derivation of volume models from boundary data is far from trivial and still an open research topic [120]. Three dimensional B-Rep models are usually defined by a *non-conforming* partition of NURBS surfaces, i.e. their mathematical parametrization has no explicit relation to each other. Besides, NURBS surfaces are based on tensor product representations. They are very efficient but have limitations due to their four sided nature and therefore the lack of *local refinement* is of particular interest, concerning their application to analysis. Moreover, almost all NURBS based CAGD models use *trimming* procedures to adapt tensor product surfaces. These schemes define certain areas of a surface which are marked as invisible without the need to modify the underlying mathematical parametrization [44]. Since analysis relies on the parametrization of the model rather than its visualization, the treatment of such trimmed geometries is an important aspect. Figure 1.3 summarizes these challenges by illustrating various perspectives of a CAGD model representing a simple solid. The corresponding B-Rep consists of one regular and three trimmed surfaces. In addition, the regular surface has a parametrization which is graded towards one of its corners. It is apparent that even simple CAGD models rely on multiple non-conforming surfaces and that any refinement would extend over the whole surface along its parametric direction.

The motivation for this thesis stems form the desire to develop a simulation method that does not require the generation of a mesh and takes data directly from a CAGD program. In particular, the mentioned challenges of integrating design models into an analysis are addressed and concepts based on *boundary integral equations* (BIEs) are presented to deal with them.

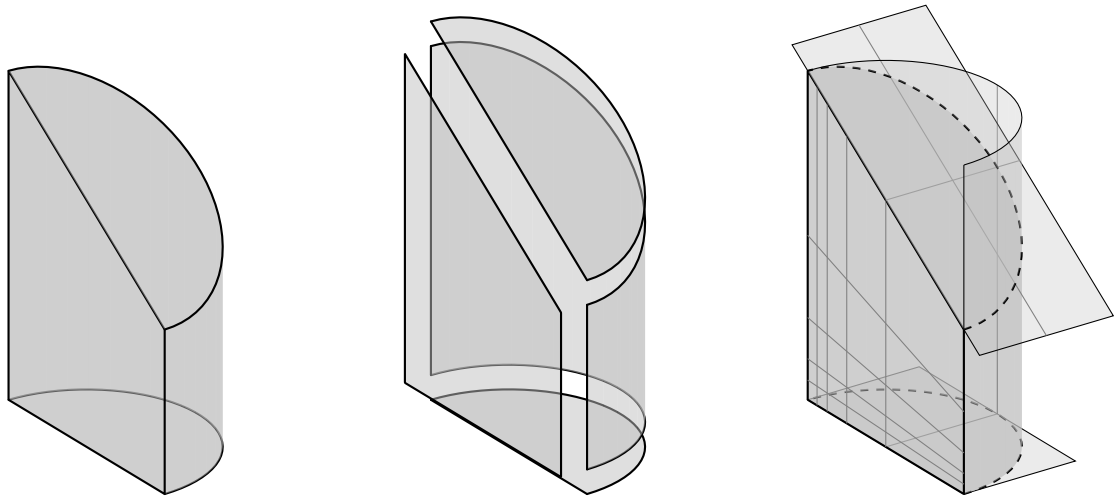

(a) Visualization (b) Components (c) Parametrization

Figure 1.3: Different perspectives of a CAGD solid model: (a) the visible part of the object, (b) segments of its B-Rep and (c) the underlying mathematical parametrization of each surface. In (c), dashed lines mark the boundary of the visible area and gray lines indicate the underlying tensor product basis. Note that the parametrization along common edges does not match. Moreover, the 'local' refinement towards the corner of the non-trimmed component propagates over the whole surface.

1.2 State of the Art

Isogeometric analysis and BIEs are the major fields of research used in this thesis. The following overview provides a brief insight into the current state of research relating to the topics that will be elaborated.

Trimmed Geometry An important issue is the proper integration of trimmed models. Current approaches may be summarized as global and local techniques.

The former [12, 57] substitutes a trimmed surface by one or several regular surfaces. As a consequence the continuity is either locally reduced by the non-smooth edges introduced or the regular surfaces are distorted in many topological cases. Moreover, this approach can not be applied to real-life geometries without user intervention.

The other techniques use the parameter space of the trimmed object as background parametrization. In particular, it is defined by a grid of so-called knot spans and a trimming curve that determines which part is visible. All this information is provided by the CAGD model, but the analysis of knot spans cut by the trimming curve requires special attention. There are different approaches [69, 70, 107, 127] which locally substitute the trimmed area by regular elements providing a mapping from the reference element where quadrature points are specified to the parameter space. In addition, tailored integration formulae may be defined [87, 128]. Due to their local nature, these concepts can be applied to complex CAGD models. However, the resulting basis functions are truncated at the trimming curve.

In the context of collocation methods this is an disadvantage, since the collocation points, i.e. Greville abscissae, of truncated basis functions may be located outside of the actual domain. Moreover, the trimmed basis may lead to system matrices with large condition numbers, if truncated basis functions have a small support. This is a serious drawback since it affects the performance of iterative solvers and more importantly may lead to unstable solutions.

Local Refinement Many developments in isogeometric analysis focus on establishing a local refinement of CAGD models. For instance locally refined B-splines [39] and hierarchical B-splines [126] enhance tensor product parameter spaces such that local refinement can be performed. An alternative approach is to use T-spline models [7, 110] which are not based on a tensor product structure. However, if the original CAGD model is based on NURBS it has to be converted first, i.e. a remodeling procedure is involved.

Non-Conforming Boundary Representation Shell formulations enable the analysis of objects with reduced dimensionality such as plates and membranes by means of finite element methods. Such models do not describe a solid but a manifold, i.e. a surface in three dimensional space. Consequently, B-Rep models define the computational domain rather than its boundary. Several authors have derived various isogeometric shell formulations, e.g. [15, 32, 41, 68]. Moreover, it has been demonstrated that shell structures allow an integration of design and analysis [106] which is also referred to as isogeometric B-Rep analysis [18]. The latter uses a penalty approach to couple common edges of adjacent surfaces. However, these approaches are not concerned with the analysis of solid models.

In the context of finite elements, solid models may be analyzed by means of fictitious domain methods, e.g. [63, 95, 99, 103]. The basic idea is to perform the analysis on a regular background mesh which incorporates the design model. Subsequently, the mesh is split into a part inside and an other outside of the actual domain. Elements at the transition are cut by the B-Rep surfaces and require special attention during the analysis. These cut elements can result in ill-conditioned system matrices, similar to the case of trimmed geometries.

Boundary Integral Equations Numerical approximation methods based on boundary integral equations are a powerful alternative to finite element methods. There are many textbooks regarding their mathematical foundation, e.g. [5, 72, 86, 102, 116]. A historical perspective is provided in [30, 129] and brief overviews of the most important developments are given in [47, 86]. The distinguishing feature of these methods is that they are based on mathematical models, namely BIEs, which represent the governing equations of the problem by means of an integral over the boundary of the computational domain. In other words, they rely on a B-Rep in the same way as design models. Despite the obvious benefit of the conforming geometry representations, no element connectivity is required [89, 90, 105]. Hence, non-conforming surfaces can be handled.

The *boundary element method* (BEM) is the most common and versatile approach to approximate BIEs. The textbooks of Beer et al. [14] and Gaul et al. [47] provide a coherent introduction to the method from an engineering point of view. Recent developments of

BEM besides the isogeometric approach are presented in [77], whereas [13] focuses on the isogeometric BEM advancements.

There have been some early attempts to include CAGD technologies to BEM simulations. In the 1980s and early 1990s, spline approximations have been used to investigate the convergence of collocated BEM formulation in two [3, 4, 34, 100, 101] and three [2, 33, 108] dimensions. Spline based formulations have been applied to elasticity [122], electromagnetic [104, 123] and potential [26, 27, 76, 78, 132] problems. To the best of the authors' knowledge, the first analysis based on NURBS surfaces has been suggested by Valle et al. [124] and Rivas et al. [96] in order to solve Maxwell's equations.

The introduction of isogeometric analysis gave much impetus to a rapid resurgence of this field. During the last years, isogeometric BEM has been applied to various problems governed by the Laplace [45, 53, 56, 94, 118], Stokes [61], Maxwell [85, 125], Lamé-Navier [75, 82, 109, 112] and Helmholtz [91, 113] equations.

Nyström introduced an alternative numerical approximation method to solve BIEs [88]. In particular, he proposed that the boundary integrals are directly evaluated by means of numerical quadratures and the unknown function values at the quadrature points are treated as degrees of freedom. If the boundary integrals and the domain are smooth, the Nyström method is in fact based on point-wise evaluations.

However, the integrands encountered in BIEs contain fundamental solutions which are singular functions and require special treatment. In the context of the Nyström method, several techniques have been developed such as product integration [5] and singularity subtraction [1]. Sloan [114] provides error analysis for such methods and the convergence behavior of several approaches is investigated in [55]. In the present implementation, the *locally corrected* Nyström method [28, 117] is used, i.e. the singular function is regularized by the local construction of a tailored quadrature rule. The interested reader is referred to [49, 92] for a good introduction to this procedure and mathematical proofs can be found in [52, 74].

An advantage of the Nyström method is that higher order convergence rates can be simply achieved by increasing the order of the chosen quadrature. However, a smooth boundary representation is required to obtain optimal convergence behavior [5]. In other words, standard triangulations are insufficient for curved geometries because kinks arise between elements of the mesh. The required continuity may be restored by re-parametrization procedures [67, 130] as suggested in [131]. Nevertheless, due to this problem the Nyström method has been mostly applied to analytical surfaces. If computational domains are smooth but contain some defined corners or edges, higher order convergence can be restored by a grading of the integration regions [5]. Several authors proposed alternative approaches for two dimensional problems [20, 22, 25, 50, 60, 71]. While it is claimed that they can be extended to the three dimensional case, only few results are reported [21]. Such procedures are also required in case of non-smooth or mixed boundary conditions [31, 59].

Applications of the Nyström method are for example potential [5] and electro-magnetic problems [46, 48], Stokes flow [51], elastic wave scattering [121], the analysis of edge cracks [43], problems governed by the Helmholtz equation [23, 24, 28] and it is generally applicable to parabolic BIEs [119].

1.3 Isogeometric Analysis based on Boundary Integral Equations

In this dissertation, an isogeometric framework for a seamless integration of design and analysis is developed which is based on boundary integral equations. In particular, the analysis of linear problems governed by the Laplace and Lamé-Navier equations are considered and solved using a NURBS based boundary representation. The main contributions of this thesis are:

- Development of an *independent field approximation* paradigm which permits a separate approximation of integral operators.
- Application and implementation of *extended B-splines* for dealing with trimmed surfaces in an isogeometric BEM analysis.
- Formulation of a locally corrected *isogeometric Nyström method* and its application to the Laplace and Lamé-Navier equations.

The first point enables an efficient and flexible formulation which allows maintaining the original CAGD model during the analysis. With this concept and the Nyström method, the application of local refinement is straightforward. Extended B-splines have been introduced in the context of fictitious domain methods [62–64, 99] in order to deal with the negative impact of cut basis functions. To the best of the authors' knowledge, there is only a single publication [65] related to trimmed geometries, although this application has been suggested in the landmark paper of isogeometric analysis [66]. Moreover, the benefit of extended B-splines regarding collocation approaches has not been investigated yet. Finally, the first application of the isogeometric paradigm to the Nyström method is demonstrated in this thesis.

The present work results from a research project supported by the Austrian science fund FWF, provided under Grant Number P24974-N30. This support provided the basis for the information published in [8–13, 80–82, 133, 134]. Some results of this dissertation have been disseminated in these works, in addition the most recent findings, e.g. the application of extended B-splines, are presented.

The aim of this thesis is to develop a methodology which allows a seamless integration of the most common CAGD models in engineering design, i.e. geometries represented by trimmed NURBS, into an analysis of linear potential and elasticity problems through the utilization of BIEs.

1.4 Organization of the Thesis

The dissertation begins by introducing the basic features of NURBS basis functions and the corresponding geometrical models in Chapter 2. Emphasis is given to those aspects which are important for the subsequent application to an analysis. Chapter 3 provides a brief overview of boundary integral equations and introduces the required operators.

In Chapter 4, the previous parts are brought together by means of a conventional isogeometric framework. In particular, the isogeometric Nyström method and collocated isogeometric BEM are presented. Throughout this chapter, the isoparametric concept is

utilized, i.e. the same basis functions are applied to all fields. In Chapter 5, this paradigm is changed in order to obtain a more flexible and efficient formulation for both the Nyström and BEM approach. Chapter 6 proceeds to discuss the treatment of trimmed objects using extended B-splines and the application to analysis. It provides a general procedure to construct the related extrapolation weights and examines the quality of the approximation obtained.

Chapter 7 is dedicated to numerical investigations of the proposed methodology. Firstly, the convergence behavior of the presented isogeometric BEM and Nyström formulations is critically studied. Secondly, miscellaneous examples emphasize features and benefits of combining isogeometric analysis, boundary integral equations and independent field approximation. Finally, trimmed CAGD models are analyzed.

In the concluding Chapter 8, the key findings are summarized and research topics identified that need further investigation.

2 B-splines and NURBS

B-splines and their rational counterpart NURBS provide the basis for most engineering design models. This chapter gives a brief overview of this CAGD technology focusing on aspects which are crucial for their subsequent application to analysis. For further information related to spline theory the interested reader is referred to [16, 44]. Detailed descriptions of efficient algorithms can be found in [93]. In the present thesis, the terms B-spline and NURBS are used to refer to basis functions. Moreover, the geometric objects described using these functions, i.e. curves and surfaces, may be denoted generally as *patches*.

2.1 Basis Functions

B-splines $B_{i,p}$ consist of polynomial segments which are connected by a certain smoothness. They are defined recursively for a fixed polynomial degree p by a strictly convex combination of B-splines of the previous degree, $p-1$, given by

$$B_{i,p}(r) = \frac{r - r_i}{r_{i+p} - r_i} B_{i,p-1}(r) + \frac{r_{i+p+1} - r}{r_{i+p+1} - r_{i+1}} B_{i+1,p-1}(r) \tag{2.1}$$

with

$$B_{i,0}(r) = \begin{cases} 1 & \text{if } r_i \leqslant r < r_{i+1} \\ 0 & \text{otherwise.} \end{cases} \tag{2.2}$$

The essential element for this construction is the *knot vector* Ξ characterized as a non-decreasing sequence of coordinates $r_i \leqslant r_{i+1}$. The parameters r_i are termed *knots* and the half-open interval $[r_i, r_{i+1})$ is called ith *knot span*. Each knot span has $p+1$ non-vanishing B-splines as illustrated in Figure 2.1. Each basis function is entirely defined by $p+2$ knots

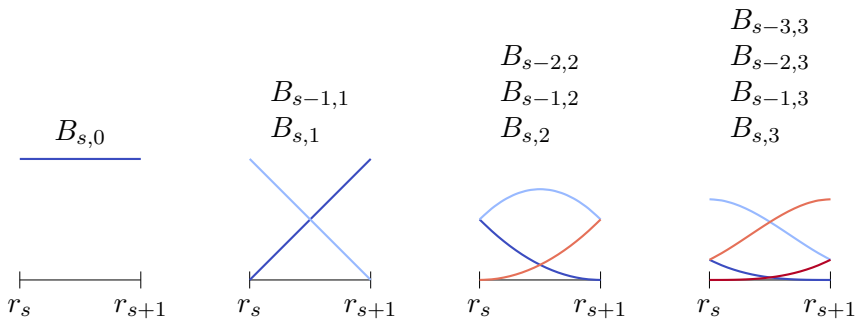

Figure 2.1: Non-vanishing B-splines $B_{i,p}$ of knot span s for different degrees $p = \{0, 1, 2, 3\}$ which are based on a knot vector with equally spaced knots.

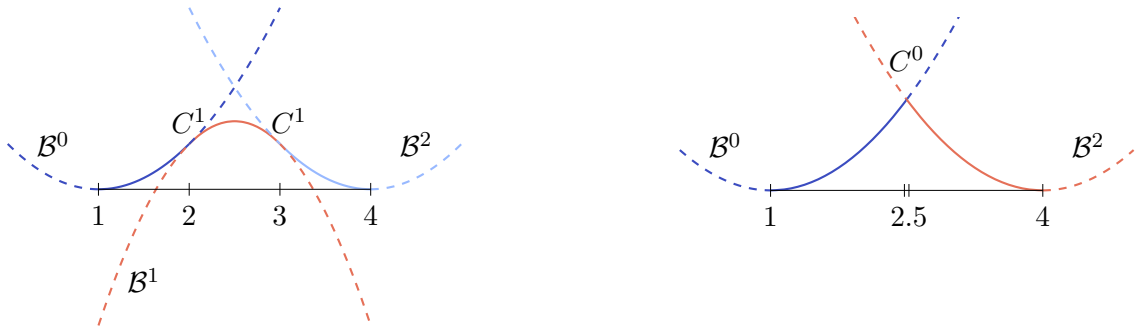

(a) $\Xi = \{1, 2, 3, 4\}$ (b) $\Xi = \{1, 2.5, 2.5, 4\}$

Figure 2.2: Polynomial segments $\mathcal{B}^s$ of a quadratic B-spline due to different knot vectors Ξ. The resulting polynomial segments are indicated by dashed lines, whereas solid lines represent the corresponding basis function.

and its support, $\operatorname{supp}\{B_{i,p}\} = \{r_i, \ldots, r_{i+p+1}\}$, is local. Within each non-zero knot span s, $r_s < r_{s+1}$, of its support, $B_{i,p}$ is described by a polynomial segment $\mathcal{B}_i^s$. Each knot value indicates a location within the parameter space which is not C^∞-continuous, i.e. where two adjacent $\mathcal{B}_i^s$ join. Successive knots may share the same value, which is indicated by the knot multiplicity m, i.e. $r_i = r_{i+1} = \cdots = r_{i+m-1}$. In general, the continuity between adjacent segments is C^{p-m}. This control of continuity is demonstrated for a quadratic B-spline in Figure 2.2. If the multiplicity of the first and last knot is equal to $p+1$, the knot vector is denoted as *open* knot vector. The knot sequence

$$\Xi = \{r_0 = \cdots = r_p, r_{p+1} = \cdots = r_{2p+1}\} \tag{2.3}$$

is a special from of such a knot vector since it yields the classical pth-degree Bernstein polynomials.

As a whole, B-splines based on a common knot vector Ξ form a *partition of unity*, i.e.

$$\sum_{i=0}^{I-1} B_{i,p}(r) = 1, \qquad r \in [r_0, r_{I+p}] \tag{2.4}$$

and they are *linear independent*, i.e.

$$\sum_{i=0}^{I-1} B_{i,p}(r)\, c_i = 0 \tag{2.5}$$

is satisfied if and only if $c_i = 0,\ i = 0, \ldots, I-1$. Due to the latter property, every piecewise polynomial $f_{p,\Xi}$ of degree p over a knot sequence Ξ can be uniquely described by a linear combination of the corresponding $B_{i,p}$. Hence, they form a *basis* of the space $\mathbb{S}_{p,\Xi}$ collecting all such functions

$$\mathbb{S}_{p,\Xi} = \sum_{i=0}^{I-1} B_{i,p}\, c_i, \qquad c_i \in \mathbb{R}. \tag{2.6}$$

The first derivative of B-splines are computed by a linear combination of B-splines of the previous degree

$$B'_{i,p}(r) = \frac{p}{r_{i+p} - r_i} B_{i,p-1}(r) - \frac{p}{r_{i+p+1} - r_{i+1}} B_{i+1,p-1}(r). \tag{2.7}$$

This can be generalized to compute the kth derivative of a B-spline

$$B^{(k)}_{i,p}(r) = \frac{p!}{(p-k)!} \sum_{l=0}^{k} a_{k,l} B_{i+l,p-k}(r) \tag{2.8}$$

with

$$\begin{aligned} a_{0,0} &= 1 \\ a_{k,0} &= \frac{a_{k-1,0}}{r_{i+p-k+1} - r_i} \\ a_{k,l} &= \frac{a_{k-1,l} - a_{k-1,l-1}}{r_{i+p+l-k+1} - r_{i+l}} \qquad l = 1, \ldots, k-1 \\ a_{k,k} &= \frac{-a_{k-1,k-1}}{r_{i+p+1} - r_{i+k}}. \end{aligned}$$

Remark: The knot differences of the denominators involved in the recursive formulae (2.1), (2.7) and (2.8) can become zero. In such a case the quotient is defined to be zero.

2.2 Curves

B-spline curves of degree p are defined by basis functions $B_{i,p}$ due to a knot vector Ξ with corresponding coefficients in physical space $\boldsymbol{c}_i$ which are denoted as *control points*. The geometrical mapping $\mathcal{X}$ from parameter space to physical space is given by

$$\mathcal{X}(r) \coloneqq \boldsymbol{x}(r) = \sum_{i=0}^{I-1} B_{i,p}(r)\, \boldsymbol{c}_i \tag{2.9}$$

with I representing the total number of basis functions. The related Jacobi-matrix is

$$\mathbf{J}_{\mathcal{X}}(r) \coloneqq \sum_{i=0}^{I-1} B'_{i,p}(r)\, \boldsymbol{c}_i \,. \tag{2.10}$$

In general, control points $\boldsymbol{c}_i$ are not interpolatory, i.e. they do not lie on the curve. The connection of $\boldsymbol{c}_i$ by straight lines is called *control polygon* and it provides an approximation of the actual curve. An important property of a B-spline curve is that it is contained within the *convex hull* of its control polygon. In particular, a polynomial segment related to a non-zero knot span s, i.e. $r \in [r_s, r_{s+1})$, is in the convex hull of the control points $\boldsymbol{c}_{s-p}, \ldots, \boldsymbol{c}_s$. The continuity of the whole piecewise polynomial curve $\boldsymbol{x}(r)$ is inherited from its underlying basis functions, i.e. the continuity at knots is determined by the knot multiplicity. These relationships are illustrated in Figure 2.3. Note that the interpolatory

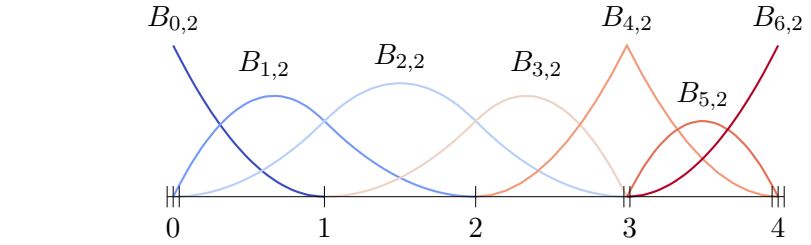

(a) Basis Functions

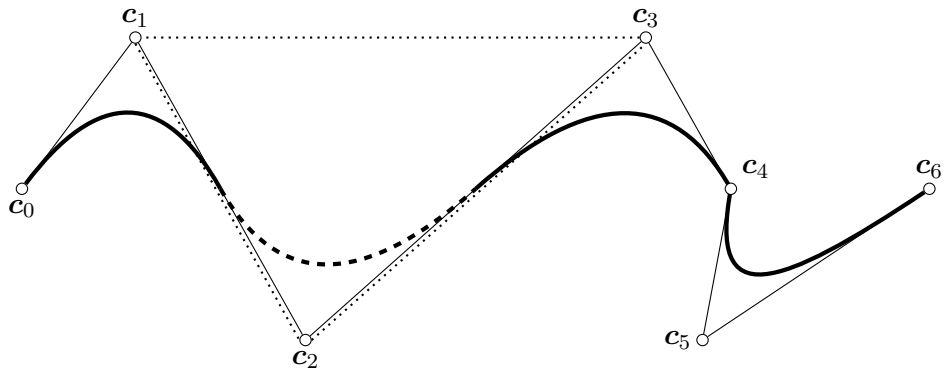

(b) Quadratic B-spline Curve

Figure 2.3: (a) B-splines based on $\Xi = \{0, 0, 0, 1, 2, 3, 3, 4, 4, 4\}$ and (b) a corresponding piecewise polynomial curve. In (b), circles denote control points and the dotted lines indicate the convex hull of the dashed curve segment $r \in [1, 2)$.

B-spline $B_{4,2}$ of Figure 2.3(a) corresponds to the kink at $\boldsymbol{c}_4$ in Figure 2.3(b) and that the second polynomial segment lies within the convex hull of $\boldsymbol{c}_1$ to $\boldsymbol{c}_3$. If the curve consist of a single polynomial segment, i.e. the related Ξ is of form (2.3), the curve is referred to as *Bézier* curve. In addition, a polynomial segment of a B-spline curve is termed Bézier segment, if it could be represented by a Bézier curve. In Figure 2.3(b), this is the case for the segment $r \in [3, 4]$ defined by the control points $\boldsymbol{c}_4$ to $\boldsymbol{c}_6$.

B-spline curves can be generalized to represent rational functions such as conic sections. For this purpose, *weights* w_i are associated with the control points such that

$$\boldsymbol{c}_i^h = (w_i \boldsymbol{c}_i, w_i)^\intercal = (\boldsymbol{c}_i^w, w_i)^\intercal \in \mathbb{R}^{d+1} \tag{2.11}$$

where d denotes the spacial dimension of the physical space. The *homogeneous coordinates* $\boldsymbol{c}_i^h$ define a B-spline curve $\boldsymbol{x}^h(r)$ in a projective space $\mathbb{R}^{d+1}$. In order to obtain a curve in $\mathbb{R}^d$ the geometrical mapping (2.9) is extended by a perspective mapping $\mathcal{P}$ with the center at the origin of $\mathbb{R}^{d+1}$. This projection is given by

$$\boldsymbol{x}(r) = \mathcal{P}(\boldsymbol{x}^h(r)) = \frac{\boldsymbol{x}^w(r)}{w(r)} \qquad \text{with} \qquad w(r) = \sum_{i=0}^{I-1} B_{i,p}(r)\, w_i \tag{2.12}$$

where $\boldsymbol{x}^w = \left(\boldsymbol{x}_1^h, \ldots, \boldsymbol{x}_d^h\right)^\intercal$ are the homogeneous vector components of the curve. The

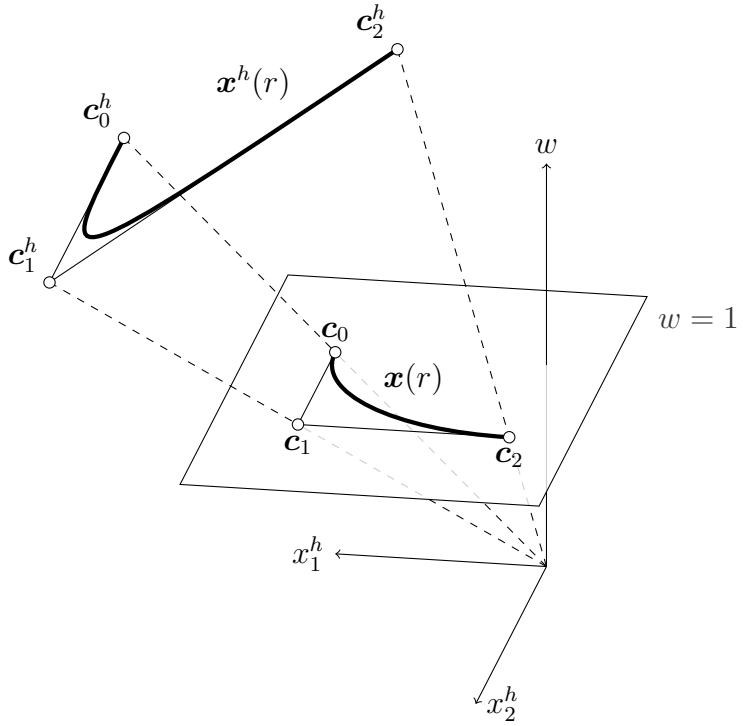

Figure 2.4: Perspective mapping $\mathcal{P}$ of a quadratic B-spline curve $\boldsymbol{x}^h(r)$ in homogeneous form $\mathbb{R}^3$ to a circular arc $\boldsymbol{x}(r)$ in physical space $\mathbb{R}^2$. The mapping is indicated by dashed lines.

application of equation (2.12) is illustrated in Figure 2.4: a circular arc $\boldsymbol{x}(r)$ in the physical space $\mathbb{R}^2$ is constructed by the projection of a quadratic B-spline curve $\boldsymbol{x}^h(r)$ defined by the control points $\boldsymbol{c}_0^h = (2,0,2)^\intercal$, $\boldsymbol{c}_1^h = (2,3,2)^\intercal$ and $\boldsymbol{c}_2^h = (0,4,4)^\intercal$. In general, the projection $\boldsymbol{x}(r)$ is denoted as *non-uniform rational B-spline* (NURBS) curve. The term rational indicates that the represented curves are piecewise rational polynomials, whereas the term non-uniform emphasizes that the knot values can be distributed arbitrarily.

The Jacobi-matrix of the NURBS geometrical mapping is defined by

$$\mathbf{J}_{\mathcal{X}}(r) \coloneqq \frac{w(r)\frac{\partial \boldsymbol{x}^w(r)}{\partial r} - \frac{\partial w(r)}{\partial r}\boldsymbol{x}^w(r)}{\left(w(r)\right)^2} \tag{2.13}$$

with

$$\frac{\partial w(r)}{\partial r} = \sum_{i=0}^{I-1} B'_{i,p}(r) w_i \qquad \text{and} \qquad \frac{\partial \boldsymbol{x}^w(r)}{\partial r} = \sum_{i=0}^{I-1} B'_{i,p}(r) \boldsymbol{c}_i^w. \tag{2.14}$$

Another way to represent NURBS curves is given by

$$\boldsymbol{x}(r) = \sum_{i=0}^{I-1} R_{i,p}(r)\, \boldsymbol{c}_i \qquad \text{with} \qquad R_{i,p}(r) = \frac{w_i B_{i,p}(r)}{w(r)}\,. \tag{2.15}$$

The weighting function $w(r)$ is the same as in equation (2.12) and $R_{i,p}$ is denoted as NURBS basis function. Since the weights w_i are now associated with B-splines $B_{i,p}$ the mapping (2.15) employs control points $\boldsymbol{c}_i$ of the physical space.

However, NURBS curves degenerate to B-spline curves, if all weights are equal. Hence, they are a generalization of them. The properties of B-spline curves apply for their rational counterpart as well, if the weights are non-negative which is usually the case.

2.3 Tensor Product Surfaces

Tensor products surfaces are an extremely efficient technique compared to other geometry descriptions. Hence, they play an important role in CAGD. In particular, B-spline and NURBS patches are very common. Basis functions for B-spline patches are obtained by the tensor product of univariate B-splines which are defined by separate knot vectors Ξ_I and Ξ_J. These knot vectors determine the parametrization in the directions r_1 and r_2, respectively. Moreover, they span the bivariate basis of a patch and specify its local coordinates $\mathbf{r} = (r_1, r_2)^\intercal$. Combined with a bidirectional grid of control points $\boldsymbol{c}_{i,j}$ the geometrical mapping is given by

$$\mathcal{X}(\mathbf{r}) \coloneqq \boldsymbol{x}(r_1, r_2) = \sum_{i=0}^{I-1} \sum_{j=0}^{J-1} B_{i,p_1}(r_1) B_{j,p_2}(r_2)\, \boldsymbol{c}_{i,j}\,. \tag{2.16}$$

The polynomial degrees for each parametric direction are denoted by p_1 and p_2. The Jacobian of the mapping (2.16) is computed by substituting the occurring univariate B-splines by their first derivatives, alternately for each direction. In general, derivatives of B-spline patches are specified by

$$\frac{\partial^{k+l}}{\partial^k r_1 \partial^l r_2} \boldsymbol{x}(r_1, r_2) = \sum_{i=0}^{I-1} \sum_{j=0}^{J-1} B^{(k)}_{i,p_1}(r_1) B^{(l)}_{j,p_2}(r_2)\, \boldsymbol{c}_{i,j}\,. \tag{2.17}$$

The tensor product nature of the patches is illustrated in Figure 2.5 by means of a bivariate basis. Note that the univariate knot values propagate over the whole parameter space. A corresponding patch is depicted in Figure 2.6. If both knot vectors are of form (2.3) the surface is referred to as Bézier surface. Moreover, NURBS surfaces are derived analogous to curves by the introduction of weights.

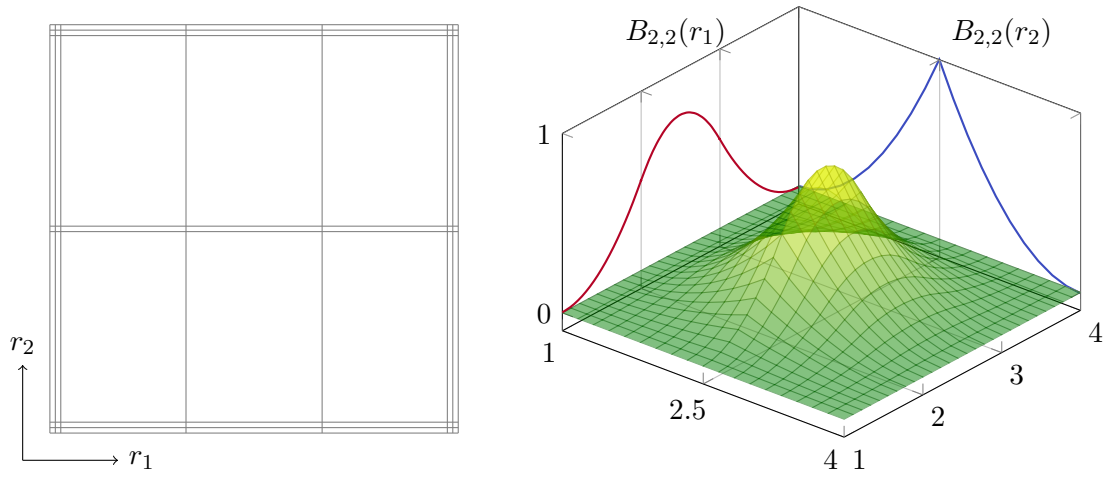

(a) Parameter Space (b) Basis Function

Figure 2.5: Bivariate basis defined by the knot vectors $\Xi_I = \{1, 1, 1, 2, 3, 4, 4, 4\}$ related to r_1 and $\Xi_J = \{1, 1, 1, 2.5, 2.5, 4, 4, 4\}$ for r_2: (a) shows the bivariate basis spanned by Ξ_I and Ξ_J, whereas (b) illustrates the construction of a corresponding bivariate B-spline.

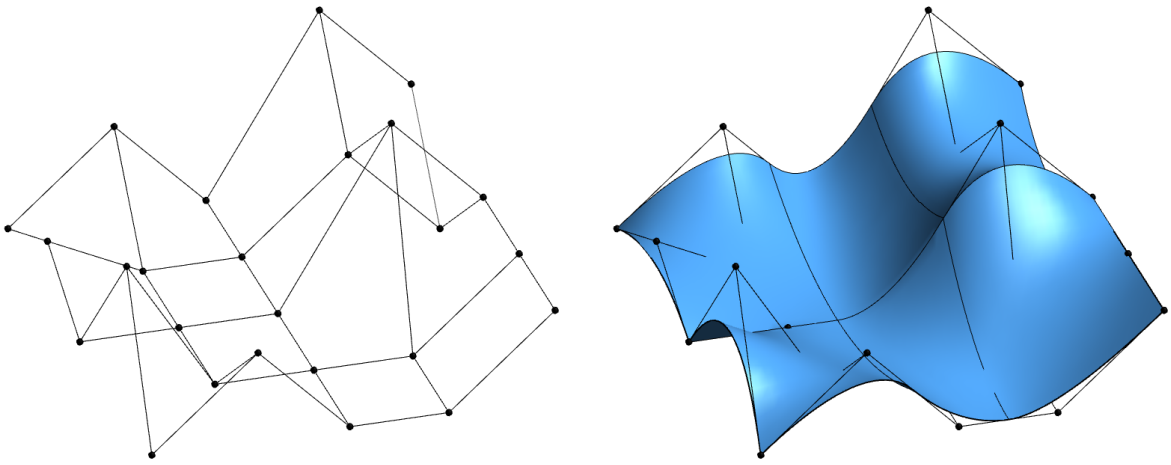

(a) Control Grid (b) B-spline Patch

Figure 2.6: Control points (a) and resulting tensor product surface (b). The basis is given by $\Xi_I = \{1, 1, 1, 2, 3, 4, 4, 4\}$ and $\Xi_J = \{1, 1, 1, 2.5, 2.5, 4, 4, 4\}$.

2.4 Refinement Procedures

A given NURBS curve $\boldsymbol{x}(r)$ can be refined such that the resulting object $\hat{\boldsymbol{x}}(r)$ is equivalent to the original one, i.e. $\boldsymbol{x}(r) \equiv \hat{\boldsymbol{x}}(r)$. The related procedures are called *knot insertion* and *degree elevation*. In both cases, a given knot vector Ξ is expanded to an extended knot vector $\hat{\Xi}$ by adding new knots $\hat{r}$ to it. Hence, the number of basis functions is increased. Moreover, the position of these $\hat{r}$ determine the control points $\hat{\boldsymbol{c}}_i^h$ of the refined NURBS curve. In other words, the refinement procedures define a new basis and set of coordinates including the weights w_i such that the geometry representation does not change.

In case of knot insertion, the degree p of the curve is not changed but each new knot $\hat{r} \in [r_s, r_{s+1})$ introduces a new control point. In addition, neighboring control points are adjusted as well. Their coordinates are obtained by

$$\hat{\boldsymbol{c}}_i^h = \alpha_i \boldsymbol{c}_i^h + (1-\alpha_i)\, \boldsymbol{c}_{i-1}^h \qquad \text{with} \qquad \alpha_i = \begin{cases} 1 & i \leqslant s-p \\ \frac{\hat{r}-r_i}{r_{i+p}-r_i} & s-p+1 \leqslant i \leqslant s-m \\ 0 & i \geqslant s-m+1 \end{cases} \tag{2.18}$$

where m denotes the initial multiplicity of $\hat{r}$. On the other hand, degree elevation increases the degree of NURBS by replicating existing knots. According to Piegl and Tiller [93] the construction of the corresponding control points involves the following steps:

1. Subdividing of the curve into Bézier segments by knot insertion.

2. Degree elevation of these Bézier segments given by

$$\hat{\boldsymbol{c}}_i^h = (1-\alpha_i)\, \boldsymbol{c}_i^h + \alpha_i \boldsymbol{c}_{i-1}^h \qquad \text{with} \qquad \alpha_i = \frac{i}{p+1}, \qquad i = 0, \ldots, p+1. \tag{2.19}$$

3. Removing of superfluous knots which separates the elevated segments by the reverse process of knot insertion in order to obtain a NURBS curve again.

Remark: Degree elevation is also denoted as order elevation. In fact, the latter is more commonly used in isogeometric analysis. However, in CAGD the term *order* $\tilde{p}$ has a distinct meaning and is specified as $\tilde{p} = p + 1$. In this thesis, the definition as degree elevation is used for the sake of clarity.

Figure 2.7 shows the curve of Figure 2.3 which has been refined by the insertion of two knots $\hat{r}_i = \{1, 2.5\}$, whereas Figure 2.8 depicts a degree elevated version. Note that the curve does not change, but its approximation by the control polygon as well as the convex hull of polynomial segments are improved, i.e. they are getting closer to the curve, in both cases. Regarding surfaces, the refinement can be applied separately for each parametric direction. However, it is not possible to perform local refinement due to the tensor product nature of the basis functions.

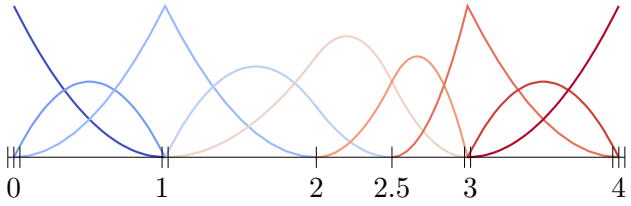

(a) Refined Basis Functions

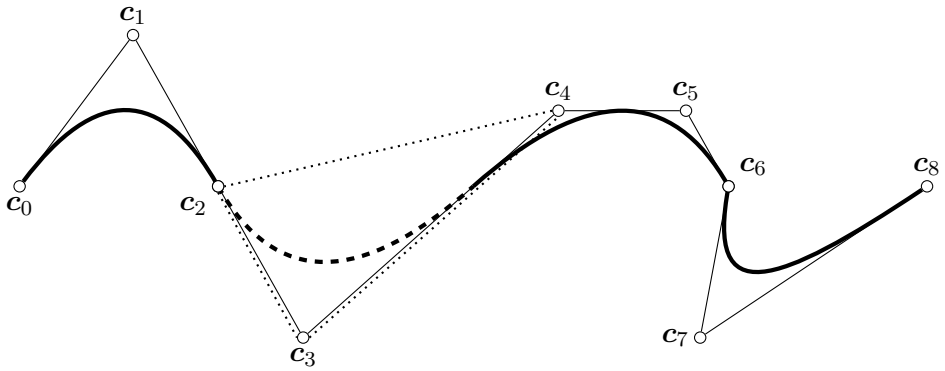

(b) Quadratic B-spline Curve

Figure 2.7: Knot insertion applied to the curve of Figure 2.3 with $\hat{r}_i = \{1, 2.5\}$.

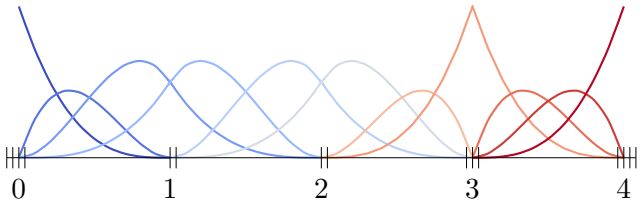

(a) Degree Elevated Basis Functions

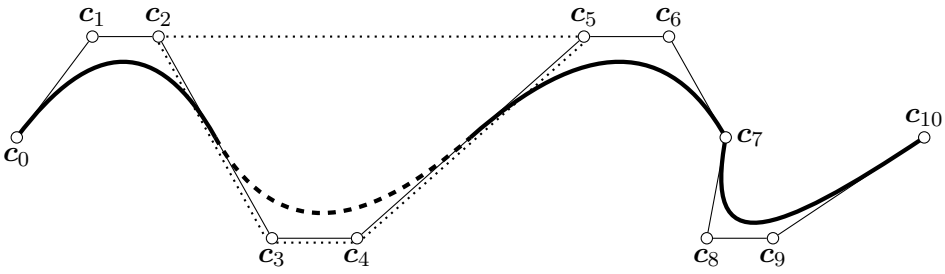

(b) Cubic B-spline Curve

Figure 2.8: Degree elevation applied to the B-spline curve of Figure 2.3.

2.5 Spline Interpolation

In case of a spline interpolation problem, a given function f shall be approximated by a B-spline curve $I_h f \coloneqq \sum_{i=0}^{I-1} B_{i,p}\, c_i$. They agree at I data sites $\bar{r}$ if and only if

$$f(\bar{r}_j) = \sum_{i=0}^{I-1} B_{i,p}(\bar{r}_j)\, c_i, \qquad j = 0, \ldots, I-1. \tag{2.20}$$

The corresponding system of equations consists of the unknown coefficients c_i and the *spline collocation matrix* $\mathbf{A}_r$ which is defined by

$$\mathbf{A}_r[j,i] = B_{i,p}(\bar{r}_j), \qquad i,j = 0, \ldots, I-1. \tag{2.21}$$

The *Schoenberg-Whitney theorem* [16, 44] states that the matrix $\mathbf{A}_r$ is invertible if and only if

$$B_{i,p}(\bar{r}_i) \neq 0, \qquad i = 0, \ldots, I-1. \tag{2.22}$$

In general, the interpolation error for every continuous function f over a fixed interval $[a,b]$ is bounded by

$$\|f - I_h f\| \leq \mathrm{const}_p\, (1 + \|I_h\|)\, \|f^{(p+1)}\|_\infty\, |r|^{p+1} \tag{2.23}$$

with

$$|r| \coloneqq \max_i \Delta r_i = \max_i (r_{i+1} - r_i)$$
$$\|I_h\| \coloneqq \max\{\|I_h f\|/\|f\| : f \in C[a,b]\backslash\{0\}\}.$$

Proofs and more detailed information can be found in [16]. The bound (2.23) indicates that the knot placement influences the approximation quality. However, in order to find optimal knots, information about the target function f must be given, which is generally not the case in analysis. Hence, it is focused on the norm $\|I_h\|$ of the interpolation process I_h.

Since condition (2.22) guarantees that $\mathbf{A}_r$ does not become singular, it is expected that $\|I_h\|$ gets large if $\bar{r}$ approaches the limits of its allowed range. Non-uniformity of $\bar{r}$ is another reason for an increasing $\|I_h\|$. In fact, $\|I_h\|$ gets arbitrary large if two interpolation sites approach each other, while the others are fixed. Several authors [6, 16, 75] recommend to interpolate at the *Greville abscissae* $\bar{r}^g$ which is obtained by the following knot average

$$\bar{r}_i^g = \frac{r_{i+1} + r_{i+2} + \cdots + r_{i+p}}{p}. \tag{2.24}$$

This abscissae are well known in CAGD and used for different purposes, e.g. to generate a linear geometrical mapping [44]. The most important feature of this approach is that it induces a stable interpolation scheme for moderate degrees p. It should, however, be noted that it may get unstable for higher degrees, in particular for non-uniform knot vector.

The only interpolation scheme that provides a stable interpolation for any degree is proposed by Demko [38]. It is independent of Ξ and minimizes the max-norm of the

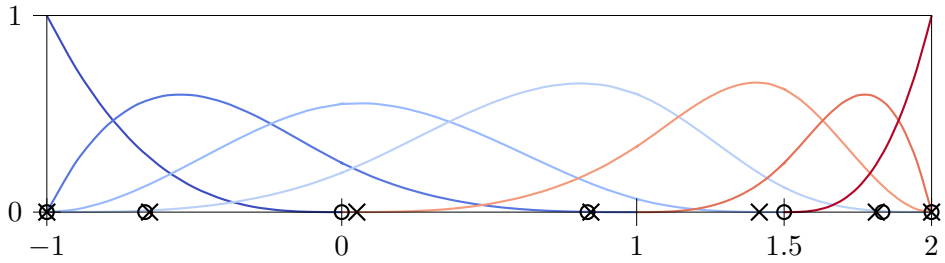

Figure 2.9: Basis function defined by $\Xi = \{-1, -1, -1, -1, 0, 1, 1.5, 2, 2, 2, 2\}$. The corresponding Greville abscissae are marked by circles, whereas crosses are used to indicate the Demko abscissae.

inverse spline collocation matrix $\|\mathbf{A}_r^{-1}\|$, where it can be shown that

$$\|I_h\| \leq \|\mathbf{A}_r^{-1}\|. \tag{2.25}$$

The minimization is achieved using the *Demko abscissae* $\bar{r}^d$, which are extrema of Chebyshev splines for a given knot vector Ξ. The computation of $\bar{r}^d$ is more involved than using the knot average (2.24). In fact, the Greville abscissae are usually used as initial guess for an iterative process and the resulting sequence of $\bar{r}^d$ is often similar to $\bar{r}^g$, as illustrated in Figure 2.9. A more detailed comparison of these approaches is provided in Appendix A.

For the remainder of this dissertation the abscissae $\bar{r}$ are generally denoted as *anchors*. In particular, they are used as a means of linking basis functions $B_{i,p}$ to a point at a specific position $\bar{r}_i$ in the parameter space.

2.6 Complex CAGD Models

Most CAGD objects are based on a boundary representation. In general, these design models consists of several boundary patches γ

$$\Gamma = \bigcup_{i=1}^{I} \gamma_i. \tag{2.26}$$

where Γ denotes the objects' boundary. If Γ is a curve, several patches may be needed to represent distinct sections with different polynomial degrees. This is not a critical issue since curves can be joined rather easily, even with a certain continuity. However, a topological penalty arises as soon as it comes to surfaces, because tensor product surfaces are four sided by definition. A single regular NURBS patch may be closed equivalently to a cylinder or a torus. Spherical topologies may be represented as well, if degenerated edges, i.e. an edge collapses to a point, are introduced. Yet, more complicated objects such as a double torus require partitions into *multiple* NURBS patches. Moreover, the connection of two adjacent surfaces is complicated, especially if a certain continuity is desired. In general, *non-conforming* parametrizations along surface boundaries may be expected.

In order to increase the flexibility of tensor product surfaces they can be modified by

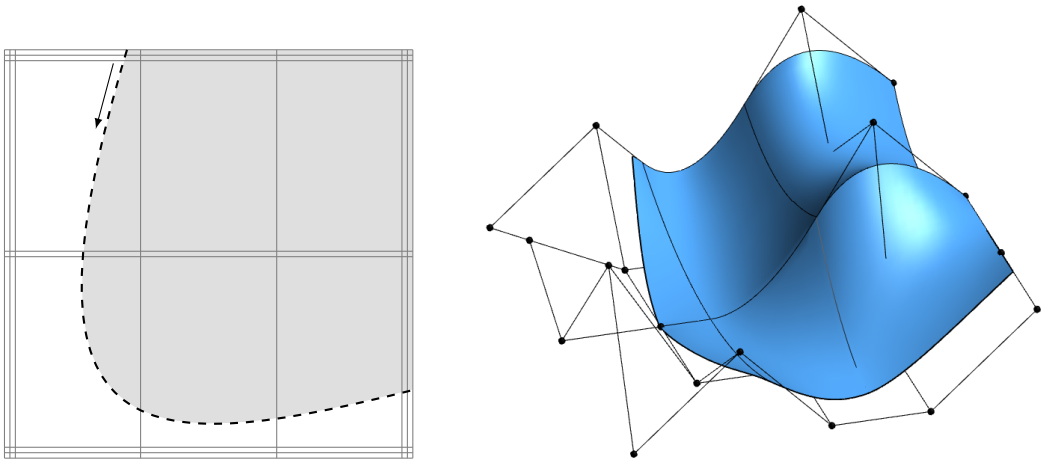

(a) Trimmed Parameter Space (b) Trimmed Patch

Figure 2.10: Trimmed version of the surface shown in Figure 2.6: (a) trimmed parameter space where the trimming curve is indicated by the dashed line and the visible part is highligthed in gray and (b) the resulting trimmed surfaces.

trimming procedures. For this purpose, a curve is defined within the parametric space of a patch. This *trimming curve* is usually a B-spline or NURBS curve and divides the resulting *trimmed patch* into separate parts where the curve's direction determines which one is visible. As a result non-rectangular topologies can be represented. An example of a trimmed patch is shown in Figure 2.10. It should be noted that the mathematical description, i.e. the tensor product basis and the related control grid, of the original patch does not change.

3 Boundary Integral Equations

Systems of partial differential equations (PDEs) can describe many physical processes. This dissertation is dedicated to the solution of linear potential and elasticity problems for homogeneous domains which are numerically solved by methods based on *boundary integral equations*. These equations are obtained by transforming PDEs into integral equations so that the unknown occurs on the boundary of the computational domain only. This process requires a *fundamental solution* of the underlying differential operator. There are many well-written books on boundary integral equations. For their in-depth discussion the reader is particularly referred to [5, 72, 102, 116]. The aim of this chapter is to provide a brief overview and to introduce the notation subsequently used.

3.1 Partial Differential Equations

The physical problems considered in this dissertation are governed by the Laplace and Lamé-Navier equations. In the following, their corresponding elliptic partial differential operators $\mathcal{L}$ are introduced.

The partial derivative of a physical quantity u is denoted as

$$\partial_i u = u_{,i} = \frac{\partial u}{\partial x_i}, \qquad 1 \leqslant i \leqslant d \tag{3.1}$$

where d is the spatial dimension and the spatial point related to the quantity u is denoted by $\boldsymbol{x} = (x_1, \ldots, x_d)^\intercal$. By introducing the *gradient* of a differentiable scalar function u

$$\operatorname{grad} u \coloneqq \nabla u \coloneqq (\partial_1 u, \ldots, \partial_d u)^\intercal \tag{3.2}$$

and the *divergence* of a differentiable vector field $\mathbf{w}$

$$\operatorname{div} \mathbf{w} \coloneqq \nabla \cdot \mathbf{w} \coloneqq \sum_{i=1}^{d} \partial_i u_i \tag{3.3}$$

the *Laplace* operator can be defined by

$$\Delta u = \operatorname{div} \operatorname{grad} u = \nabla \cdot \nabla u = \sum_{i=1}^{d} \partial_i^2 u. \tag{3.4}$$

Moreover, the *curl* operate is specified as

$$\operatorname{curl} \mathbf{w} \coloneqq \nabla \times \mathbf{w} \coloneqq (\partial_2 u_3 - \partial_3 u_2, \partial_3 u_1 - \partial_1 u_3, \partial_1 u_2 - \partial_2 u_1)^\intercal . \tag{3.5}$$

The application of the Laplace operator (3.4) to a scalar function u

$$\mathcal{L}u(\boldsymbol{x}) \coloneqq -k\Delta u(\boldsymbol{x}) \tag{3.6}$$

is used to model potential problems such as electrostatics and steady-state heat conduction. For the latter the constant coefficient k denotes the conductivity and u the heat potential. The operator of the Lamé-Navier equation is defined by

$$\mathcal{L}\mathbf{u}(\boldsymbol{x}) := -\mu\Delta\mathbf{u}(\boldsymbol{x}) - (\lambda+\mu)\,\mathrm{grad}\,\mathrm{div}\,\mathbf{u}(\boldsymbol{x}) \tag{3.7}$$

with $\mathbf{u} \in \mathbb{R}^d$ denoting displacements. The Lamé-constants λ and μ are computed from the Young's modulus E and the Poisson's ratio ν of the considered material. In particular, the constants are defined as

$$\lambda = \frac{E\,\nu}{(1-2\,\nu)(1+\nu)} \qquad \text{and} \qquad \mu = \frac{E}{2\,(1+\nu)}. \tag{3.8}$$

In the subsequent sections, u will be used for both the heat potential and the displacement.

3.2 Fundamental Solutions

In general, a fundamental solution $\mathsf{U}(\boldsymbol{x},\boldsymbol{y})$ is the solution of

$$\mathcal{L}\mathsf{U}(\boldsymbol{x},\boldsymbol{y}) = \delta(r) \tag{3.9}$$

where $r = |\boldsymbol{x}-\boldsymbol{y}|$ is the Euclidean distance and $\delta(r)$ denotes the Dirac delta function

$$\delta(r) = \begin{cases} \infty & \text{for } r = 0 \\ 0 & \text{otherwise} \end{cases} \tag{3.10}$$

which also satisfies

$$\int_\Omega \delta(r)\,\mathrm{d}\Omega = 1 \qquad\qquad \boldsymbol{x},\boldsymbol{y} \in \Omega. \tag{3.11}$$

Equation (3.9) can be solved to provide the potential at the *field point* $\boldsymbol{y}$ due to a unit point source applied at $\boldsymbol{x}$, which is denoted as *source point*. The fundamental solution to the Laplace operator is given by [47]

$$\mathsf{U}(\boldsymbol{x},\boldsymbol{y}) = -\frac{1}{2\pi}\ln r \qquad \text{for } d = 2, \tag{3.12}$$

and

$$\mathsf{U}(\boldsymbol{x},\boldsymbol{y}) = \frac{1}{4\pi r} \qquad \text{for } d = 3. \tag{3.13}$$

Kelvin's fundamental solution for the Lamé-Navier equation is

$$\mathsf{U}_{ij}(\boldsymbol{x},\boldsymbol{y}) = \frac{1}{8\pi\mu\,(1-\nu)}\,(r_{,i}r_{,j} - (3-4\nu)\ln r\,\delta_{ij}) \qquad \text{for } d=2, \tag{3.14}$$

and

$$\mathsf{U}_{ij}(\boldsymbol{x},\boldsymbol{y}) = \frac{1}{16\pi\mu\,(1-\nu)\,r}\,(r_{,i}r_{,j} + (3-4\nu)\,\delta_{ij}) \qquad \text{for } d=3. \tag{3.15}$$

It is represented as a tensor with $i,j = \{1,\ldots,d\}$, where δ_{ij} denotes the Kronecker delta:

$$\delta_{ij} = \begin{cases} 1 & \text{if } i=j \\ 0 & \text{otherwise.} \end{cases} \tag{3.16}$$

It should be noted that the fundamental solutions depend on the distance $r = |\boldsymbol{x}-\boldsymbol{y}|$ rather than the actual location of the field and source points. Moreover, they tend to infinity if $r \to 0$.

3.3 Boundary Value Problem

Let $\Omega \in \mathbb{R}^d$ be a bounded domain defined by its boundary $\Gamma \coloneqq \partial\Omega$ and $\mathbf{n}$ the related outward normal. Furthermore, it is supposed that Γ is partitioned into a Neumann Γ_N and a Dirichlet part Γ_D, such that $\Gamma = \Gamma_N \cup \Gamma_D$ and $\Gamma_N \cap \Gamma_D = \emptyset$. For a given right hand side, $g_D \in \Gamma_D$ and $g_N \in \Gamma_N$, a mixed elliptic boundary value problem (BVP) can be defined: Find $u(\boldsymbol{x})$ such that

$$\mathcal{L}u(\boldsymbol{x}) = 0 \qquad \forall \boldsymbol{x} \in \Omega \tag{3.17}$$

$$\operatorname{Tr} u(\boldsymbol{x}) = u(\boldsymbol{y}) = g_D(\boldsymbol{y}) \qquad \forall \boldsymbol{y} \in \Gamma_D \tag{3.18}$$

$$\mathcal{T}u(\boldsymbol{x}) = t(\boldsymbol{y}) = g_N(\boldsymbol{y}) \qquad \forall \boldsymbol{y} \in \Gamma_N. \tag{3.19}$$

Note that the unknown $u(\boldsymbol{x})$ in the interior of Ω is represented by the *Cauchy* data on Γ, i.e. $u(\boldsymbol{y})$ and $t(\boldsymbol{y})$. In particular, the *boundary trace*

$$\operatorname{Tr} u(\boldsymbol{x}) = \lim_{\mathbf{x}\to\mathbf{y}} u(\boldsymbol{x}) = u(\boldsymbol{y}) \qquad \boldsymbol{x} \in \Omega,\ \boldsymbol{y} \in \Gamma \tag{3.20}$$

maps the primal field $u(\boldsymbol{x})$ in the domain Ω to $u(\boldsymbol{y})$ on the boundary. The *conormal derivative* $\mathcal{T}$ of the Laplace operator transforms the potential $u(\boldsymbol{x})$ to the flux along the boundary $t(\boldsymbol{y})$ by

$$\mathcal{T}u(\boldsymbol{x}) = k\nabla u(\boldsymbol{y}) \cdot \mathbf{n}(\boldsymbol{y}) = t(\boldsymbol{y}). \tag{3.21}$$

For the Lamé-Navier operator it is defined by

$$\mathcal{T}u(\boldsymbol{x}) = \lambda\nabla\cdot u(\boldsymbol{y})\mathbf{n}(\boldsymbol{y}) + 2\mu\nabla u(\boldsymbol{y})\cdot\mathbf{n}(\boldsymbol{y}) + \mu\,\mathbf{n}(\boldsymbol{y}) \times (\nabla \times u(\boldsymbol{y})) = t(\boldsymbol{y}) \tag{3.22}$$

which maps displacements $u(\boldsymbol{x})$ to surface traction $t(\boldsymbol{y})$.

3.4 Boundary Integral Equations

The homogeneous differential equation (3.17) can be solved by means of boundary integral equations. Using the fundamental solutions the *single layer potential*

$$u(\boldsymbol{x}) = \int_\Gamma \mathsf{U}(\boldsymbol{x},\boldsymbol{y})\phi(\boldsymbol{y})\ \mathrm{ds}_{\boldsymbol{y}} \qquad \boldsymbol{x}\in\Omega,\ \boldsymbol{y}\in\Gamma \tag{3.23}$$

and *double layer potential*

$$u(\boldsymbol{x}) = \int_\Gamma \mathcal{T}\mathsf{U}(\boldsymbol{x},\boldsymbol{y})\psi(\boldsymbol{y})\ \mathrm{ds}_{\boldsymbol{y}} \qquad \boldsymbol{x}\in\Omega,\ \boldsymbol{y}\in\Gamma \tag{3.24}$$

are introduced as an Ansatz for the solution u with the unknown *density functions* ϕ and ψ. The *kernel function* U satisfies the homogeneous differential equation, since it is the fundamental solution to the underlying differential operator of the problem. Applying the trace Tr to these potentials yields to the single layer

$$(\mathcal{V}\phi)(\boldsymbol{x}) = \int_\Gamma \mathsf{U}(\boldsymbol{x},\boldsymbol{y})\phi(\boldsymbol{y})\ \mathrm{ds}_{\boldsymbol{y}} \qquad \forall \boldsymbol{x},\boldsymbol{y}\in\Gamma \tag{3.25}$$

and double layer

$$(\mathcal{K}\psi)(\boldsymbol{x}) = \int_\Gamma \mathcal{T}\mathsf{U}(\boldsymbol{x},\boldsymbol{y})\psi(\boldsymbol{y})\ \mathrm{ds}_{\boldsymbol{y}} \qquad \forall \boldsymbol{x},\boldsymbol{y}\in\Gamma \tag{3.26}$$

boundary integral *operators*. The former integral is weakly singular, i.e. it is finite although its integrands tend to infinity as $\boldsymbol{y}$ approaches $\boldsymbol{x}$. The second integral operator is strongly singular in general and treated as Cauchy principal value, i.e. the integral in the neighborhood of the singularity $\boldsymbol{x}$ is calculated by a limiting process. This procedure causes an integral free jump term

$$(\mathcal{C}u)(\boldsymbol{x}). \tag{3.27}$$

On smooth surfaces the free term is given by

$$\mathcal{C} = \tfrac{1}{2}\mathcal{I} \tag{3.28}$$

where $\mathcal{I}$ denotes the identity, i.e. $\mathcal{I}u(\boldsymbol{x}) = u(\boldsymbol{x})$. For non-smooth surfaces, it depends on the geometrical angle at $\boldsymbol{x}$ and the Poisson's ratio for elasticity [47, 79].

Remark: It is noteworthy that the integral kernel of the double layer operator is zero at the singularity in case of the Laplace equation. As a consequence the integral is also weakly singular. In general, the calculation of the integral free term can be avoided by the application of regularization techniques, e.g. as described in [13].

Based on the operators (3.25) and (3.26) boundary integral equations of the first

$$u(\boldsymbol{x}) = (\mathcal{V}\phi)(\boldsymbol{x}) \qquad \forall \boldsymbol{x} \in \Gamma \tag{3.29}$$

or the second kind

$$u(\boldsymbol{x}) = ((\mathcal{C} + \mathcal{K})\psi)(\boldsymbol{x}) \qquad \forall \boldsymbol{x} \in \Gamma \tag{3.30}$$

can be derived. These *indirect* formulations are solved for the unknown densities ϕ and ψ which are usually non-physical quantities. The actual solution of the BVP is obtained by the corresponding potentials (3.23) and (3.24), respectively.

In order to work with physical quantities u and t on the boundary Γ only, the BVP is solved by means of a *direct* boundary integral formulation

$$((\mathcal{C} + \mathcal{K})u)(\boldsymbol{x}) = (\mathcal{V}t)(\boldsymbol{x}) \qquad \forall \boldsymbol{x} \in \Gamma \tag{3.31}$$

instead. Once equation (3.31) is solved all Cauchy data are known and $u(\boldsymbol{x})$ within the domain is obtained by the representation formula

$$u(\boldsymbol{x}) = \int_\Gamma \mathsf{U}(\boldsymbol{x}, \boldsymbol{y})\, t(\boldsymbol{y})\, \mathrm{ds}_{\boldsymbol{y}} - \int_\Gamma \mathsf{T}(\boldsymbol{x}, \boldsymbol{y})\, u(\boldsymbol{y})\, \mathrm{ds}_{\boldsymbol{y}} \qquad \forall \boldsymbol{x} \in \Omega,\ \forall \boldsymbol{y} \in \Gamma \tag{3.32}$$

where T is the fundamental solution for the traction or flux which is determined by the conormal derivative with respect to the $\boldsymbol{y}$ variable, i.e. $\mathsf{T}(\boldsymbol{x}, \boldsymbol{y}) = \mathcal{T}_{\boldsymbol{y}}\mathsf{U}(\boldsymbol{x}, \boldsymbol{y})$. In elastostatics, the representation formula is referred to as *Somigliana's identity*.

If not stated otherwise, the direct boundary integral formulation (3.31) will be considered in the remainder of this thesis.

4 Discretization of Boundary Integral Equations

In general, the boundary integral equations presented in Chapter 3 can not be solve analytically. Hence, numerical methods are applied to solve the BIEs approximately. This thesis is dedicated to the collocated boundary element method and the quadrature based method introduced by Nyström. Beer et al. [14] and Gaul et al. [47] provide excellent basis for the former, whereas the introduction of Peterson and Bibby [92] or Gedney and Young [49] is recommended for the latter. In this chapter, these numerical approximation methods are embedded into *isogeometric analysis*, that is, the functions of CAGD are used for the description of the geometry and the approximation of the Cauchy data.

4.1 Geometry Representation

Following the isogeometric concept, the approximation of the computational domain's boundary Γ is obtained by a disjointed set of NURBS patches γ such that

$$\Gamma \approx \Gamma_h = \bigcup_{i=1}^{I} \gamma_i. \tag{4.1}$$

For the moment, it is assumed that the patches are not trimmed and the treatment of trimmed patches will be discussed later in Chapter 6. However, it should be noted that this set of NURBS patches (4.1) is equivalent to the boundary representation (2.26) of design models which are often starting point for the description of physical problems. Moreover, they provide the best geometry representation available. As a result the computational boundary is described as accurate as possible, so that $\Gamma_h = \Gamma$.

Any point $\boldsymbol{x} \in \Gamma$ can be evaluated within the corresponding patch by the geometrical mapping

$$\mathcal{X}(\boldsymbol{r}) : \mathbb{R}^{d-1} \mapsto \mathbb{R}^d \tag{4.2}$$

which maps local coordinates $\mathbf{r} = (r_1, \ldots, r_{d-1})^\intercal$ to the global coordinates $\boldsymbol{x} = (x_1, \ldots, x_d)^\intercal$ in the d-dimensional Cartesian system. For the sake of notational simplicity, the geometric mappings introduced in Section 2.2 and Section 2.3 are generalized to

$$\mathcal{X}(\boldsymbol{r}) := \boldsymbol{x}(\boldsymbol{r}) = \sum_{k=1}^{K} \theta_k(\boldsymbol{r})\, \boldsymbol{c}_k \tag{4.3}$$

where K denotes the total number of B-spline or NURBS basis functions θ_k, which are either univariate or bivariate. It is assumed that the mapping (4.3) is valid, i.e. the related Gram's determinant defined by

$$G(\boldsymbol{r}) = \sqrt{\det\left(\mathbf{G}(\boldsymbol{r})\right)} \qquad \text{with} \qquad \mathbf{G}(\boldsymbol{r}) := \mathbf{J}_{\mathcal{X}}^{\intercal}(\boldsymbol{r})\, \mathbf{J}_{\mathcal{X}}(\boldsymbol{r}) \in \mathbb{R}^{(d-1)\times(d-1)} \tag{4.4}$$

is non-singular. The corresponding Gram matrix $\mathbf{G}(\boldsymbol{r})$ consists of the Jacobi-matrix

$$\mathbf{J}_{\mathcal{X}}(\boldsymbol{r}) \coloneqq \left(\frac{\partial \mathcal{X}_i}{\partial r_j} \right) \qquad \text{with} \qquad i = 1, \ldots, d \qquad \text{and} \qquad j = 1, \ldots, d-1 \tag{4.5}$$

which results from the geometrical mapping [102]. In general this assumption holds, but in fact, it is not fulfilled if a patch is evaluated directly at an edge which degenerates to a point. However, it will be shown in the subsequent sections that even degenerated patches are analysis suitable, if they are solely evaluated at valid points.

Remark: Points where the geometric mapping is not valid are also referred to as EV or extraordinary vertices in CAGD. They are of particular interest in the context of subdivision surfaces and T-splines.

4.1.1 Integration Elements

Each non-zero knot span defines a different segment of its patch γ. Moreover, knots indicate locations which are not C^∞-continuous. In order to perform the numerical integration properly, the integrands must be smooth within each integration interval. Consequently, each non-zero knot span is defined as *integration element* τ. The quadrature points are specified within the reference element $\hat{\tau} = [-1, 1]^{d-1}$ with the intrinsic coordinates $\boldsymbol{\xi}$. The coordinate transformation from $\hat{\tau}$ to the parameter space of τ is denoted by $\mathcal{X}_\xi(\boldsymbol{\xi})$. A proper distribution of quadrature points over a B-spline curve is illustrated in Figure 4.1.

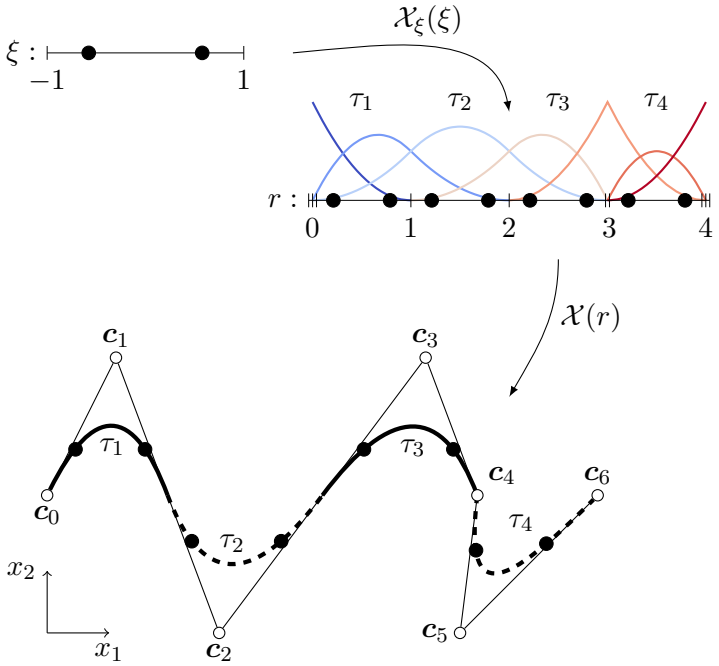

Figure 4.1: Distribution of quadrature points over a B-spline curve defined by the knot vector $\Xi = \{0, 0, 0, 1, 2, 3, 3, 4, 4, 4\}$ and the control points $\boldsymbol{c}_i$. Each element τ_j is subjected to a two point quadrature rule defined in the reference interval $\xi \in [-1, 1]$. The quadrature points are indicated by black circles.

4.2 Isogeometric Nyström Method

The Nyström method is a quadrature based method where the boundary integral operators are approximated by means of a numerical integration [72]. In general, numerical quadratures approximate an integral, $I = \int_a^b f(s)\,\mathrm{d}s$, by a sum over quadrature weights w_q and evaluations at quadrature points s_q

$$I \approx I_Q = \sum_{q=1}^{Q} f(s_q) w_q. \tag{4.6}$$

Usually, the quadratures are constructed by replacing the integrand f by an interpolation polynomial with respect to s_q. The approximation I_Q converges to I as $Q \to \infty$. Another way to improve the quality of I_Q is to subdivide the integration interval into several parts leading to a *composite* quadrature scheme. The quadrature weights w_q are obtained by analytic integration of the underlying interpolation polynomial. For example, Lagrange polynomials with equidistant interpolation points lead to the classical Newton-Cotes formulae. The corresponding convergence rate is related to the order p_q of the quadrature which is defined by the highest polynomial degree that it integrates exactly.

In his original paper [88], Nyström proposed to discretize second kind integral equations (3.30) by means of a numerical quadrature

$$((\mathcal{C} + \mathcal{K})\psi)(\boldsymbol{x}_i^c) \approx c\psi_h(\boldsymbol{x}_i^c) + \sum_{q=1}^{Q} \mathcal{T}\mathsf{U}(\boldsymbol{x}_i^c, \boldsymbol{y}_q)\psi_h(\boldsymbol{y}_q) w_q \qquad \boldsymbol{x}_i^c,\ \boldsymbol{y}_q \in \Gamma \tag{4.7}$$

where $\boldsymbol{y}_q$ are the corresponding evaluation points. Thereby, the solution ψ of the integral equation is replaced by the solution ψ_h of a finite dimensional linear system [72]. In order to set up a system of equations, the quadrature sum (4.7) is enforced at distinct points $\boldsymbol{x}_i^c$ with $i = 1, \ldots, Q$. For the remainder of this thesis, these points are referred to as *collocation points*. The solution of the obtained system of equations represents point-wise results at $\boldsymbol{x}_i^c$. The results along the remaining boundary are determined by the application of an interpolation scheme.

4.2.1 Discretization of Cauchy Data

In order to evaluate the boundary integral adequately, the patch γ is subdivided into a set of integration elements τ, so that

$$\gamma = \bigcup_{i=1}^{I} \tau_i. \tag{4.8}$$

A distinguishing feature of the Nyström method is that the element-wise discretization of the Cauchy data is directly expressed through points on the geometry defined by the applied quadrature rule. In particular, the present formulation applies Gauss-Legendre quadrature formulae. The motivation for this choice is twofold: firstly, they require the minimal

number of quadrature points to obtain results for a certain quadrature order p_q. Moreover, they are open quadratures, i.e. the quadrature points are not located at the boundary of the integration region. Consequently, there is no evaluation at physical corners or edges, where the integral kernel may be undefined or diverging. Furthermore, the application of a composite quadrature is straightforward. In particular, the quadrature points are distributed within each integration element with respect to their coordinates $\boldsymbol{\xi} \in [-1,1]^{d-1}$ in the reference element. To compute their location $\boldsymbol{y}$ on τ in the physical space, the mappings $\mathcal{X}_\xi(\boldsymbol{\xi})$ for the reference element and $\mathcal{X}(\boldsymbol{r})$ for the geometry are consecutively applied as depicted in Figure 4.1.

It is noteworthy that the Cauchy data are not expressed in terms of variables at control points, in contrast to other isogeometric methods. For the analysis with the isogeometric Nyström method, Cauchy data are taken from evaluations at the quadrature points $\boldsymbol{y} \in \Gamma$ directly.

4.2.2 Collocation

The integral equation is enforced at the collocation points $\boldsymbol{x}^c$ which are the quadrature points, i.e. $\boldsymbol{x}^c \equiv \boldsymbol{y}$, so one obtains as many equations as unknowns. For the approximated integral equation of second kind (4.7) the matrix equation is

$$\left(\mathbf{C} + \tilde{\mathbf{K}}\right) \boldsymbol{\psi} = \mathbf{f} \tag{4.9}$$

for a given right hand side $\mathbf{f}$. The matrix $\tilde{\mathbf{K}}$ denotes the discrete double layer operator and the matrix $\mathbf{C}$ contains the integral free terms. For boundary integral equations of the first kind (3.29), the system is

$$\mathbf{V}\boldsymbol{\phi} = \mathbf{f} \tag{4.10}$$

with the discrete single layer operator $\mathbf{V}$. For a direct formulation (3.31) with mixed boundary conditions, a block system of equations

$$\begin{matrix} \boldsymbol{x}^c \in \Gamma_D: \\ \boldsymbol{x}^c \in \Gamma_N: \end{matrix} \quad \begin{pmatrix} \mathbf{V}_{DD} & -\mathbf{K}_{DN} \\ \mathbf{V}_{ND} & -\mathbf{K}_{NN} \end{pmatrix} \begin{pmatrix} \mathbf{t}_D \\ \mathbf{u}_N \end{pmatrix} = \begin{pmatrix} \mathbf{K}_{DD} & -\mathbf{V}_{DN} \\ \mathbf{K}_{ND} & -\mathbf{V}_{NN} \end{pmatrix} \begin{pmatrix} \mathbf{g}_D \\ \mathbf{g}_N \end{pmatrix} \tag{4.11}$$

is obtained in an analog manner to the formulation presented in [135]. If integral free terms are present, they are already integrated in the system matrices $\mathbf{K}$. The first subscript indicates if the collocation point $\boldsymbol{x}_i^c$ is either on a Dirichlet (D) or Neumann (N) boundary, whereas the second one corresponds to the quadrature point $\boldsymbol{y}_j$. If the surface Γ is smooth and the kernel function U is regular, entries of the system matrix only consist of point-wise evaluations

$$\mathbf{V}[i,j] = \mathsf{U}(\boldsymbol{x}_i^c, \boldsymbol{y}_j) w_j \qquad \text{and} \qquad \mathbf{K}[i,j] = \delta_{ij} c + \mathcal{T}\mathsf{U}(\boldsymbol{x}_i^c, \boldsymbol{y}_j) w_j. \tag{4.12}$$

Since the present formulation applies an open quadrature rule, the collocation points always lie on a smooth surfaces. Hence, the integral free term is $c = \frac{1}{2}$. However, the kernel functions for the applications considered are undefined if $\boldsymbol{x}_i^c = \boldsymbol{y}_j$ so that special treatment is necessary to evaluate the corresponding system matrix entries.

4.2.3 Evaluation of System Matrix Coefficients

In the present implementation, Gauss-Legendre quadrature rules are used. For the analysis in three dimensions, a tensor product quadrature is constructed. However, it is also feasible to apply non-tensor product quadratures or numerical quadratures constructed for special purposes [19].

As mentioned in Chapter 3, the integral kernels are singular if collocation and quadrature point coincide. Such kernels require special treatment for a correct integration. For the isogeometric Nyström method, a spatial separation of quadrature points in relation to each collocation point is performed. An admissibility criterion

$$\operatorname{diam}(\tau) \leqslant \eta \operatorname{dist}(\boldsymbol{x}_i^c, \boldsymbol{y}_j) \tag{4.13}$$

is introduced which separates the region with a smooth kernel function from that one with singular or nearly singular behavior. If condition (4.13) is fulfilled, the corresponding entries are in the scope of the *far field* where the system matrices consist of point evaluations only. The other region is denoted as *near field* and is subjected to a regularization procedure.

4.2.3.1 Far Field Evaluation

Considering the discrete single layer operator, a matrix entry for the isogeometric Nyström method is

$$\mathbf{V}[i,j] = \mathsf{U}(\boldsymbol{x}_i^c, \boldsymbol{y}_j) G(\boldsymbol{r}_j) J_{\mathcal{X}_\xi}(\boldsymbol{\xi}_j) w_j \tag{4.14}$$

where $\mathsf{U}(\boldsymbol{x}_i^c, \boldsymbol{y}_j)$ is the evaluation of the fundamental solution with respect to the collocation point $\boldsymbol{x}_i^c$ and the quadrature point $\boldsymbol{y}_j$. Gram's determinant $G(\boldsymbol{r}_j)$ is defined by the location $\boldsymbol{r}_j$ of $\boldsymbol{y}_j$ in the parametric space. For the integral transformation from reference to integration element, the Jacobian of the mapping $\mathcal{X}_\xi$

$$J_{\mathcal{X}_\xi}(\boldsymbol{\xi}_j) = \det(\mathbf{J}(\boldsymbol{\xi}_j)) \tag{4.15}$$

is evaluated with respect to the reference coordinates $\boldsymbol{\xi}_j$ of the quadrature point $\boldsymbol{y}_j$. Finally, w_j in equation (4.14) denotes the regular weight of the quadrature formula applied.

4.2.3.2 Near Field Evaluation

Based on a technique for the construction of quadrature rules with arbitrary order for given singular functions, presented in [117], the authors of [28] developed the *locally corrected* Nyström method for the solution of the Helmholtz equation. This particular regularization technique is used for the framework presented in this thesis. The main idea is to replace the contribution of the original kernel function in the neighborhood $\Omega_{\boldsymbol{x}^c}$ of the collocation point $\boldsymbol{x}_i^c$ with a corrected regular one. As a result, a new kernel function is defined by

$$\mathsf{U}^*(\boldsymbol{x}_i^c, \boldsymbol{y}_j) = \begin{cases} \mathsf{L}(\boldsymbol{x}_i^c, \boldsymbol{y}_j) & \text{if } \boldsymbol{x}_i^c \in \Omega_{\boldsymbol{x}^c} \\ \mathsf{U}(\boldsymbol{x}_i^c, \boldsymbol{y}_j) & \text{otherwise.} \end{cases} \tag{4.16}$$

The locally corrected kernel L for the collocation point $\boldsymbol{x}_i^c$ is computed at the corresponding quadrature points $\boldsymbol{y}_j \in \Omega_{\boldsymbol{x}^c}$ by solving the linear system

$$\sum_{j=1}^{J} N_k(\boldsymbol{y}_j) L(\boldsymbol{x}_i^c, \boldsymbol{y}_j) w_j = \int\limits_{\Gamma \cap \Omega_{\boldsymbol{x}^c}} \mathsf{U}(\boldsymbol{x}_i^c, \boldsymbol{y}) N_k(\boldsymbol{y}) \, \mathrm{ds}_{\boldsymbol{y}} \qquad \text{with} \qquad k = 1, \dots, K. \tag{4.17}$$

Equation (4.17) introduces a space of K test functions N_k, hence the singularity of the original kernel is treated in a weak sense on the right hand side. In fact, a tailored numerical quadrature is constructed, where the weights w_j are not explicitly calculated but multiplied with the corrected kernel, i.e. $\tilde{w}_j = L(\boldsymbol{x}_i^c, \boldsymbol{y}_j) w_j$. Finally, the linear system in matrix form is given by

$$\mathbf{N}\tilde{\mathbf{w}} = \mathbf{f} \qquad \text{with} \qquad \mathbf{N} \in \mathbb{R}^{K \times J}, \; \tilde{\mathbf{w}} \in \mathbb{R}^{J}, \; \mathbf{f} \in \mathbb{R}^{K}. \tag{4.18}$$

The matrix $\mathbf{N}$ consists of evaluations of the test functions and $\mathbf{f}$ contains the accurately evaluated right hand side of equation (4.17).

Following the isogeometric concept, we propose using B-splines as test functions, i.e. $N_k = B_{k,p}$, which are defined on the integration element τ. In particular, a Bézier patch is constructed where the corresponding basis functions are specified by knot vectors of the kind

$$\Xi = \{-1, \dots, -1, 1, \dots, 1\} \tag{4.19}$$

in each parametric direction. The multiplicity of the knots is chosen such that they define at least as many basis functions as present quadrature points on the integration element. This allows to solve equation (4.17) by means of LU-decomposition or as a least squares problem.

The integrals of the right hand side are

$$\int\limits_{\tau} \mathsf{U}(\boldsymbol{x}_i^c, \boldsymbol{y}) B_{k,p}(\boldsymbol{y}) \, \mathrm{ds}_{\boldsymbol{y}} \qquad \text{or} \qquad \int\limits_{\tau} \mathcal{T}_{\boldsymbol{y}} \mathsf{U}(\boldsymbol{x}_i^c, \boldsymbol{y}) B_{k,p}(\boldsymbol{y}) \, \mathrm{ds}_{\boldsymbol{y}} \tag{4.20}$$

for the single and double layer operators, respectively. If $\boldsymbol{x}_i^c \in \tau$ the integrals are singular. In that case the single layer integral is subject to coordinate transformations as described in [73] and [42] while the double layer integral is treated with regularization techniques presented in [54]. If $\boldsymbol{x}_i^c \notin \tau$ but condition (4.13) is not fulfilled, the integral is nearly singular and treated with an adaptive numerical integration. This procedure is also required in the context of BEM analysis and described in the subsequent Section 4.3.3.2. In practical terms, the extent of the region where elements are marked as nearly singular is determined by the admissibility factor η of equation (4.13).

It should, however, be pointed out that the application of the local correction leads to a quadrature order of $p_q = Q$ with Q denoting the number of quadrature points $\boldsymbol{y}_j$ used per integration element [117]. Despite the fact that Gauss quadratures reach higher orders for regular integrals, i.e. $p_q = 2Q - 1$.

4.2.4 Geometric Requirements

The applied quadrature scheme is chosen to be of open type. This particular choice brings an advantage: due to its point-wise nature, the Nyström method does not require any connectivities between patches. Hence, non-conforming patches are inherently supported.

Nevertheless, the Nyström method requires smooth surfaces to converge with respect to the order of the underlying quadrature. Isogeometric analysis is capable to fulfill this requirement, in contrast to conventional simulations based on triangulations. However, real-world geometries still contain corners and edges by design. They can be easily identified by the multiplicity of knots, i.e. $m = p$, of the related knot vectors. In order to retain higher order convergence, the integration regions adjacent to corners or edges are graded. According to Atkinson [5] the particular interval $[r_s, r_{s+1}]$ is subdivided into ℓ elements by introducing new parameter values $\hat{r}_i$ specified as

$$\hat{r}_i = r_s + (r_{s+1} - r_s)\left(\frac{i}{\ell}\right)^{\alpha} \qquad \text{and} \qquad \hat{r}_i = r_{s+1} - (r_{s+1} - r_s)\left(\frac{i}{\ell}\right)^{\alpha} \tag{4.21}$$

for grading towards r_s or r_{s+1}, respectively. The exponent α is given by

$$\alpha \geqslant \frac{p_q + 1}{\upsilon} \qquad \text{with} \qquad 0 < \upsilon \leqslant 1 \tag{4.22}$$

where p_q is the order of the quadrature rule and υ denotes the Hölder constant. This grading is also applied if the boundary conditions change abruptly.

4.2.5 Postprocessing

Once the system of equations is solved, the Cauchy data exist only in the quadrature points $\boldsymbol{y}_j$. Thus a postprocessing step is required to visualize the distribution over the whole geometry. The Nyström-interpolation [5] is the most accurate procedure for this task. But it requires additional kernel evaluations at all quadrature points, which is computationally expensive. For the isogeometric Nyström method, the following approach is probably less accurate but simpler and local to the integration elements τ. Following the isogeometric concept, each element τ is represented by the Bézier patch already constructed for the local correction. The results in the corresponding quadrature points $\boldsymbol{y}_j$ are interpolated within each τ by means of the basis functions $B_{i,p}$ based on a knot vector of form (4.19). For instance, the primary variable u in any point $\boldsymbol{\xi}$ of the reference element can be calculated with

$$u(\boldsymbol{\xi}) = \sum_{i=0}^{I} B_{i,p}(\boldsymbol{\xi})\, \boldsymbol{c}_i. \tag{4.23}$$

In order to compute the unknown coefficients $\boldsymbol{c}_i$ a spline interpolation problem is solved.

4.3 Isogeometric Boundary Element Method

Boundary element methods can be classified as *methods of weighted residuals*. The residual of a differential equation $\mathcal{L}u = f$ is given by

$$\epsilon \coloneqq \mathcal{L}u_h - f \tag{4.24}$$

where u_h is the numerically obtained approximated solution. Note that ϵ is zero, if $u_h = u$. The approximation u_h is defined within a finite dimensional subspace $\mathbb{S}_h$ that is believed to be close to the original solution space. In particular, $u_h(\boldsymbol{x})$ can be written as

$$u_h(\boldsymbol{x}) = \sum_{i=1}^{I} \phi_i(\boldsymbol{x})\, a_i \tag{4.25}$$

with ϕ spanning the basis $\{\phi_1, \ldots, \phi_I\}$ of the I-dimensional space $\mathbb{S}_h$. The corresponding coefficients a_i are determined by the requirement that the integral over the residual $\epsilon(\boldsymbol{x})$ multiplied with weighting functions $\omega_j(\boldsymbol{x})$ becomes zero [47], i.e.

$$\int_\Omega \epsilon(\boldsymbol{x})\omega_j(\boldsymbol{x})\, \mathrm{d}\boldsymbol{x} = 0, \qquad \forall \omega_j,\ j = i, \ldots, I. \tag{4.26}$$

If the weighting functions are chosen to be equivalent to the basis functions of the approximation, i.e. $\omega_i \equiv \phi_i$, the classical *Galerkin* method is obtained. The *collocation* approach, on the other hand, enforces the boundary integral equation at a certain set of collocation points $\boldsymbol{x}^c$ so that

$$\epsilon(\boldsymbol{x}_j^c) = 0, \qquad \forall \boldsymbol{x}_j^c,\ j = i, \ldots, I \tag{4.27}$$

or rather

$$\int_\Omega \epsilon(\boldsymbol{x})\delta(\boldsymbol{x} - \boldsymbol{x}_j^c)\, \mathrm{d}\boldsymbol{x} = 0, \qquad \forall \boldsymbol{x}_j^c,\ j = i, \ldots, I. \tag{4.28}$$

where $\delta(\boldsymbol{x} - \boldsymbol{x}_j^c)$ denotes the Dirac delta function (3.10). Apparently, the location of these collocation points is crucial and will be outlined later in this chapter.

4.3.1 Discretization of Cauchy Data

In order to provide a coherent terminology, we use the notation for the solution of the Lamé-Navier equation. In this case, the Cauchy data are vector valued, i.e. $\mathbf{u} = (u_1, \ldots, u_d)^\intercal$ and $\mathbf{t} = (t_1, \ldots, t_d)^\intercal$. Within each patch the Cauchy data are represented by

$$\mathcal{Y}_u(\boldsymbol{r}) := \mathbf{u}(\boldsymbol{r}) = \sum_{i=1}^{I} \varphi_i(\boldsymbol{r})\, \tilde{\mathbf{u}}_i \qquad \text{and} \qquad \mathcal{Y}_t(\boldsymbol{r}) := \mathbf{t}(\boldsymbol{r}) = \sum_{j=1}^{J} \psi_j(\boldsymbol{r})\, \tilde{\mathbf{t}}_j. \tag{4.29}$$

The coefficients $\tilde{\mathbf{u}}_i$ and $\tilde{\mathbf{t}}_j$ are the control parameters of the corresponding field and the related basis functions are denoted by φ_i and ψ_j. The mapping $\mathcal{Y}$ is similar to the geometric

mapping (4.3) and the distinction will be important later in Chapter 5. In this chapter, attention is given to the fact that control parameters are not interpolatory, i.e. do not lie on their patch. Hence, the known Cauchy data on the boundary, i.e. $\mathbf{g}_N$ and $\mathbf{g}_N$, can not be applied directly but have to be expressed by means of the control parameters $\tilde{\mathbf{g}}_N$ and $\tilde{\mathbf{g}}_D$. If the whole NURBS patch has either Neumann or Dirichlet boundary conditions it can be easily obtained by the inverse of the mappings (4.29) with

$$\tilde{\mathbf{g}}_D = \mathcal{Y}_u^{-1}\mathbf{g}_D \qquad \text{and} \qquad \tilde{\mathbf{g}}_N = \mathcal{Y}_t^{-1}\mathbf{g}_N. \tag{4.30}$$

In addition, the appropriate choice of the location of collocation points for the unknown $\tilde{\mathbf{u}}_i$ and $\tilde{\mathbf{t}}_j$ is of particular interest and addressed in the next section.

4.3.2 Collocation

The so-called spline collocation method was used to develop estimates for the stability [108] and convergence of collocated boundary element methods in two [3, 4, 100, 101] and three dimensions [2, 33]. Most of these papers focus on uniform or smoothly graded knot intervals on closed curves. For curves with odd degree p, collocation at the knots was applied, whereas collocation in the middle of a knot span was employed for even p. Since the ascent of isogeometric analysis more complex splines are used, which are usually based on open knot vectors with arbitrary knot spacing. Hence, collocation at knots or midpoints would not suffice.

In the following, the collocation points are generally defined by the anchors $\bar{\boldsymbol{r}}$ of the used basis function, i.e. $\boldsymbol{x}_i^c = \mathcal{X}(\bar{\boldsymbol{r}}_i)$. In particular, the Greville abscissae are used. It has been demonstrated that this is a robust and accurate choice [6, 75, 82]. In fact, it agrees with the approach previously mentioned, since using Greville abscissae leads to collocation at knots and midpoints for odd and even p as well, if the knot vector is uniform.

Remark: The Demko abscissa is the optimal choice for spline interpolation problems. However, in the context of collocated BEM it may lead to numerical complications if B-splines of odd degree are used. See Appendix A.3 for a more detailed discussion.

The system of equations is set up by collocating at the anchors of the basis functions approximating the unknown field. It can be represented by a block system of matrices [135] by sorting the equations with respect to the Dirichlet and Neumann boundary, leading to

$$\begin{matrix} \boldsymbol{x}^c \in \Gamma_D: \\ \boldsymbol{x}^c \in \Gamma_N: \end{matrix} \quad \begin{pmatrix} \mathbf{V}_{DD} & -\mathbf{K}_{DN} \\ \mathbf{V}_{ND} & -\mathbf{K}_{NN} \end{pmatrix} \begin{pmatrix} \tilde{\mathbf{t}}_D \\ \tilde{\mathbf{u}}_N \end{pmatrix} = \begin{pmatrix} \mathbf{K}_{DD} & -\mathbf{V}_{DN} \\ \mathbf{K}_{ND} & -\mathbf{V}_{NN} \end{pmatrix} \begin{pmatrix} \tilde{\mathbf{g}}_D \\ \tilde{\mathbf{g}}_N \end{pmatrix}. \tag{4.31}$$

This system of equations represents the discretized boundary integral equation (3.31). In particular, $\mathbf{V}$ denotes the discretized single layer and $\mathbf{K}$ represents the double layer operator and the integral free jump term. For the sake of simplicity $\mathbf{K}$ is broadly referred to as discretized double layer operator. The first subscript indicates the boundary type which corresponds to the collocation point. Likewise, the second subscript denotes the boundary type related to the integrated element or more precisely its basis functions. Hence, the

matrix coefficients are determined by

$$\mathbf{V}_{RC}[i,j] = (\mathcal{V}\psi_j)(\boldsymbol{x}_i^c) \qquad \text{and} \qquad \mathbf{K}_{RC}[i,j] = ((\mathcal{C}+\mathcal{K})\varphi_j)(\boldsymbol{x}_i^c) \tag{4.32}$$

where $\boldsymbol{x}_i^c \in \Gamma_R$ and $\psi_j, \varphi_j \in \Gamma_C$.

4.3.3 Evaluation of System Matrix Coefficients

4.3.3.1 Regular Integration

The system matrix coefficients (4.32) are evaluated by numerical integration. Each entry corresponds to a basis function which spans over up to $p+1$ integration elements τ. For instance, the entry for the collocation point $\boldsymbol{x}_i^c$ and the basis function ψ_j is obtained by a sum of integrals

$$\mathbf{V}[i,j] = \sum_{k=1}^{K} I_{\tau_k} = \sum_{k=1}^{K} \int_{\tau_k} \mathsf{U}(\boldsymbol{x}_i^c, \boldsymbol{y})\psi_j(\boldsymbol{y}) \, \mathrm{ds}_{\boldsymbol{y}} \tag{4.33}$$

where I_{τ_k} is the contribution of the element τ_k. The integration is performed for example with standard Gauss-Legendre quadrature. For each τ_k this yields to

$$I_{\tau_k} \approx \sum_{q=1}^{Q} \mathsf{U}\left(\boldsymbol{x}_i^c, \boldsymbol{y}_q\right) \psi_j(\boldsymbol{y}_q) G(\boldsymbol{r}_q) J_{\mathcal{X}_\xi}(\boldsymbol{\xi}_q) w_q \tag{4.34}$$

where w_q are the integration weights of related integration point $\boldsymbol{y}_q = \mathcal{X}(\boldsymbol{r}_q) = \mathcal{X}(\mathcal{X}_\xi(\boldsymbol{\xi}_q))$ defined by its coordinates $\boldsymbol{\xi}_q$ within the reference element $\hat{\tau}$. Gram's determinant (4.4) for the integration points is denoted by $G(\boldsymbol{r}_q)$ and the Jacobian of the integral transformation $\mathcal{X}_\xi$ from $\hat{\tau}$ to τ is given by

$$J_{\mathcal{X}_\xi}(\boldsymbol{\xi}_q) = \det\left(\mathbf{J}(\boldsymbol{\xi}_q)\right). \tag{4.35}$$

4.3.3.2 Nearly Singular Integration

The integrand includes the fundamental solution which tends to infinity as the integration point approaches the collocation point, i.e. $w_q \to \boldsymbol{x}_i^c$. In order to integrate the steep gradient near the singularity, affected elements are further subdivided into integration regions as illustrated in Figure 4.2. Regular integration is used within each of these regions. For more detailed information on the implemented subdivision scheme the interested reader is referred to [82].

4.3.3.3 Singular Integration

Regular integration schemes can not be applied, if a collocation point $\boldsymbol{x}_i^c$ is located within the current integration element. Hence, the region where the boundary integral becomes singular is subjected to regularization techniques. The weakly singular integral of the discretized single layer operator $\mathbf{V}$ is subject to coordinate transformations according to

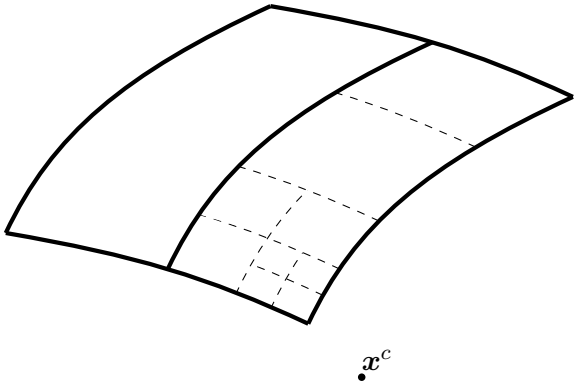

Figure 4.2: Subdivision of an element close to a collocation point $\boldsymbol{x}^c$. The actual elements are indicated by continuous lines, whereas the introduced integration regions are denoted by dashed lines.

[73] and [42]. The strongly singular integral of the discretized double layer operator $\mathbf{K}$ is treated with regularization techniques presented in [54]. For more detailed information on the implemented treatment of singular integrals is referred to [82].

4.3.4 Geometric Requirements

So far it was tacitly assumed that the whole boundary Γ is smooth. In this section, it is focused on the situation when Γ contains C^0-continuities, i.e. corners and edges, which are denoted by Γ^0.

First of all, the integral free term has to be calculated accordingly to Mantic [79], if $\boldsymbol{x}_i^c \in \Gamma^0$. Moreover, the traction along Γ^0 is discontinuous since the outward normal $\mathbf{n}$ jumps there. In order to approximate the traction accurately, discontinuous basis functions are introduced. In particular, interpolatory basis functions are modified by means of knot insertion so that C^0 knots become C^{-1}-continuous. The Greville abscissae $\bar{\boldsymbol{r}}^g$ related to these discontinuous basis functions coincide. If they would be used as collocation points the resulting system of equations would become singular. Hence, the definition of *discontinuous anchors* is introduced.

Discontinuous Anchors Anchors $\bar{\boldsymbol{r}}_i$ of basis functions, e.g. ψ_i, are generally defined by the Greville abscissae. In case of discontinuous basis functions an additional offset α is applied to their parametric location. This offset is specified by an adaptation of the 2-ring collocation scheme presented in [109]. It is given for each parametric direction by

$$\alpha_i = \frac{\sum_{k=1}^{K} \bar{r}_{i-k}^e - \bar{r}_i^e + \sum_{k=1}^{K} \bar{r}_{i+k}^e - \bar{r}_i^e}{2K+1} \tag{4.36}$$

with

$$\bar{r}^e = \Xi_\psi \bigcup \bar{r}^g, \qquad \bar{r}_j^e \leqslant \bar{r}_{j+1}^e \qquad \text{and} \qquad K = \begin{cases} 1 & \text{if } (p-1) < 2 \\ 2 & \text{otherwise.} \end{cases}$$

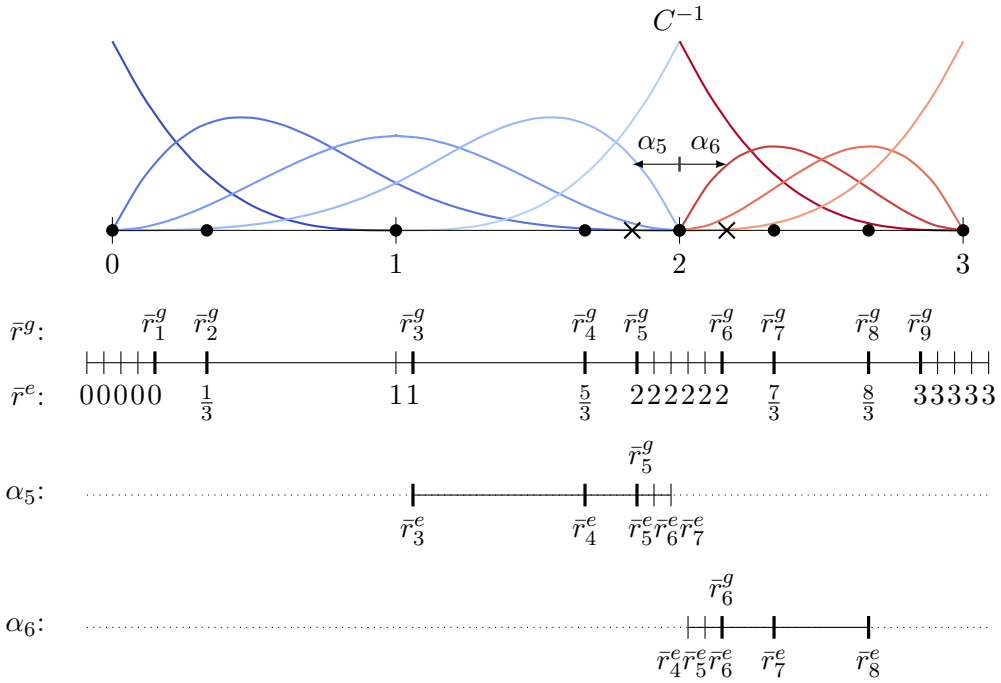

Figure 4.3: Definition and numbering of the sequence $\bar{r}^e$ for the construction of offsets α_5 and α_6. The basis is defined by $\Xi = \{0,0,0,0,1,2,2,2,2,3,3,3,3\}$. The Greville abscissae are marked by circles or thicker ticks. The final position of the shifted anchors $\bar{r}_5$ and $\bar{r}_6$ is indicated by crosses.

The values $\bar{r}^e$ represent an extension of the knot vector Ξ_ψ, which includes the corresponding Greville abscissae $\bar{r}^g$. In general, $\bar{r}^e$ is sorted in a non-decreasing order. Furthermore, Greville abscissae located at discontinuous knots, i.e. $m = p + 1$, are inserted at the beginning and the end of these knots. In equation (4.36) the index i is related to the discontinuous ψ_i considered and its $\bar{r}_i^g$. Consequently, the numbering of the surrounding entries $\bar{r}^e$ depends on the position of $\bar{r}_i^g$ within the sequence as shown in Figure 4.3.

Fields of Applications In addition to the approximation of discontinuous field variables, discontinuous collocation can be used to deal with *degenerated* and *non-conforming* patches. The former case is illustrated in Figure 4.4(a). There a quarter of a hemisphere is modeled by concentrating several control points, i.e. $\boldsymbol{c}_6 = \boldsymbol{c}_7 = \boldsymbol{c}_8$. Hence, their related collocation points would coincide as well, if they are specified by the Greville abscissae. The offset α is applied to these anchors so that each one has its own location in the Cartesian system. In the example considered, this leads to the three collocation points around the degenerated edge.

Regarding multi-patch geometries, collocation points $\boldsymbol{x}^c$ of adjacent patches may coincide if they are located at their common edge. In addition, the parametric coordinates of those $\boldsymbol{x}^c$ must be known within both parameter spaces in order to regularize the singular integrals. However, collocation points at common edges are avoided if discontinuous collocation is used there. Consequently, each patch can be treated separately. Figure 4.4(b)

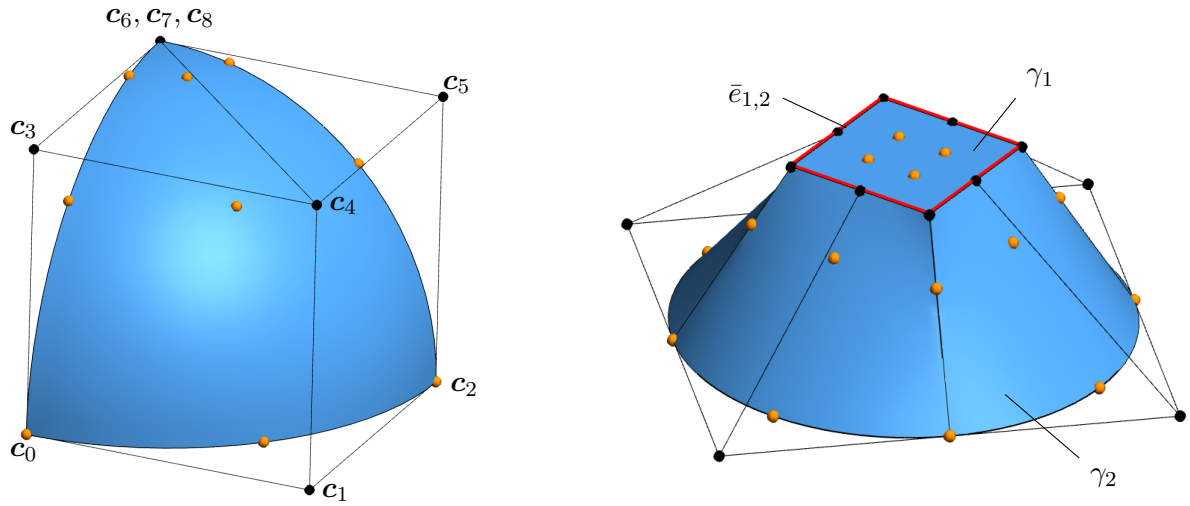

(a) Degenerated Patch (b) Non-conforming Patches

Figure 4.4: Discontinuous collocation applied to different geometrical cases. Control points are indicated by black dots, whereas orange dots are used for collocation points. In (b), the common edge $\bar{e}_{1,2}$ of the patches γ_1 and γ_2 is highlighted in red.

shows a model which consists of two patches γ_1 and γ_2 with a common edge $\bar{e}_{1,2}$. Since the former is a linear and the latter a quadratic surface, it is evident that γ_1 and γ_2 have non-conforming parameter spaces. On the one hand, $\bar{e}_{1,2}$ is represented by 4 linear curves since γ_1 is a simple square based on linear B-splines. On the other hand, it is defined by quadratic NURBS according to γ_2. Some collocation points would lie on $\bar{e}_{1,2}$, if they are specified by continuous anchors. Due to the application of discontinuous collocation they are situated around the common edge.

5 Independent Field Approximation

The following explanations will refer to elasticity problems and uses the related terminology. However, they are analogously applicable to potential problems.

In the previous chapter, numerical approximations methods based on boundary integral equations have been included into an isogeometric framework. In this chapter, the concept is generalized by representing the geometry, displacement and traction field independently from each other, which leads to the term *independent field approximation*. The obtained formulations are more flexible and avoid redundancies.

For example, the refinement of the geometry is in fact superfluous since knot insertion or degree elevation does not change a NURBS patch, neither geometrically nor parametrically [93]. The geometrical aspect is discussed in more detail at the end of this chapter. The application of independent field approximation to the isogeometric Nyström and boundary element method is examined first.

5.1 Nyström Method

5.1.1 Integration Elements

Regarding the Nyström method, the discretization of the Cauchy data is determined by the applied quadrature rule and its underlaying interpolation polynomial. Hence, there is no approximation by basis functions related to the CAGD model. Consequently, the arrangement of integration regions $\tilde{\tau}$ over a patch γ can be chosen independently of the geometry basis, i.e. $\tilde{\tau} \neq \tau$. Similar to the definition of the integration elements τ introduced in Section 4.1.1, the patch γ is subdivided into a set of elements $\tilde{\tau}$, so that

$$\gamma = \bigcup_{i=1}^{I} \tilde{\tau}_i. \tag{5.1}$$

It should be emphasized that this partition is not determined by the knots spans of the knot vector Ξ related to the geometry representation. But still, the geometry must be smooth within each $\tilde{\tau}$. In order to consider the geometrical continuity, it is proposed to define the elements $\tilde{\tau}$ by means of an *artificial* knot vector Λ such that $\Xi \subset \Lambda$. To be clear, the purpose of Λ is not to construct basis functions but to organize the global partition of $\tilde{\tau}$ properly. The knots of Λ are denoted by a_i. Based on the initial discretization, i.e. $\Xi = \Lambda$, the approximation quality of the Cauchy data can be improved by inserting additional knot values $\hat{a}_i$ into a knot span s of Λ, such that $a_s < \hat{a}_i < a_{s+1}$. This procedure defines an *h-refinement* that is performed in the parametric space and preserves the continuity requirements with respect to the geometry. Moreover, the grading described in Section 4.2.4 can also be performed within the artificial parameter space. The independent partition of elements $\tilde{\tau}$ over a curve is indicated in Figure 5.1.

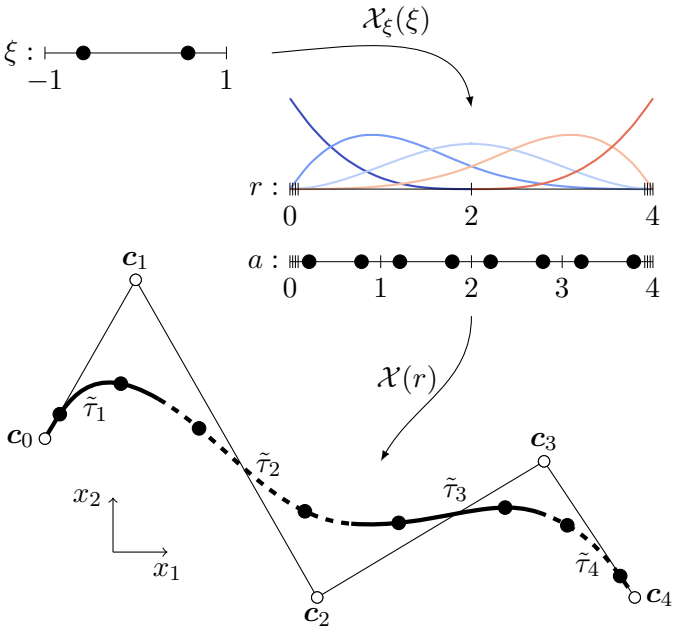

Figure 5.1: The geometry of a cubic B-spline curve is defined by control points $\boldsymbol{c}_i$ and the knot vector $\Xi = \{0, 0, 0, 0, 2, 4, 4, 4, 4\}$. The elements $\tilde{\tau}_j$ along the curve are defined by $\Lambda = \{0, 0, 0, 0, 1, 2, 3, 4, 4, 4, 4\}$ in the parameter space. Each element is equipped with a two point quadrature rule defined in the reference interval $\xi \in [-1, 1]$.

5.1.2 Local Refinement of Tensor Product Surfaces

The use of artificial knot vectors Λ is sufficient for the partition of $\tilde{\tau}$ over a curve. However, the extension of this concept to surface representations is limited. In particular, local refinement is not possible if elements $\tilde{\tau}$ are defined by a tensor product of Λ_I and Λ_J. In this section, a strategy for local refinement with the isogeometric Nyström method is derived.

The proposed procedure is visualized in Figure 5.2. Global refinement is performed by the introduction of additional artificial knots, i.e. inserting $\hat{a}_j$ in Λ_J as indicated by the dashed line in Figure 5.2(a). Both non-zero knot spans in Λ_I are subdivided. The subsequent subdivision is intended to be local for each of the elements $\tilde{\tau}$. In particular, the definition of *refinement points* $\grave{\boldsymbol{r}}$ is proposed for the partitioning of *local elements* $\grave{\tau}$ within an $\tilde{\tau}$. Each $\grave{\boldsymbol{r}}$ is defined in the parametric space and located either inside or on an edge of $\tilde{\tau}$. Inside $\tilde{\tau}$, it defines the origin of a cross which is aligned to the parametric coordinate system and subdivides $\tilde{\tau}$ into four local elements $\grave{\tau}$. If $\grave{\boldsymbol{r}}$ is located on an edge, $\tilde{\tau}$ is subdivided into two $\grave{\tau}$. Further, a local grid can be defined by combining several refinement points simultaneously. The local refinement options described are illustrated in Figure 5.2(b).

In order to enable further refinement of local elements, all elements are sorted in a *hierarchical* tree structure and labeled with the refinement level ℓ. The initial refinement level $\ell = 0$ refers to the global element, hence $\grave{\tau}^0 \equiv \tilde{\tau}$. Each node of the tree may have a

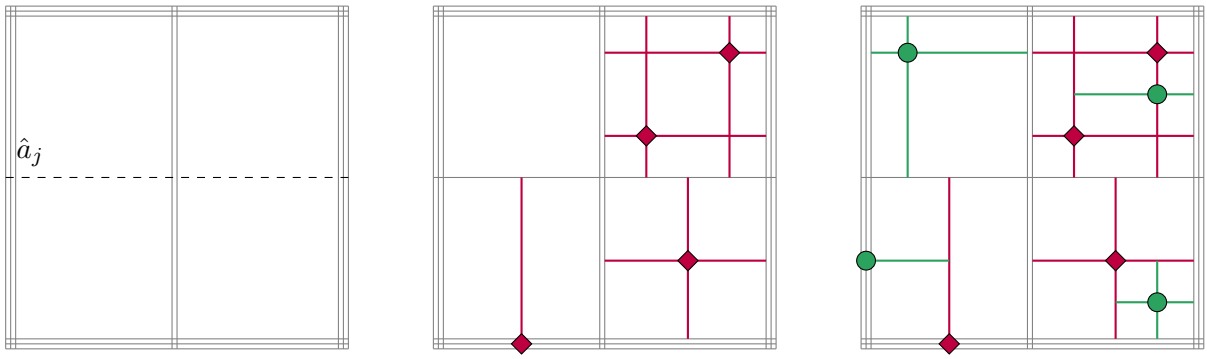

(a) Global Refinement (b) Local Refinement $\ell = 1$ (c) Local Refinement $\ell = 2$

Figure 5.2: Subsequent refinement of integration elements defined by the tensor product of $\Lambda_I = \{0, 0, 0, 1, 1, 2, 2, 2\}$ and $\Lambda_J = \{0, 0, 0, 2, 2, 2\}$. (a) Global refinement by inserting $\hat{a}_j = 1$ into Λ_J. (b) Subdivision into local elements by refinement points of the first refinement level which are denoted by diamonds. (c) Further local refinement by a higher refinement level indicated by circles.

different number I of ancestors because several refinement points may be defined per level. The local elements $\check{\tau}_i^\ell$ generated in level ℓ cover the complete area of the local element $\check{\tau}^{\ell-1}$ of the previous level

$$\check{\tau}^{\ell-1} = \bigcup_i^I \check{\tau}_i^\ell. \tag{5.2}$$

The final partition of the global element $\tilde{\tau}$ is defined by the sum of local elements

$$\tilde{\tau} = \bigcup_{j=1}^J \check{\tau}_j \tag{5.3}$$

related to the *leaves* in the hierarchical tree structure as shown in Figure 5.3. An example of such a locally refined patch with two levels of refinement is depicted in Figure 5.2(c). The local refinement procedure involves the scaling and translation of the element boundaries. Details on the construction of this transformation due to a given set of $\check{\boldsymbol{r}}$ are provided in Appendix B. Finally, local refinement of a patch is illustrated in Figure 5.4.

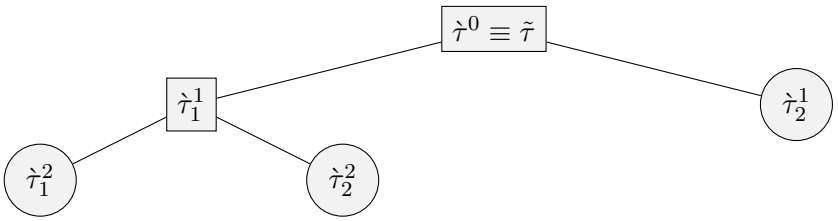

Figure 5.3: Hierarchical tree structure of local elements $\check{\tau}$ with different levels of refinement. The final partition is defined by the leaves indicated by circles.

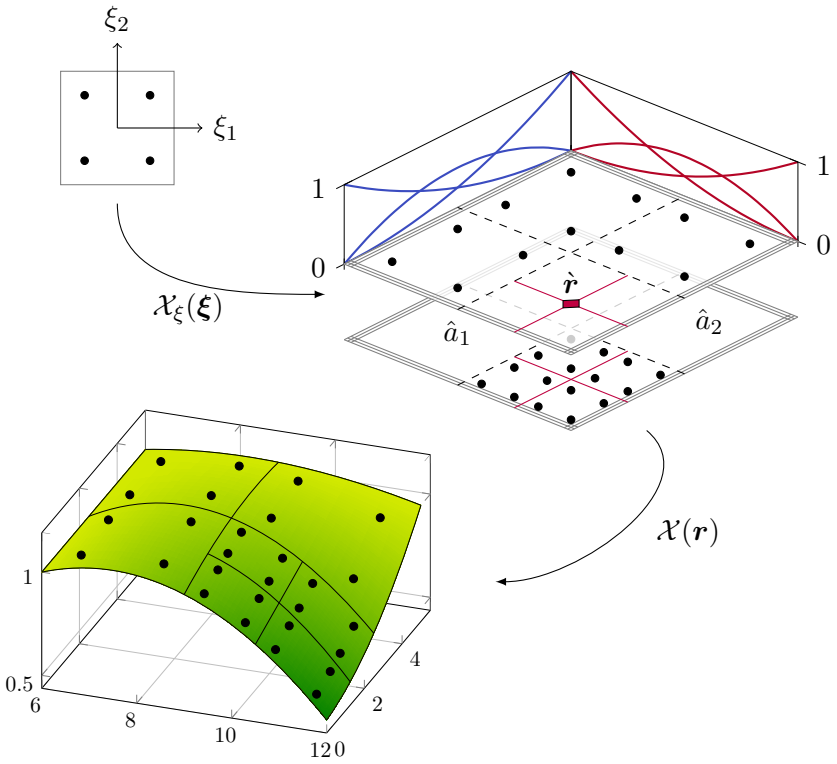

Figure 5.4: The distribution of quadrature points on a locally refined surface. The basis function of the geometry are defined by $\Xi_I = \Xi_J = \{0, 0, 0, 2, 2, 2\}$. The partition of local elements is defined by a global insertion of $\hat{a}_1 = \hat{a}_2 = 1$ and a refinement point $\hat{\boldsymbol{r}} = (0.5, 0.5)^\intercal$.

5.2 Boundary Element Method

In the context of isogeometric BEM, the Cauchy data are discretized by means of B-splines or NURBS. The related mappings have been presented in Section 4.3.1 and are denoted by $\mathcal{Y}_u(\boldsymbol{r})$ and $\mathcal{Y}_t(\boldsymbol{r})$ for displacements $\mathbf{u}$ and traction $\mathbf{t}$, respectively. In the following, *isoparametric* and *subparametric* patches are introduced. The former employs the isoparametric paradigm, i.e. all field are represented by the same basis functions, as it is generally established in isogeometric analysis. The latter utilizes the proposed independent field approximation. The term subparametric is used to indicate that less parameters are used for the description of the geometry than for the Cauchy data.

5.2.1 Isoparametric Patches

In an isoparametric discretization, the mappings $\mathcal{Y}_u(\boldsymbol{r})$ and $\mathcal{Y}_t(\boldsymbol{r})$ are equal to the geometrical one $\mathcal{X}(\boldsymbol{r})$. This implies some compromises. First of all, the same refinement is applied to all fields. Refinement of the unknown field is mandatory to improve the solution. But as a consequence, the geometry and the known field are refined even though they may be exactly represented by the initial basis functions. In addition to refinement aspects, the fields have different continuity requirements along corners and edges. In particular,

discontinuous basis functions are required to describe traction jumps. On the other hand, they are not optimal for representing the displacement field which should be continuous according to the physical constraint. Furthermore, the number of basis functions is rising unnecessarily.

Thus, a preliminary conclusion is that isoparametric discretization introduces superfluous control variables. This increases the numerical effort and storage requirements for setting up the discrete boundary integral operators of the right hand side block matrices of the system of equations (4.31). Moreover, refinement of CAGD models affects the efficiency of all geometry evaluations performed during the analysis. These points motivate the application of the proposed subparametric approach presented next.

5.2.2 Subparametric Patches

In this section, subparametric patches are introduced. The key idea is to treat each field separately in order to fulfill their individual needs. In particular, the concept of a subparametric element is adopted, i.e. more basis functions will be used to represent the field variables than for the geometry representation.

The basis functions of the geometry θ, the displacements φ and the tractions ψ are defined by the knot vector Ξ_θ, Ξ_φ and Ξ_ψ, respectively. Without loss of generality, basis functions of the Cauchy data are defined as an extended version of Ξ_θ, so that

$$\Xi_\theta \subset \Xi_\varphi \qquad \text{and} \qquad \Xi_\theta \subset \Xi_\psi. \tag{5.4}$$

This definition guarantees a proper partition of integration elements. It should, however, be noted that it allows the variation of basis functions types. For instance, the Cauchy data over a NURBS patch may be approximated by B-splines. First of all, the evaluation of B-splines is faster and furthermore there is no need to compute new weight values during the refinement process. The approximation quality of such an approach is investigated in Section 7.1.1. The subsequent sections are dedicated to the general refinement strategy and the setting up of the block system of matrices (4.31).

5.2.2.1 Individual Refinement

In the present implementation the geometry knot vector Ξ_θ provides the initial basis for all fields. Subsequently, basis functions are refined if an only if it is necessary. Discontinuous basis functions are introduced for the traction field solely. The known Cauchy data are classified as *simple* or *complex* boundary conditions as indicated in Figure 5.5. The former can be exactly represented by Ξ_θ, hence the corresponding discretization does not need to be refined. Homogeneous boundary conditions or constant loading are examples for such boundary conditions. The latter can only be approximated and the corresponding basis functions have to be refined in order to improve the representation of the known Cauchy data. In such a case, refinement is performed equal to the one for the approximation of the unknown field.

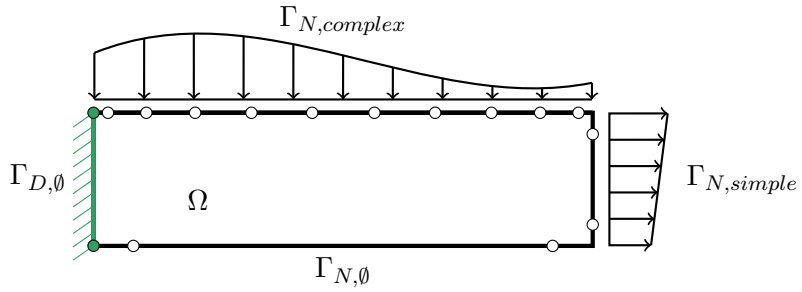

Figure 5.5: Examples of simple and complex boundary conditions applied to a cantilever beam. Homogeneous boundary condition are denoted by the subscript $\emptyset$. Circles indicate the related anchors of the basis functions.

5.2.2.2 Collocation

In isogeometric BEM, collocation points are defined by the anchors of basis functions. Subparametric patches contain different discretizations for each field, consequently, there are various sets of anchors as indicated in Figure 5.6. In order to obtain collocation points, they are specified to be the anchors of the basis functions approximating the unknown field.

This results in a *mixed collocation* scheme where discontinuous collocation is applied at Γ_D and continuous collocation is applied at Γ_N. As a result, continuous displacements and discontinuous tractions can be discretized simultaneously at non-smooth boundaries. Different arrangements of collocation points at corners are illustrated in Figure 5.7. In the mixed case 5.7(b), the displacement anchor at the corner does not induce a collocation point $\boldsymbol{x}^c$, since the displacement is known there, i.e. $\boldsymbol{x} \in \Gamma_D$.

The application of subparametric patches leads to a block system of matrices (4.31) similar to the isoparametric approach. In fact, the left hand side $\mathbf{L}$ is equivalent, but the right hand side $\mathbf{R}$ varies. The size of the isoparametric one $\mathbf{R}_i \in \mathbb{R}^{n \times n}$ is determined by the degrees of freedom n. However, the number of columns m of the subparametric right hand side matrix $\mathbf{R}_s \in \mathbb{R}^{n \times m}$ is determined by the control parameters which represent the known field. Usually, this number is significantly smaller than the degrees of freedom, i.e. $m \ll n$.

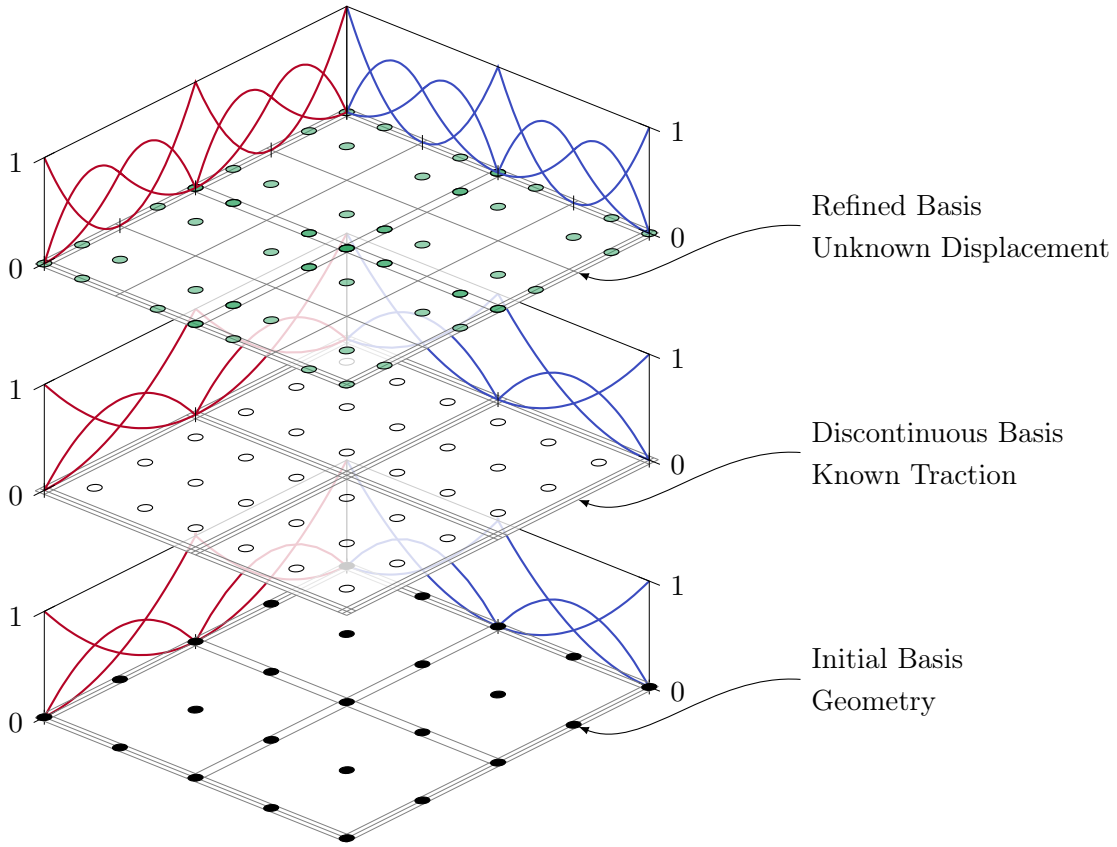

Figure 5.6: Anchors of different fields of a patch which is subjected to simple Neumann boundary conditions. The anchors are indicated by different circles for each field.

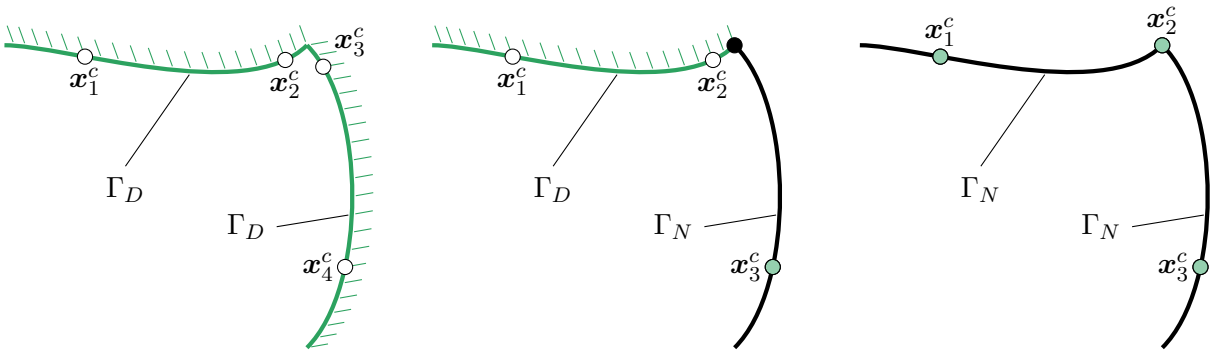

(a) Discontinuous (b) Mixed (c) Continuous

Figure 5.7: Collocation situations of subparametric patches at corners: (a) discontinuous collocation for unknown tractions, (c) continuous collocation for unknown displacements and (b) mixed collocation at the join of Γ_D and Γ_N. White circles indicate collocation points defined by traction anchors, whereas collocation point of displacement anchors are green. In (b), the black circle denotes a displacement anchor which is not used as collocation point.

5.3 Geometry Evaluation

Independently from the applied numerical approximation method, the refinement of the geometry basis functions is superfluous due to the fact that it does not improve the representation of the computational domain. Nevertheless, changing the geometrical basis has an influence on the computational effort for the evaluation of geometrical mapping $\mathcal{X}(\boldsymbol{r})$ and the related Jacobi-matrix $\mathbf{J}_{\mathcal{X}}(\boldsymbol{r})$. In particular, the effort depends on the degree p of the underlaying basis.

Table 5.1 provides the number of elementary operations, i.e. floating point operations such as division and multiplication, which are required for evaluations of B-spline and NURBS patches. The values are obtained by the analysis of the efficient algorithms proposed in [93]. A detailed determination of these factors is given in [83]. In general, it is demonstrated that geometry evaluations have quadratic complexity, i.e. $\mathsf{Op}(p) = \mathcal{O}(p^2)$, with respect to the degree p. So it can be concluded that each superfluous degree elevation of the geometry reduces the efficiency of the analysis.

	curves		surface with $p = p_1 = p_2$	
	$\mathcal{X}(r)$	$\mathbf{J}_{\mathcal{X}}(r)$	$\mathcal{X}(\boldsymbol{r})$	$\mathbf{J}_{\mathcal{X}}(\boldsymbol{r})$
B-spline	$(3p^2 + 5p + 2)/2$	$(3p^2 + 3p + 6)/2$	$5p^2 + 7p + 2$	$7p^2 + 13p + 6$
NURBS	$(3p^2 + 9p + 6)/2$	$(3p^2 + 15p + 14)/2$	$7p^2 + 11p + 4$	$14p^2 + 27p + 15$

Table 5.1: Elementary operations required for the evaluation of CAGD geometries.

5.3.1 Assessment of Computational Effort

The influence of geometry evaluations on the integration time is examined. To be precise, the effort for an isogeometric BEM analysis is investigated. The applied test setting is depicted in Figure 5.8. A unit square γ defines the computational domain. The related discrete single layer operator $\mathbf{V}_\gamma$ and double layer operator $\mathbf{K}_\gamma$ are computed for various source points $\tilde{\boldsymbol{x}}_r$, $\tilde{\boldsymbol{x}}_n$ and $\tilde{\boldsymbol{x}}_s$. These points are chosen so that regular, nearly singular and singular boundary integrals occur. Hence, different integration schemes are applied as

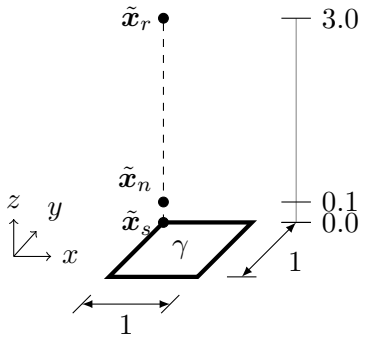

Figure 5.8: Unit square γ and source points $\tilde{\boldsymbol{x}}$ of the single patch integration test.

described in Section 4.3.3. Moreover, the accuracy of the numerical integration is ensured up to a user-defined quadrature tolerance ϵ_Q due to an adaptive numerical integration scheme presented in [82]. For the following test cases, it is set to $\epsilon_Q = 10^{-9}$. Degree elevation is applied to improve the discretization. For the sake of clarity the polynomial degree of the geometry representations is denoted by p_g, whereas p_c is taken for the degree of the basis functions related to Cauchy data. The patch γ is labeled isoparametric, if Cauchy data and geometry are described by the same NURBS basis functions, i.e. $p_c = p_g$. In contrast to the subparametric discretization where only the basis of the Cauchy data is degree elevated. Table 5.2 shows the number of Gauss points required for the subparametric test cases. It indicates that accurate integration in the context of BEM demands a large number of quadrature points and therefore, many geometry evaluations.

	$\#GP$ for $\mathbf{V}_\gamma$			$\#GP$ for $\mathbf{K}_\gamma$		
p_c	regular	near. sing.	singular	regular	near. sing	singular
1	64	375	1447	64	415	1015
2	64	375	1575	100	415	1015
3	100	375	1711	100	415	1015
4	100	375	1903	100	479	1015
5	100	375	1967	100	479	1015
6	100	439	1967	100	511	1015

Table 5.2: Required number of Gauss points ($\#GP$) depending on degree p_c on the unit square γ which is discretized by linear basis functions, i.e. $p_g = 1$, and different integration schemes.

The numerical integration is performed single-threaded and repeated 100 times, in order to obtain comparable timings. The runtime of isoparametric and subparametric patches are denoted by t_i and t_s, respectively. Figure 5.9 illustrates the difference between the two approaches in terms of computation time. In particular, the performance is compared using the factor t_i/t_s. It is demonstrated that the proposed subparametric concept increases the efficiency of the computation of the matrix entries. The graphs of the different integration schemes are almost similar. Hence, the obtained runtime ratios are independent of the actual number of required integration points. It seems that a speedup of approximately 12 % for $\mathbf{V}_\gamma$ and 17 % for $\mathbf{K}_\gamma$ is achieved for each degree elevation applied. The difference between the two operators occurs because the latter requires an additional evaluation of the outward normal $\mathbf{n}$.

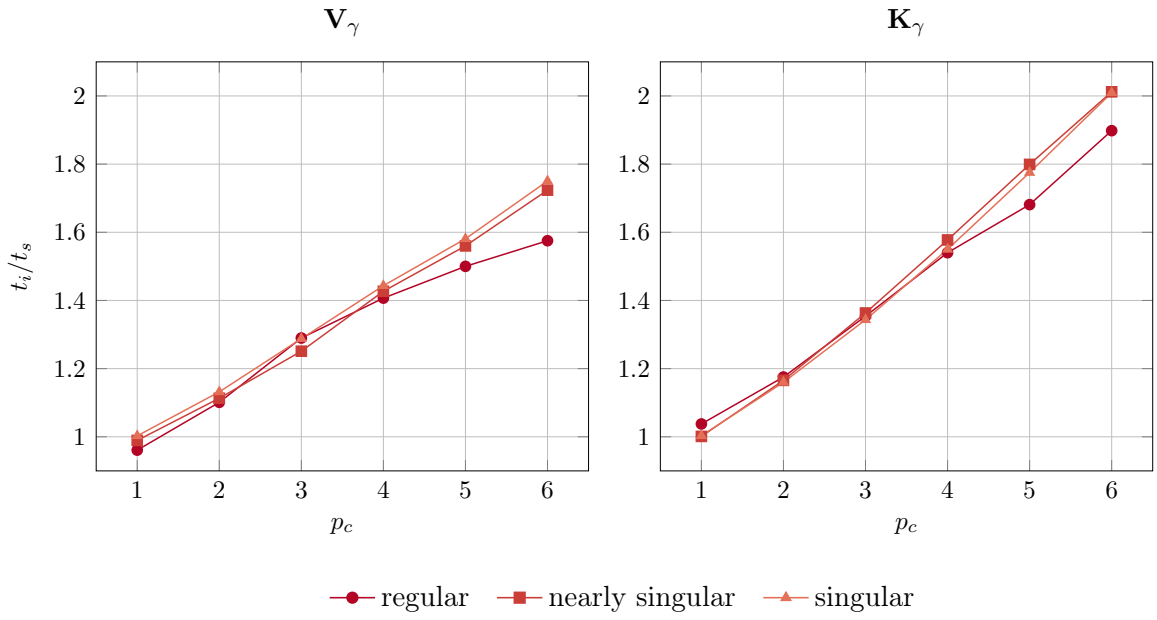

Figure 5.9: Integration time of the unit square example for an isoparametric BEM discretization (t_i) related to a subparametric one (t_s) as a function of the degree p_c of the Cauchy data. The discrete single layer $\mathbf{V}_\gamma$ and double layer $\mathbf{K}_\gamma$ operators are computed using regular, nearly singular and singular integration.

6 Analysis of Trimmed Geometries

Trimmed patches are very often a part of CAGD models because they offer a convenient way to apply an efficient surface representation to non-rectangular surface topologies. However, their application to an analysis needs further consideration. First of all, trimming procedures are used to define visible domains Ω_p over patches independently of the underlying knot sequence, i.e. the original control points still remain. Hence, it is not sufficient to define integration elements based on the non-zero knot spans. Moreover, the trimmed basis contains *degenerated* basis functions which exist only partially within Ω_p. In some cases their supports may be very small and the condition number of the resulting system matrices can become large. Consequently, a trimmed basis is not guaranteed to be stable.

In the following, a method is presented that re-establishes the stability of a trimmed B-spline basis. Originally, it has been developed in the context of weighted extended B-splines [63, 64, 99]. The term weighted indicates that their definition includes a weighting function which is used to define the boundary of Ω_p and to enforce essential boundary conditions to a finite element analysis. In the context of BEM, the weighting function is not required, thus the term *extended B-splines* is used. The application of such B-splines to NURBS geometries is straightforward because of the independent field approximation.

6.1 Definition of Extended B-splines

The concept of extended B-splines $B^e_{i,p}$ is illustrated in Figure 6.1. The original basis 6.1(a) is defined by the knot vector $\Xi = \{0, 0, 0, 1, 2, 3, 3, 3\}$. The domain of the trimmed patch Ω_p is determined by a trimming parameter t, i.e. $\Omega_p \in (t, 3)$, as indicated by the dashed vertical line. In the initial step, the stable B-splines $B_{i,p}$ and degenerated B-splines $B_{j,p}$ of the basis have to be identified. Therefore the size of the supports inside Ω_p may be evaluated [63]. Here a different approach is proposed: B-splines are labeled degenerated if their support is partially within, but the corresponding anchor is outside of the visible domain. The related indices are stored in the index-set $\mathbb{J}$. In the given example this is the case for B_0. Next, the polynomial segments of the trimmed knot span are substituted by *extensions* of the polynomial segments $\mathcal{B}^s_i$ of the closest non-trimmed knot interval s. Finally, those extensions are defined by a linear combination of the original ones of the trimmed knot span

$$B^e_{i,p} = B_{i,p} + \sum_{j \in \mathbb{J}_i} e_{i,j} B_{j,p} \tag{6.1}$$

where $\mathbb{J}_i$ is an index-set of all degenerated B-splines related to the current $B^e_{i,p}$. Note that equation (6.1) defines $B^e_{i,p}$ outside of the trimmed knot span, where $B^e_{i,p} = B_{i,p}$, as well. It remains to define the extrapolation weights $e_{i,j}$.

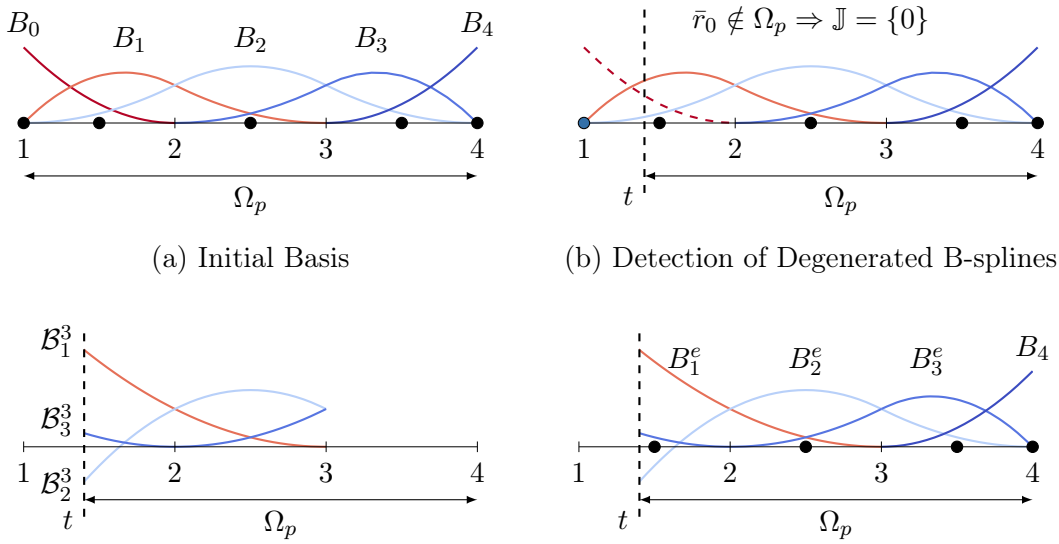

(a) Initial Basis

(b) Detection of Degenerated B-splines

(c) Extensions of Polynomial Segments

(d) Extended B-splines

Figure 6.1: Basic procedure to get from (a) conventional to (d) extended B-splines: (b) determination of degenerated B-splines and substitution of trimmed polynomial segments by (c) extensions of non-trimmed ones.

6.1.1 Univariate Extrapolation Weights

In order to compute the extrapolation weights $e_{i,j}$ of an extended B-spline an interpolation problem needs to be solved. In particular, the extended polynomial segments $\mathcal{B}_i^s$ of the non-trimmed knot span s shall be approximated by B-splines of the trimmed knot span t such that

$$\mathcal{B}_i^s(r) = \sum_{j=t-p}^{t} B_{j,p}(r)\, e_{i,j}, \qquad r \in [r_t, r_{t+1})\,. \tag{6.2}$$

It should be noted that $\mathcal{B}_i^s$ can be exactly represented by $B_{j,p}$ since they are polynomials within the B-spline space $\mathbb{S}_{p,\Xi}$. Moreover, the coefficient $e_{i,i}$ has to be equal to 1 due to the fact that $\mathcal{B}_i^s(r) \equiv B_{i,p}(r), r \in [r_s, r_{s+1})$. Analogously, $e_{i,k} = 0$ for other non-zero B-splines $B_{k,p}$ of the knot span s, since $\mathcal{B}_i^s(r) \neq B_{k,p}(r), r \in [r_s, r_{s+1})$. Other values are obtained, only if the basis function is degenerated, i.e. $j \in \mathbb{J}_i$. However, spline interpolation requires $p+1$ anchors $\bar{r}$ as described in Section 2.5. Unfortunately, the recommended $\bar{r}$, i.e. Greville or Demko abscissae, are not within the trimmed knot span t in general. Hence, a *quasi interpolation* approach is preferred.

Quasi interpolation methods allow the computation of spline approximations without solving an linear system of equations. In addition, the schemes are applied to single intervals, hence they are ideally suited to compute the extrapolation weights $e_{i,j}$. Here the so-called *de Boor–Fix* or dual functional $\lambda_{j,p}$ [16] is used: for any piecewise polynomial

$f \in \mathbb{S}_{p,\Xi}$,

$$f = \sum_{j=0}^{J-1} \lambda_{j,p}(f)\, B_{j,p} \tag{6.3}$$

with

$$\lambda_{j,p}(f) = \frac{1}{p!} \sum_{k=0}^{p} (-1)^k \psi_{j,p}^{(p-k)}(\mu_j)\, f^{(k)}(\mu_j), \qquad \mu_j \in [r_j, r_{j+p+1}] \tag{6.4}$$

$$\psi_{j,p}(r) = \prod_{l=1}^{p} (r - r_{j+l})\,. \tag{6.5}$$

Note that the evaluation point μ_j can be chosen arbitrarily within $[r_j, r_{j+p+1}]$. Moreover, it can be proven that for all l,

$$\lambda_{l,p}(B_{j,p}) = \delta_{lj} \qquad \text{and} \qquad \lambda_{l,p}\left(\sum_{j=0}^{J-1} B_{j,p}\, c_j\right) = c_l\,. \tag{6.6}$$

In order to compute $e_{i,j}$ the function f is substituted by $\mathcal{B}_i^s$, leading to

$$e_{i,j} = \lambda_{j,p}(\mathcal{B}_i^s) = \frac{1}{p!} \sum_{k=0}^{p} (-1)^k \psi_{j,p}^{(p-k)}(\mu_j)\, \mathcal{B}_i^{s\,(k)}(\mu_j), \qquad \mu_j \in [r_j, r_{j+p+1}]\,. \tag{6.7}$$

Equation (6.7) provides in fact the entire information to set up the extrapolation weights. However, it may seems a bit complex at first glance. So its evaluation is discussed in more detail. The polynomial $\psi_{j,p}$ can be rewritten in an explicit representation also known as power basis form

$$\psi_{j,p}(r) = \sum_{k=0}^{p} \beta_k\, r^k. \tag{6.8}$$

The corresponding coefficients β_k are computed by

$$\beta_k = (-1)^k \sum_{l=1}^{L} \prod_{m \in \mathbb{T}_{k,l}} r_m \qquad \text{with} \qquad L = \frac{p!}{(p-k)!\, k!} \tag{6.9}$$

where the sum over $\mathbb{T}_{k,l}$ denotes all k-combinations with repetition of the knots appearing in the definition of $\psi_{j,p}$, i.e. $r_{j+1}, \ldots, r_{j+p}$. The segments $\mathcal{B}_i^s$ of $B_{i,p}$ can also be converted to an explicit representation by Taylor expansion given by

$$\mathcal{B}_i^s(r) = \sum_{k=0}^{p} \frac{B_{i,p}^{(k)}(\tilde{r})}{k!}\, (r - \tilde{r})^k = \sum_{k=0}^{p} \alpha_k\, (r - \tilde{r})^k, \qquad \tilde{r} \in [r_s, r_{s+1}) \tag{6.10}$$

where the point $\tilde{r}$ is within the corresponding knot span s. Equation (6.10) can also be

written in power basis form such that

$$\mathcal{B}_i^s(r) = \sum_{k=0}^{p} \tilde{\alpha}_k \, r^k \qquad \text{with} \qquad \tilde{\alpha}_k = \sum_{m=k}^{p} \binom{m}{k} \alpha_m \, (-\tilde{r})^{m-k} \tag{6.11}$$

where $\binom{m}{k}$ denotes the binomial coefficient defined as

$$\binom{m}{k} \coloneqq \frac{m!}{(m-k)!\, k!} \, . \tag{6.12}$$

Based on the explicit representations (6.8) and (6.11), the functional can be evaluated without direct evaluation at a point μ_j. Since this point can be chosen arbitrarily, values depending on μ_j cancel out [98]. Therefore, the dual functional can be written as

$$e_{i,j} = \lambda_{j,p}(\mathcal{B}_i^s) = \frac{1}{p!} \sum_{k=0}^{p} (-1)^k \, (p-k)! \, \beta_{p-k} \, k! \, \tilde{\alpha}_k. \tag{6.13}$$

Supplementary information regarding the evaluation of $\lambda_{j,p}(\mathcal{B}_i^s)$ is provided in Appendix C.

6.1.2 Bivariate Extrapolation Weights

Bivariate extrapolation weights $e_{i,j}$ are obtained by the tensor product of their univariate counterparts calculated for each parametric direction. The indices i and j indicate stable and degenerated bivariate B-splines, respectively. The construction procedure is visualized in Figure 6.2 and examples of different bivariate extended B-splines are shown in Figure 6.3. In general, a degenerated B-spline is distributed to $(p_1 + 1)\,(p_2 + 1)$ interior B-splines. Several degenerated B-splines $B_{j,p}$ may be associated to an interior B-spline $B_{i,p}$. In particular, the number of $B_{j,p}$ related to $B_{i,p}$ is determined by the cardinality of the corresponding intex-set $\#\mathbb{J}_i$. However, the extension procedure is restricted to those basis functions which are close to the trimming curve. For instance, the basis function shown in Figure 6.3(a) is a conventional B-spline since it is far enough away from the trimming curve.

The extrapolation weights may be negative, hence extended B-splines may have negative values as well. Nevertheless, the resulting extended B-splines inherit all essential properties of conventional B-splines including linear independence [63]. In addition, the determination of proper anchors is straightforward since all anchors of extended B-splines are within Ω_p by construction. This is an essential feature for interpolation and collocation schemes.

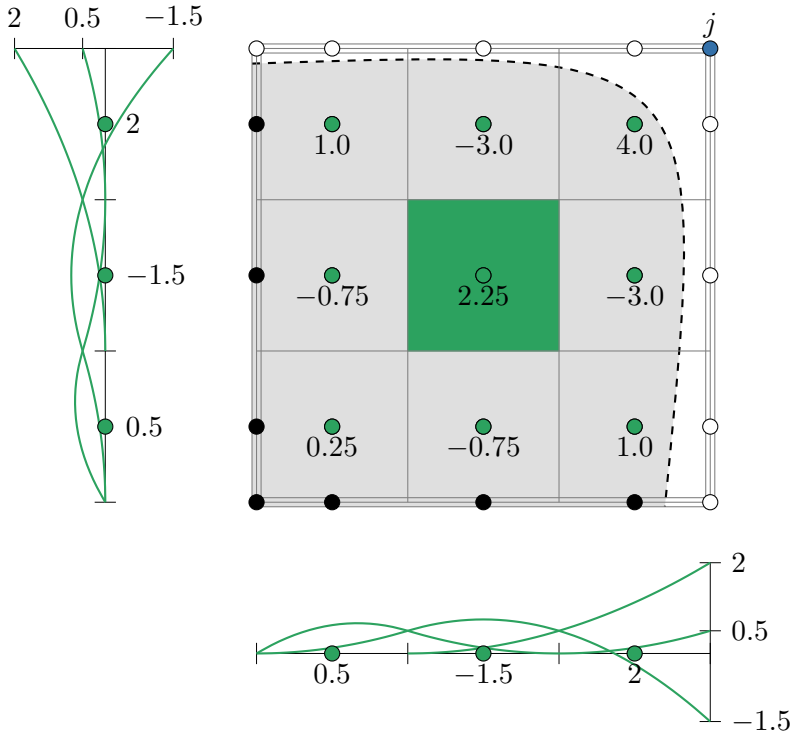

Figure 6.2: The construction of bivariate extrapolation weights $e_{i,j}$. The basis is defined by a tensor product of the B-spline depicted in Figure 6.1(a), the dashed line indicates the trimming curve and Ω_p is highlighted in gray. Stable B-splines are marked by black and green circles. The shown values of $e_{i,j}$ are related to the degenerated basis function marked by the blue circle in the upper right corner of the parameter space. The B-splines of the closest non-trimmed knot span are indicated by green circles. The values of the univariate extrapolation weights are derived in Appendix C.

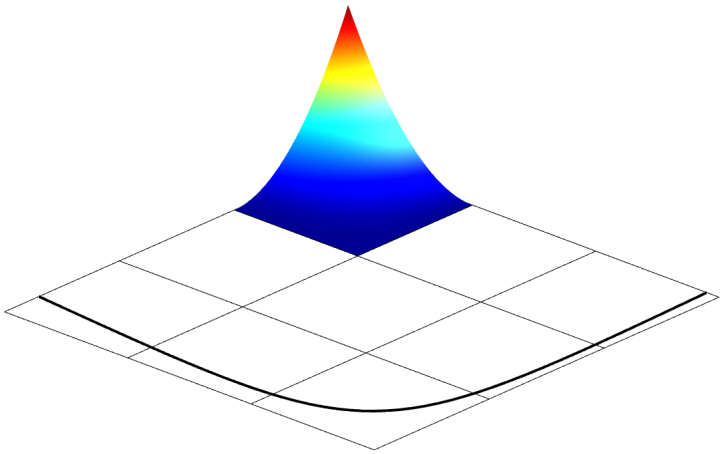

(a) $\#\mathbb{J}_i = 0$

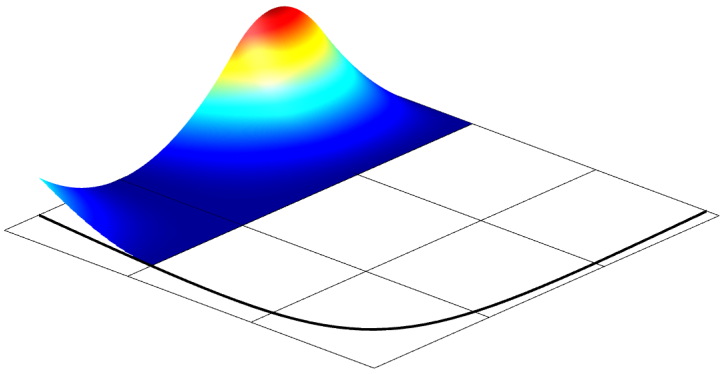

(b) $\#\mathbb{J}_i = 1$

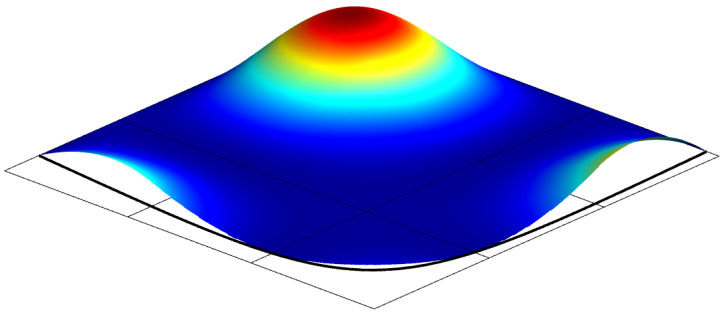

(c) $\#\mathbb{J}_i > 1$

Figure 6.3: Bivariate extended B-splines $B^e_{i,p}$ with various cardinalities of the index-set $\mathbb{J}_i$ which indicates the number of related degenerated B-splines. Note that (a) is in fact a conventional B-spline, i.e. $B^e_{i,p} \equiv B_{i,p}$, since $\mathbb{J}_i$ is empty.

6.1.3 Assessment of Approximation Quality

In order to verify the approximation quality of extended B-splines the following test case is studied: the initial B-spline basis defined by $\Xi = \{-1, -1, 1, 1\}$ is refined by degree elevated up to different degrees $p = \{2, 3, 4\}$ and uniform knot insertion. The knot insertion depth d_k indicates how often the knot spans have been subsequently subdivided. Hence, it defines how many knots are inserted. A trimming parameter $t < 1$ determines the valid domain of the patch $\Omega_p \in (-1, t)$.

An interpolation problem is solved using extended B-splines for each trimmed basis. In addition a simple approach is applied, where the anchors of degenerated basis functions are just shifted into Ω_p. If a support is entirely outside of the domain it does not contribute to the approximation in both cases. The schemes are depicted in Figure 6.4. The quality and stability of the approximation $f_h(u)$ are specified by the relative interpolation error measured in the L_2-norm $\|\epsilon_{rel}\|_{L_2}$ as well as the condition number of the spline collocation matrix $\kappa(\mathbf{A}_r)$.

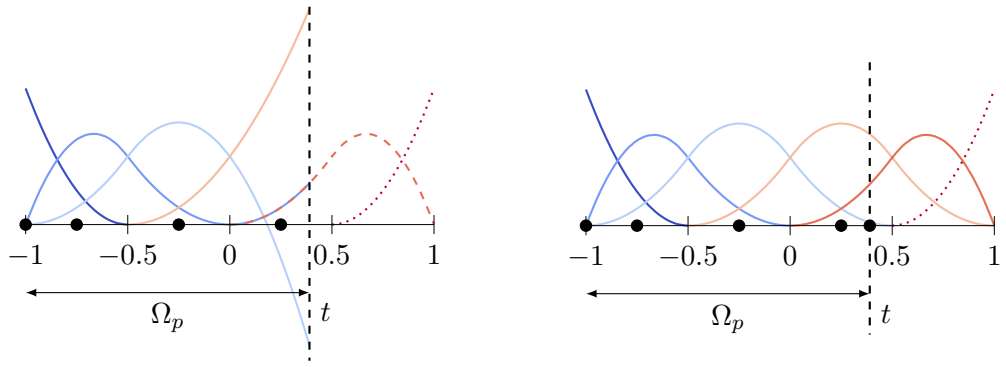

(a) Extended B-splines (b) Shifted Anchors

Figure 6.4: Trimmed univariate basis specified by $p = 2, d_k = 2$ and $t = 0.4$ for (a) extended B-splines and (b) the simple approach. The involved basis functions are indicated by continuous lines and their anchors are marked by circles. Dotted basis functions do not contribute to the interpolation problem. In (a), the dashed line indicates a degenerated B-spline.

6.1.3.1 Spline Interpolation in 1D

The target function of the interpolation problem is given by

$$f(r) = \frac{1}{|a - r|} \qquad \text{with} \qquad a = -1.1 \notin \Omega_p \qquad \text{and} \qquad r \in \Omega_p. \tag{6.14}$$

The knot insertion depth d_k is set to 4 and the interpolation is performed for several trimming parameters $t \in [0.5, 1)$. The resulting $\kappa(\mathbf{A}_r)$ and $\|\epsilon_{rel}\|_{L_2}$ of the untrimmed case, i.e. $t = 1$, are given in Table 6.1 for reference purpose. All other results are summarized in Figure 6.5 and Figure 6.6.

p	κ	$\|\epsilon_{rel}\|_{L_2}$
2	2.500	1.989×10^{-2}
3	4.310	5.734×10^{-3}
4	7.938	1.750×10^{-3}

Table 6.1: Results of the interpolation problem of the untrimmed basis, i.e. $t = 1$.

It can be observed that the condition number of $\mathbf{A}_r$ due to shifted anchors is considerably influenced by t. A peak is reached as soon as t approaches an anchor or a knot value. If extended B-splines are used, $\kappa(\mathbf{A}_r)$ hardly changes. In other words, the extended B-spline basis is stable. At the same time, the relative error is almost identical with respect to t. The extended B-spline approach yields even more accurate results, if $\|\epsilon_{rel}\|_{L_2}$ is related to the number of anchors, i.e. degrees of freedom n.

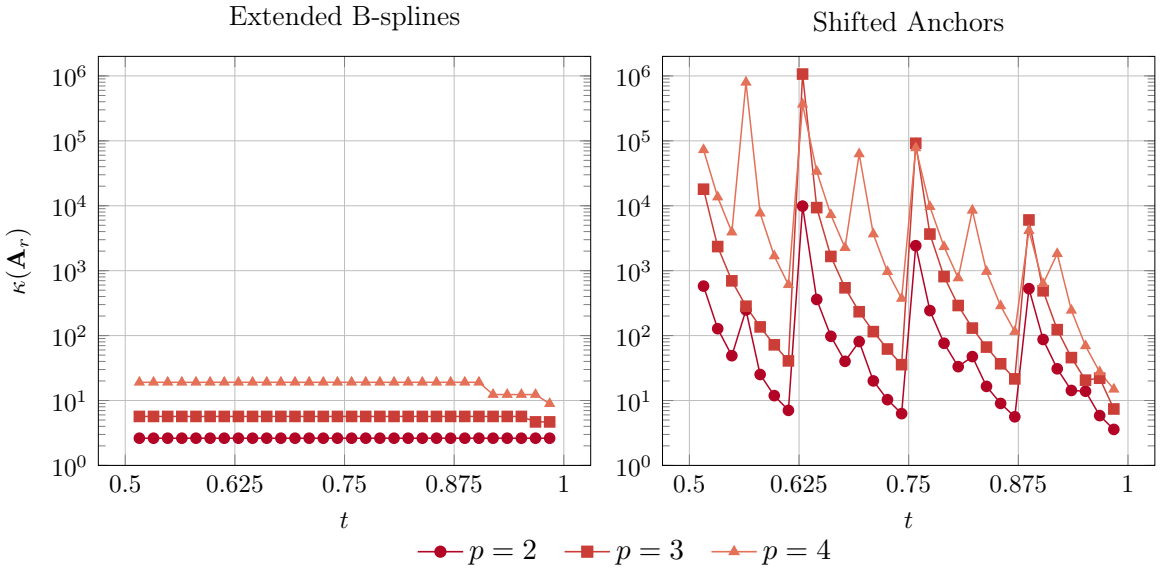

Figure 6.5: Condition number $\kappa(\mathbf{A}_r)$ for several degrees p and trimming parameters t. The labels of the horizontal axis indicate knots of the trimmed basis.

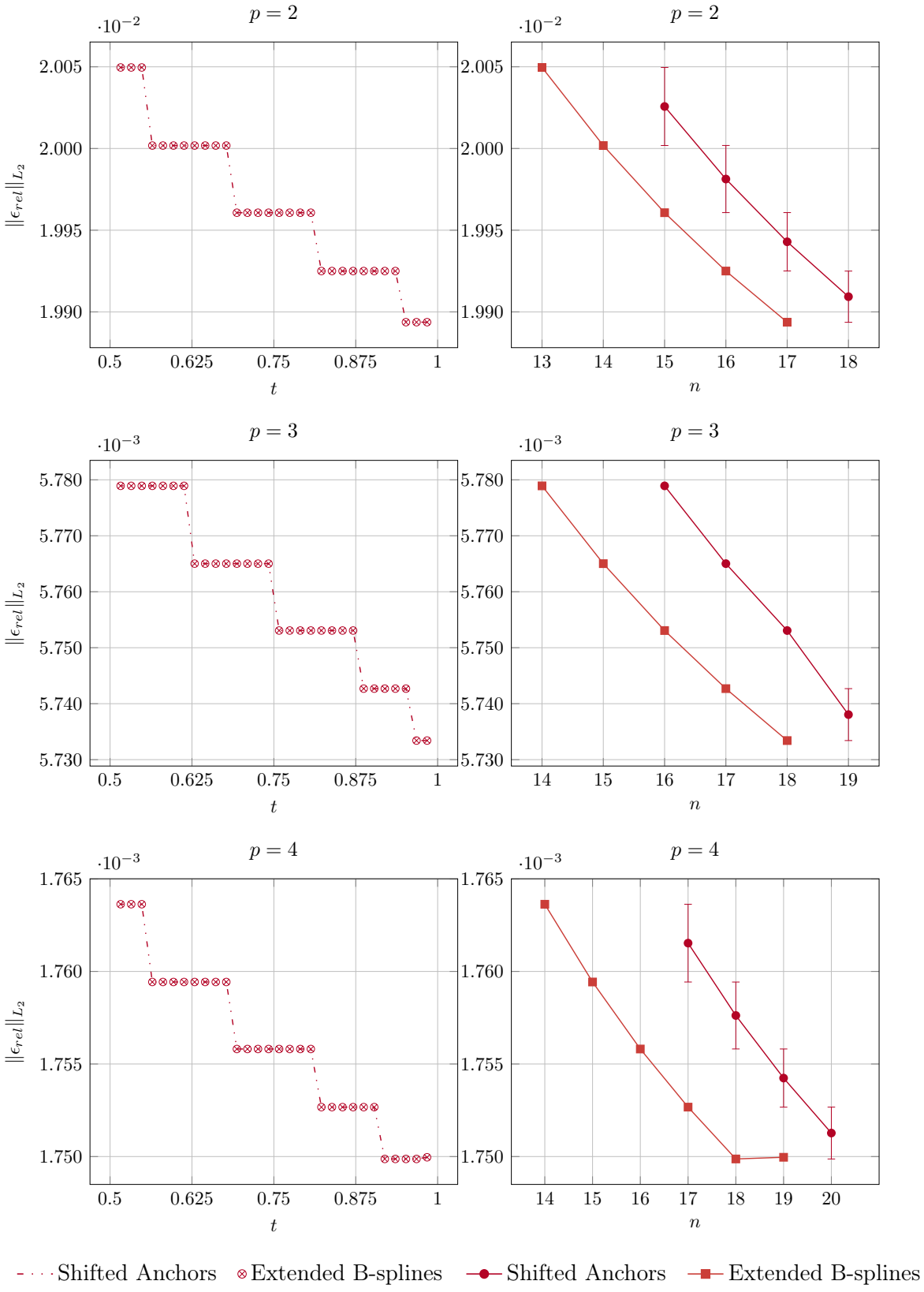

Figure 6.6: Relative interpolation error of the univariate example with several degrees p related to the trimming parameter t (left) and the degrees of freedom n (right).

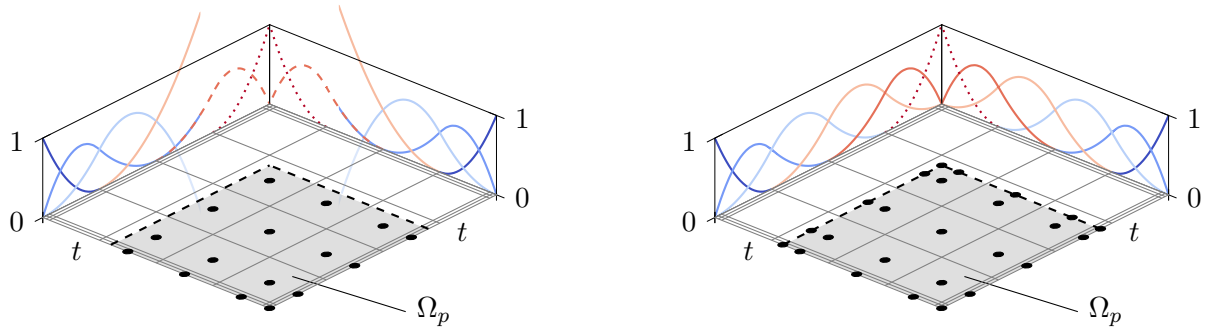

(a) Extended B-splines (b) Shifted Anchors

Figure 6.7: Trimmed bivariate basis specified by $p = 2, d_k = 2$ and $t = 0.4$ for (a) extended B-splines and (b) the simple approach. The domain Ω_p of the interpolation problem is highlighted in gray and circles indicate the basis functions involved. Note that there are anchors on the trimming curve in case of the simple approach.

6.1.3.2 Spline Interpolation in 2D

The interpolation problem of the two dimensional case is set up as tensor product of the one dimensional example as indicated in Figure 6.7. In particular, the basis and the definition of Ω_p are given by a tensor product of the univariate versions discussed in the previous section. The target function of the interpolation problem is given by

$$f(r_1, r_2) = \frac{1}{\sqrt{(a_1 - r_1)^2 + (a_2 - r_2)^2}} \qquad \text{with} \qquad a_1 = a_2 = -1.2\,. \tag{6.15}$$

The knot insertion depth d_k is set to 4 for both intrinsic directions and the interpolation problem is performed for several trimming parameters $t \in [0.5, 1)$. For the untrimmed case, i.e. $t = 1$, the resulting $\kappa(\mathbf{A}_r)$ and $\|\epsilon_{rel}\|_{L_2}$ are summarized in Table 6.2. All other results are depicted in Figure 6.8 and Figure 6.9.

It is evident that the simple approach negatively affects the condition number and subsequently the quality of the approximation. The error peaks near knot values are in fact disastrous. Astonishingly, extended B-splines provide a stable basis where $\kappa(\mathbf{A}_r)$ barely changes for the same trimming cases. The reduction of the approximation accuracy occurs due to the reduction of the degrees of freedom n, i.e. number of extended B-spline, as the trimming parameter $t \to 0.5$.

p	κ	$\|\epsilon_{rel}\|_{L_2}$
2	6.250	2.108×10^{-4}
3	18.574	4.488×10^{-5}
4	63.015	7.657×10^{-6}

Table 6.2: Results of the interpolation problem of the untrimmed bivariate basis.

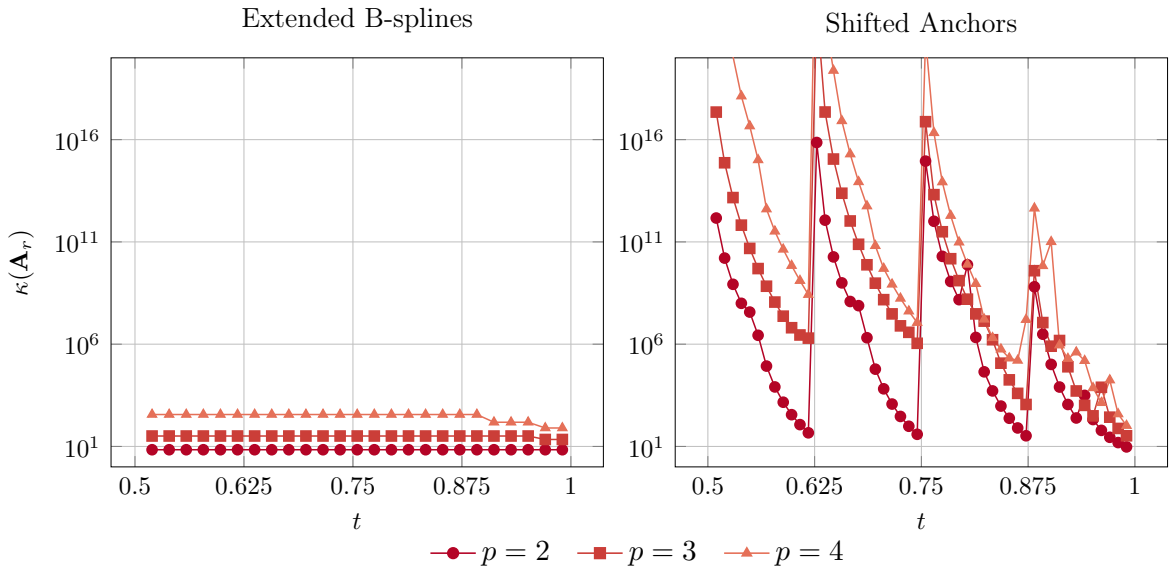

Figure 6.8: Condition number $\kappa(\mathbf{A}_r)$ of the bivariate basis for several degrees p and trimming parameters t. The labels of the horizontal axis indicate knots of the trimmed basis.

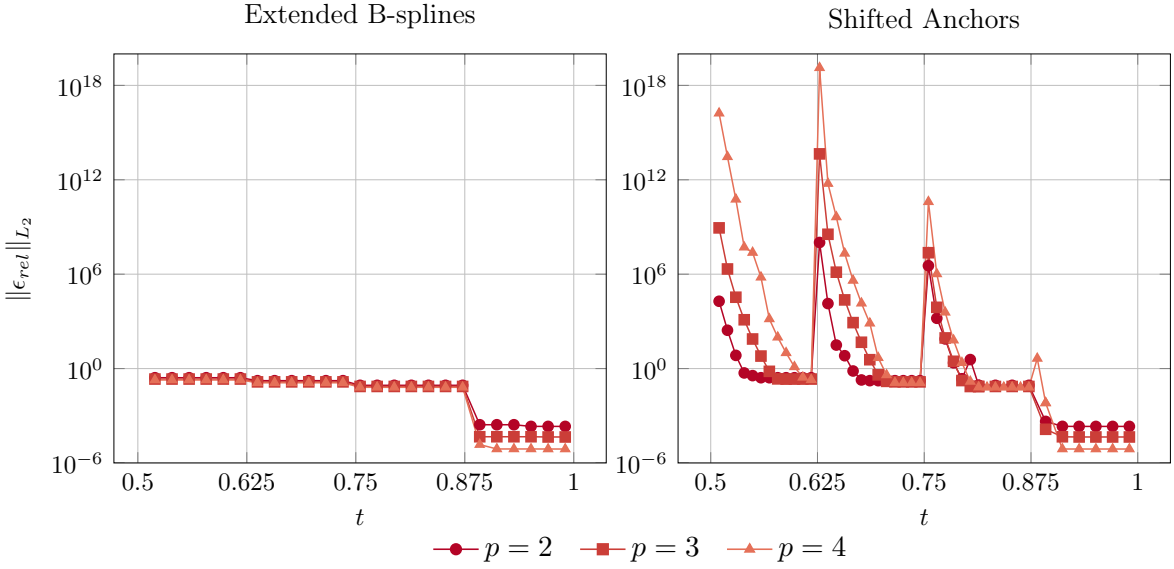

Figure 6.9: Relative interpolation error of the bivariate basis for several degrees p related to the trimming parameter t. The labels of the horizontal axis indicate knots of the trimmed basis.

6.2 Application to Analysis

The extended B-spline basis is applied to an isogeometric BEM framework. The partitioning of integration elements over trimmed surfaces and the setting up of the system matrices is of particular interest in this section.

6.2.1 Integration Elements

Non-trimmed knot spans can be treated as in the regular case, but trimmed ones require a different representation. The detection of trimmed knot spans is performed accordingly to Schmidt et al. [107]. In particular, the following steps are performed:

1. Determine *intersection points* of the trimming curve and the grid produced by the tensor product of the knot vectors.

2. Detect invalid *cutting patterns* and perform knot insertion to obtain valid ones.

3. Assign an *element type* to each knot span based on the valid cutting patterns.

Figure 6.10 shows a trimmed parameter space with related element types and Figure 6.11 depicts the valid cutting patterns considered in this thesis. Elements of type 1 are the regular knot spans, whereas type -1 elements are not considered during the analysis since they are outside of the computational domain. It remains to define the mapping $\mathcal{X}_\xi(\boldsymbol{\xi})$ from the reference element $\hat{\tau} = [-1, 1]^{d-1}$ to knot spans of type $\{3, 4, 5\}$.

By adapting the concept of Coons patches, we use the edges of the trimmed knot span to specify $\mathcal{X}_\xi(\boldsymbol{\xi})$. There is a single edge determined by the trimming curve, the others are straight lines related to the grid of the parameter space. The latter can be represented by the grid points and linear B-splines $B_{j,1}$ based on the knot vector $\Xi = \{-1, -1, 1, 1\}$. The former is obtained by the application of knot insertion so that the trimming curve gets interpolatory at the intersection points. The resulting Bézier segment $\boldsymbol{x}_b$ and the opposing

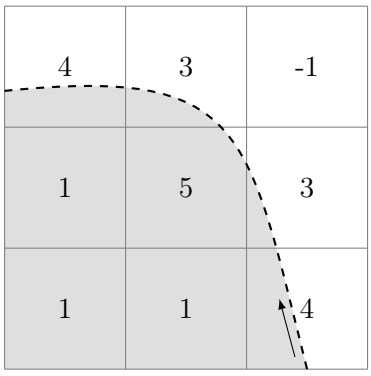

Figure 6.10: Trimmed parameter space and corresponding element types: 1 labels untrimmed knot spans whereas -1 denotes knot spans which are outside of the computational domain. In case of trimmed knot spans the element type indicates the number of interior edges, i.e. 3, 4 or 5.

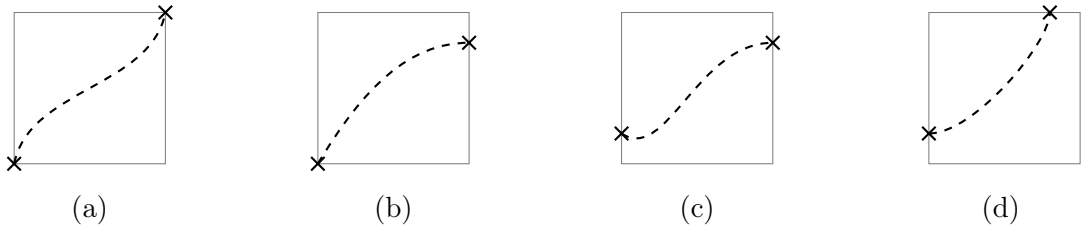

Figure 6.11: Illustration of valid cutting patterns of a single knot span. The actual element type is determined by the direction of the trimming curve which is indicated by the dashed line. The intersection points are highlighted by crosses.

straight edge $\boldsymbol{x}_e$ determine $\mathcal{X}_\xi(\boldsymbol{\xi})$ by the following construction: firstly, it is ensured that both curves are defined on the same parameter range, i.e. $\xi_1 \in [-1, 1]$. Next, the knot vector Ξ_e of $\boldsymbol{x}_e$ is refined by degree elevation and knot insertion so that it is equivalent to the knot vector Ξ_b of $\boldsymbol{x}_b$. Consequently, both edges are described by the same basis functions $B_{i,p}(\xi_1)$. Combined with a linear interpolation $B_{j,1}(\xi_2)$ given by the knot vector $\Xi = \{-1, -1, 1, 1\}$ the integration region of the trimmed knot span is represented by

$$\mathcal{X}_\xi(\boldsymbol{\xi}) \coloneqq \boldsymbol{x}(\xi_1, \xi_2) = \sum_{i=0}^{I-1} \sum_{j=0}^{1} B_{i,p_1}(\xi_1) B_{j,1}(\xi_2)\, \boldsymbol{c}^r_{i,j} \tag{6.16}$$

where $\boldsymbol{c}^r_{i,j}$ denote the control points of $\boldsymbol{x}_b$ and $\boldsymbol{x}_e$ within the parametric space. In case of the element type 3 the opposite edge $\boldsymbol{x}_e$ degenerates to a point. Moreover, an element of type 5 can be treated by subdividing it into three triangular parts. The local mapping $\mathcal{X}_\xi(\boldsymbol{\xi})$ is exemplary shown in Figure 6.12. It is noteworthy that the integration points do not coincide at the degenerated point since open quadrature rules are used.

Remark: Regarding singular integration the position of a collocation point within the reference element may be needed. The corresponding intrinsic coordinates $\boldsymbol{\xi}$ are obtained by point inversion. For more details regarding this procedure is referred to [93].

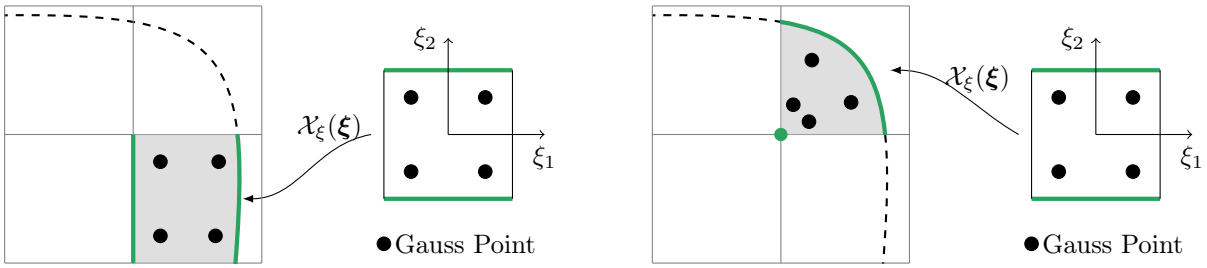

(a) Regular Local Coons Patch (b) Degenerated Local Coons Patch

Figure 6.12: Mapping $\mathcal{X}_\xi(\boldsymbol{\xi})$ from the reference element to the B-spline parameter space. The related knot span is marked in gray, the dashed line represents the trimming curve, circles indicate quadrature points and higher degree edges, i.e. $p > 1$, are highlighted in green.

6.2.2 System of Equations

The approach presented in the previous section permits a proper integration over the visible part Ω_p of a patch, since the partition of integration elements τ is such that

$$\Omega_p = \bigcup_{i=1}^{I} \tau_i \, . \tag{6.17}$$

In order to set up the system of equations for the analysis, basis functions have to be integrated within each τ. If extended B-splines $B^e_{i,p}$ are involved, they could be evaluated directly by equation (6.1). However, they can be included into the simulation without being considered during the integration process as well. In particular, integration is performed with the original basis functions $B_{i,p}$, $i \notin \mathbb{K}$, where the index-set $\mathbb{K}$ denotes all B-splines $B_{k,p}$ which are completely outside of the domain, i.e. $\text{supp}\{B_{k,p}\} \notin \Omega_p$. In other words, the computation of system matrix entries does not differ from the regular case of non-trimmed patches despite the tailored mapping $\mathcal{X}_\xi(\boldsymbol{\xi})$ from the reference element to the parameter space which is applied for trimmed knot span.

Consequently, the resulting system of equations $\mathbf{K} \in \mathbb{R}^{n \times m}$ is rectangular, where n denotes the number of collocation points and m represents the total number of integrated $B_{i,p}$, $i \notin \mathbb{K}$. In order to obtain a square matrix an *extension operator* $\mathbf{E} \in \mathbb{R}^{m \times n}$ is introduced. This sparse matrix $\mathbf{E}$ contains all extrapolation weights $e_{i,j}$ including the trivial ones, i.e. $e_{i,i} = 1$. The transformation of the original to the extended B-spline basis is performed by multiplying the extension operator to the left hand side and ride hand side of the system of equation. Regarding a Neumann problem the stabilization is given by

$$\mathbf{K}\mathbf{E}_\varphi \tilde{\mathbf{u}} = \mathbf{V}\mathbf{E}_\psi \tilde{\mathbf{g}}_N \tag{6.18}$$

$$\mathbf{K}_e \tilde{\mathbf{u}} = \mathbf{f} \tag{6.19}$$

where $\tilde{\mathbf{g}}_N \in \mathbb{R}^m, \tilde{\mathbf{u}} \in \mathbb{R}^n$, $\mathbf{f} \in \mathbb{R}^n$ and $\mathbf{K}_e \in \mathbb{R}^{n \times n}$. The subscripts of $\mathbf{E}$ emphasize that the extrapolation weights are related to the basis functions φ and ψ of the Cauchy data. Hence, if the discretization of the known and unknown Cauchy data varies, $\mathbf{E}$ of the left hand side and right hand side of equation (6.18) varies as well. The stable system (6.19) is subsequently solved and the obtained solution $\tilde{\mathbf{u}} \in \mathbb{R}^n$ corresponds to the extended B-splines of the unknown field. In case of multi-patch geometries, the extrapolation weights $e_{i,j}$ of each patch have to be assembled to $\mathbf{E}$ with respect to the global degrees of freedom. However, the application of the extension operator is particularly convenient, if extended B-splines are added to an existing isogeometric code.

7 Numerical Results

In this chapter, isogeometric analysis based on boundary integral equations and independent field approximation is applied to several potential and elasticity problems. Firstly, the convergence behavior is investigated. Secondly, important features and advantages of the proposed solution methods are demonstrated on various examples. Finally, the treatment of trimmed geometries using extended B-splines is examined.

In general, the system of equations is set up by an adaptive numerical integration scheme presented in [82]. This approach ensures an integration accuracy up to a user-defined quadrature tolerance ϵ_Q. For large scale examples a fast solution technique is utilized in order to reduce the computational complexity. In particular, the system matrices are approximated by means of hierarchical matrices ($\mathcal{H}$-matrices). The quality of this approximation is controlled by the accuracy of the applied adaptive cross approximation (ACA) algorithm $\epsilon_{\mathcal{H}}$. The *HLib* library [17] is used for the $\mathcal{H}$-matrix representation and matrix operations. For details on the applied $\mathcal{H}$-matrices implementation the interested reader is referred to [82, 135].

The present implementation is part of the research software BEFE++. The commercial NURBS modeling tool Rhinoceros was used to define the geometry models. CAGD data is directly transfered to the analysis software using the IGES standard exchange format. Hence, a seamless integration of design and analysis is obtained.

7.1 Convergence Studies

The convergence behavior of the proposed methods is demonstrated on various examples. Figure 7.1 shows the general test setting for a circular cavity in an infinite domain Ω. The boundary of the domain is defined by Γ and the outward normal $\mathbf{n}$ points into the void, denoted by Ω^-. The fundamental solution $\mathsf{U}(\tilde{\boldsymbol{x}}, \boldsymbol{y})$ which is evaluated at source points $\tilde{\boldsymbol{x}} \in \Omega^-$ is applied as boundary condition at $\boldsymbol{y} \in \Gamma$. In particular, $\boldsymbol{y}$ represents anchors and quadrature points of a BEM and Nyström analysis, respectively.

Remark: The applied test setting does not incorporate geometry approximation errors. Since isogeometric analysis exploits the most feasible geometry representation available, this contribution is negligible.

In order to study the accuracy of the discretized single layer operator $\mathbf{V}$ and double layer operator $\mathbf{K}$ independently, the problem is solved by the indirect boundary integral formulations (3.29) and (3.30). For the latter, the test setting is slightly changed, since an interior problem has to be solved instead of an exterior one. However, based on the computed density on Γ, interior results are derived at several field points $\hat{\boldsymbol{x}} \in \Omega$ and the point-wise error ϵ_h is measured by

$$\epsilon_h = u(\hat{\boldsymbol{x}}) - \mathsf{U}(\tilde{\boldsymbol{x}}, \hat{\boldsymbol{x}}) \qquad \forall \hat{\boldsymbol{x}} \in \Omega,\, \tilde{\boldsymbol{x}} \in \Omega^-. \tag{7.1}$$

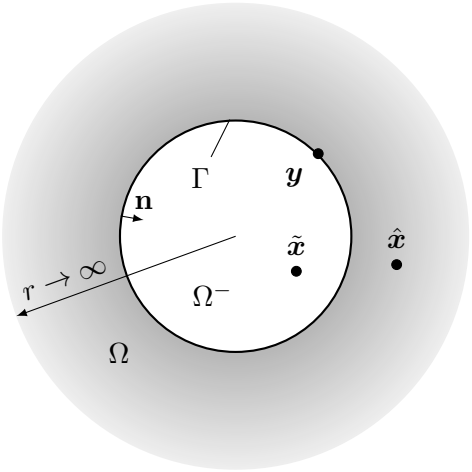

Figure 7.1: Exterior problem given by a circular boundary Γ and an exemplary source $\tilde{\boldsymbol{x}} \in \Omega^-$ and field point $\hat{\boldsymbol{x}} \in \Omega$.

The approximation quality of $\mathbf{V}$ and $\mathbf{K}$ is given by the maximum-norm $\|\epsilon_{rel}\|_\infty$ of the corresponding relative error

$$\epsilon_{rel} = \frac{\epsilon_h}{\mathsf{U}(\tilde{\boldsymbol{x}}, \hat{\boldsymbol{x}})}. \tag{7.2}$$

Further the direct boundary integral formulation (3.31) may be applied to a pure Neumann or Dirichlet problem. The boundary condition for the former is

$$t(\boldsymbol{y}) = \mathsf{T}(\tilde{\boldsymbol{x}}, \boldsymbol{y}) \qquad \forall \boldsymbol{y} \in \Gamma,\, \tilde{\boldsymbol{x}} \in \Omega^- \tag{7.3}$$

and the error is determined by

$$\epsilon_h = u(\boldsymbol{y}) - \mathsf{U}(\tilde{\boldsymbol{x}}, \boldsymbol{y}) \qquad \forall \boldsymbol{y} \in \Gamma,\, \tilde{\boldsymbol{x}} \in \Omega^- \tag{7.4}$$

where $u(\boldsymbol{y})$ is the obtained solution. In contrast to the indirect setting, equation (7.4) is evaluated on Γ. Hence, the approximation error can be measured with respect to the L_2-norm, i.e. $\|\epsilon_{rel}\|_{L_2}$. For a Dirichlet problem, the boundary conditions are $u(\boldsymbol{y}) = \mathsf{U}(\tilde{\boldsymbol{x}}, \boldsymbol{y})$ and $\mathsf{T}(\tilde{\boldsymbol{x}}, \boldsymbol{y})$ provides the reference solution. The convergence plots are related to either the degrees of freedom n or a normalized element diameter

$$h = \left(\frac{A^\tau_{max}}{A} \right)^{1/(d-1)}. \tag{7.5}$$

Equation (7.5) provides a dimensionless parameter h which is similar to the element length in classical analysis with finite elements. Hence, it refers to a length in $\mathbb{R}^2$ and an area in $\mathbb{R}^3$. The largest element size is denoted by A^τ_{max} and related to A which is the whole length or area of Γ. This measure will be used if a *uniform* h-refinement is employed. According to the concept of independent field approximation, refinement is only applied to the discretization of the Cauchy data, while the representation of the geometry remains

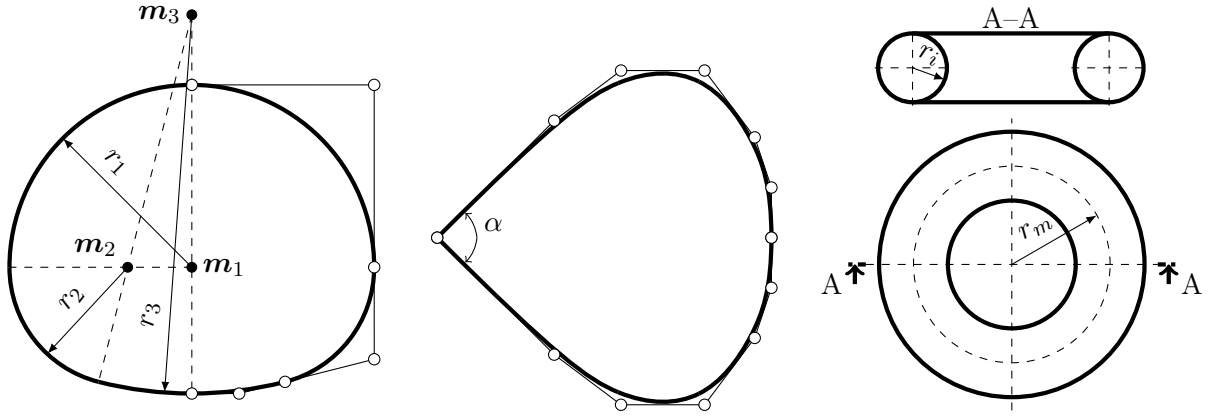

(a) Tunnel (b) Teardrop (c) Torus

Figure 7.2: Geometries taken for the convergence studies referring to: (a) smooth domains in 2d, (b) non-smooth domains in 2d and (c) smooth 3d domains.

unchanged.

The investigated geometries are summarized in Figure 7.2. A smooth tunnel cross section defined by circular arcs is shown in Figure 7.2(a). Their midpoints are $\boldsymbol{m}_1 = (0.0, 0.0)^\intercal$, $\boldsymbol{m}_2 = (1.6, 0.0)^\intercal$ and $\boldsymbol{m}_3 = (0.0, 6.3)^\intercal$ with the related radii $r_1 = 4.55$, $r_2 = 2.95$ and $r_3 = 9.45$. These dimensions are scaled by 100 such that the geometry's diameter is less than 1.00 in order to deal with the occurring logarithmic fundamental solution. In Figure 7.2(b) a non-smooth teardrop shape determined by its opening angle $\alpha = 90°$ is shown. The upper part is defined by a cubic B-spline curve and the corresponding control points $\boldsymbol{c}_i$ are listed in Table 7.1. For the lower part the y-coordinates are mirrored, i.e. multiplied by -1. The three dimensional example 7.2(c) is a torus defined by the radii r_i and r_m which will be specified in the subsequent Section 7.1.1.3 and Section 7.1.2.3, respectively.

$\boldsymbol{c}_0$	$\boldsymbol{c}_1$	$\boldsymbol{c}_2$	$\boldsymbol{c}_3$	$\boldsymbol{c}_4$	$\boldsymbol{c}_5$	$\boldsymbol{c}_6$
0.0000	0.2062	0.3241	0.4714	0.5598	0.5893	0.5893
0.0000	0.2062	0.2946	0.2946	0.1768	0.0884	0.0000

Table 7.1: Control points values of the teardrop geometries upper part.

7.1.1 Isogeometric Boundary Element Method

This section focuses on the convergence properties of the proposed isogeometric BEM formulation which employs subparametric patches. Optimal convergence is achieved, if a rate of convergence $\mathcal{O}\left(h^{-p-1}\right)$ is obtained [5, 102]. While this statement is valid for most test cases, a rate of $\mathcal{O}\left(h^{-p-2}\right)$ may be expected for even degrees p, if the indirect boundary integral formulation with the single layer operator is applied [115]. Related error estimates usually refer to smooth surfaces and small h only. In general, some refinement steps are necessary until the predicted behavior can be observed.

7.1.1.1 Tunnel

The Lamé-Navier equation is applied to the smooth two dimensional example illustrated in Figure 7.2(a). The corresponding Lamé constants (3.8) are given by the Young's modulus $E = 10\,000\,\mathrm{MPa}$ and Poisson's ratio $\nu = 0.25$. Uniform h-refinement is performed for different degrees $p = \{2, \ldots, 5\}$ by means of knot insertion in the middle of non-zero knot spans. The geometry is represented by NURBS basis functions, since it consists of circular arcs. However, the Cauchy data are discretized either by NURBS or B-splines and their convergence behavior is compared. The integration accuracy is set to $\epsilon_Q = 10^{-11}$ and results are shown up to one magnitude less for the relative error.

In Figure 7.3, the convergence behavior of the discrete integral operators $\mathbf{V}$ and $\mathbf{K}$ by means of the indirect boundary integral formulations (3.29) and (3.30) is shown. The results of the Neumann and Dirichlet problems due to the direct formulation (3.31) are

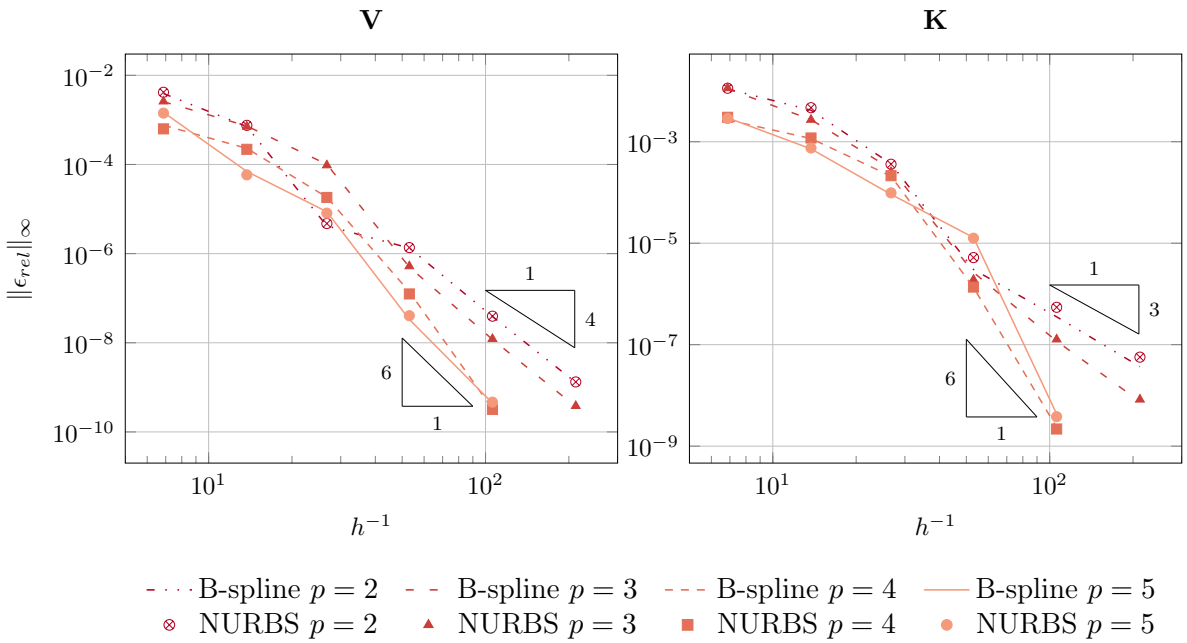

Figure 7.3: Relative error of the indirect formulation on the tunnel example for the discrete single layer operator $\mathbf{V}$ and double layer operator $\mathbf{K}$ measured in the maximum-norm and related to the normalized element diameter h.

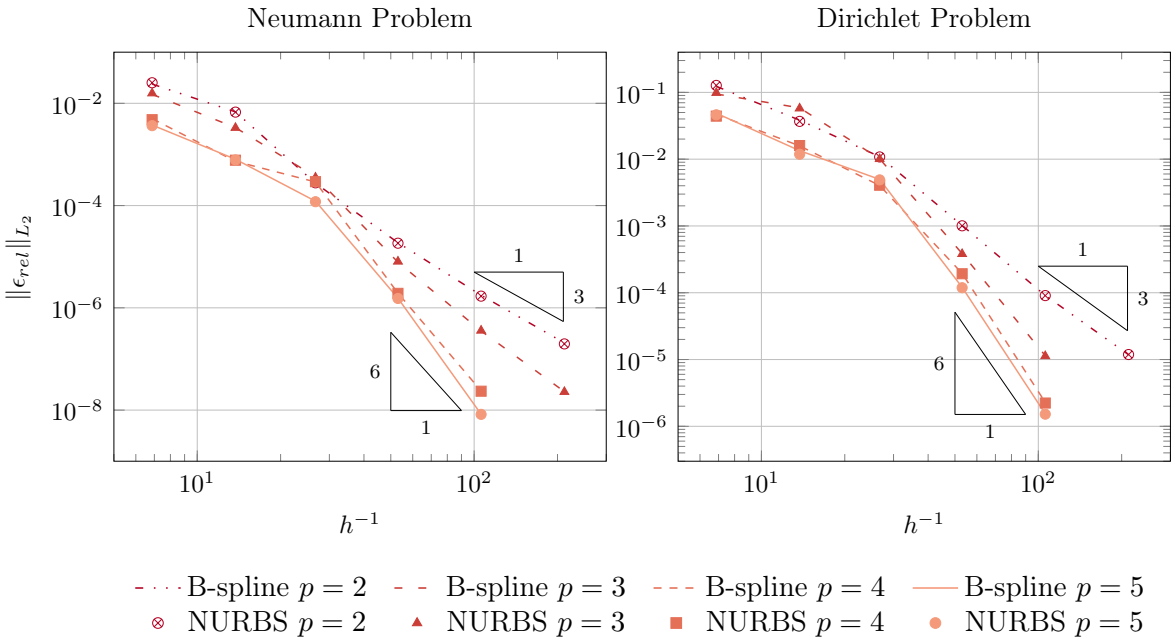

Figure 7.4: Relative error of the Neumann and Dirichlet problems on the tunnel geometry measured in L_2-norm and related to the normalized element diameter h.

presented in Figure 7.4. In these graphs, lines and marks are used to distinguish between NURBS and B-spline discretizations of the Cauchy data for various degrees p. Triangles indicate the optimal rate of convergence for the lowest and highest degree, i.e. $p = \{2, 5\}$. Note that the convergence rates corresponding to $\mathbf{V}$ varies for even and odd degrees. Comparing the results of B-spline and NURBS discretizations indicates that they lead to almost identical results. Moreover, it is apparent that optimal convergence is achieved for all cases.

7.1.1.2 Teardrop

The convergence behavior of the isogeometric BEM on a non-smooth geometry is investigated by means of a potential problem. The corresponding geometry is depicted in Figure 7.2(b). Discontinuous collocation is applied in order to treat the occurring corner of the cubic curve. Refinement is performed by uniform knot insertion and the integration error is set to $\epsilon_Q = 10^{-10}$.

The results of the discrete boundary integral operators are shown in Figure 7.5. The relative L_2-error of the Neumann and Dirichlet problems is illustrated in Figure 7.6. In contrast to the smooth case of Section 7.1.1.1, the discrete single layer operator $\mathbf{V}$ seems to converge with a rate of $\mathcal{O}\left(h^{-p-1}\right)$ for even degree, i.e. $p = 4$, as well. It should, however, be noted that the error of the finest discretization is already close to ϵ_Q. All other cases provide the same rates as in the smooth tunnel example.

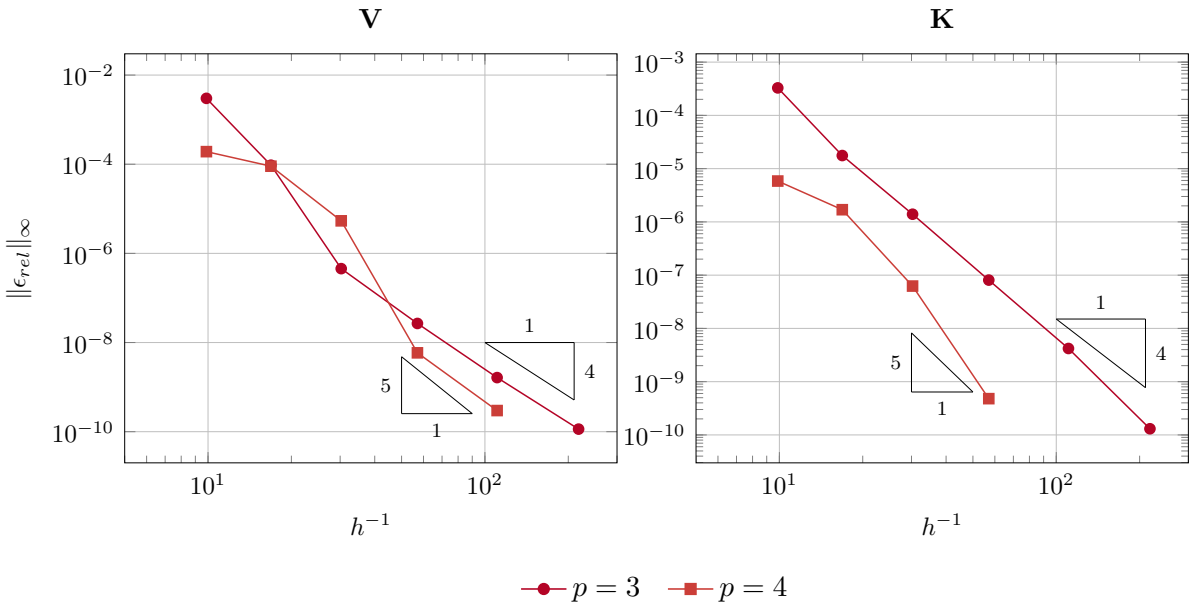

Figure 7.5: Relative error of the indirect teardrop example for the discrete single layer operator $\mathbf{V}$ and double layer operator $\mathbf{K}$ measured in the maximum-norm and related to the normalized element diameter h.

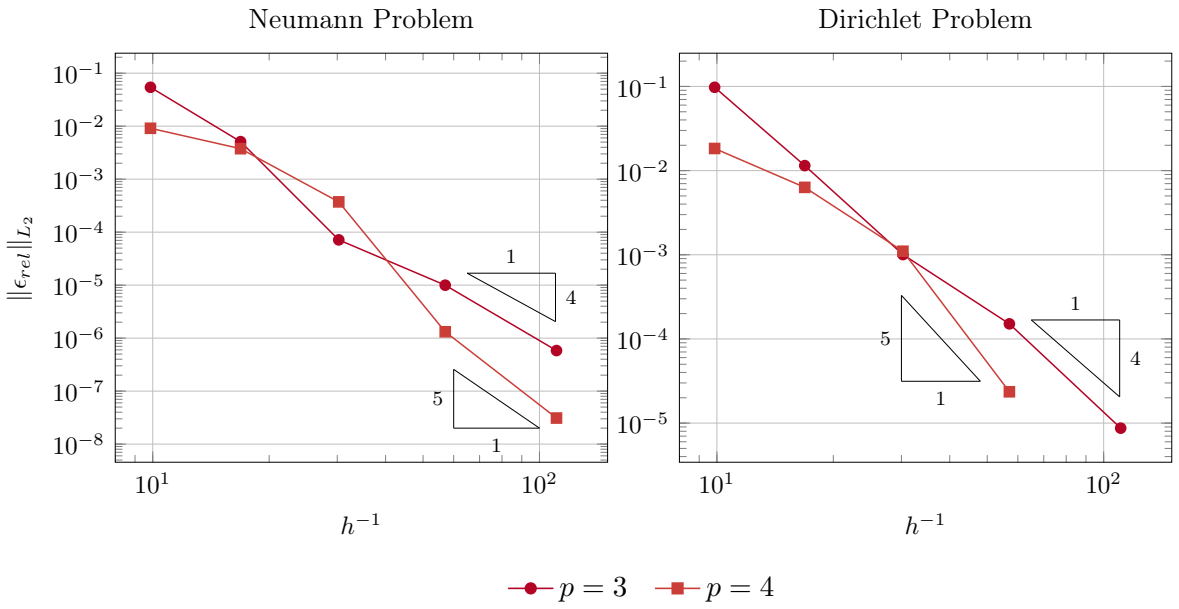

Figure 7.6: Relative error of the Neumann and Dirichlet problems on the teardrop geometry measured in L_2-norm and related to the normalized element diameter h.

7.1.1.3 Torus

An elasticity problem in three dimensions is investigated. The elastic material parameters are $E = 1\,\mathrm{MPa}$ and $\nu = 0.30$. The geometry is defined by a torus with radii $r_m = 5.00\,\mathrm{m}$ and $r_i = 1.00\,\mathrm{m}$, according to Figure 7.2(c). In three dimensions the numerical complexity increases rapidly with the number of degrees of freedom, especially in case of the Lamé-Navier equation. Hence, the resulting system of equations is approximated by means of $\mathcal{H}$-matrices. The ACA accuracy $\epsilon_{\mathcal{H}}$ as well as the integration error ϵ_Q are set to 10^{-7}.

Figure 7.7 depicts the convergence for the indirect formulation with the single layer operator $\mathbf{V}$ and double layer operator $\mathbf{K}$ and for the direct formulation it is shown in Figure 7.8. Desired rates of convergence are marked by triangles for degrees $p = \{2, 5\}$ in each graph. Optimal convergence rates are obtained in all cases.

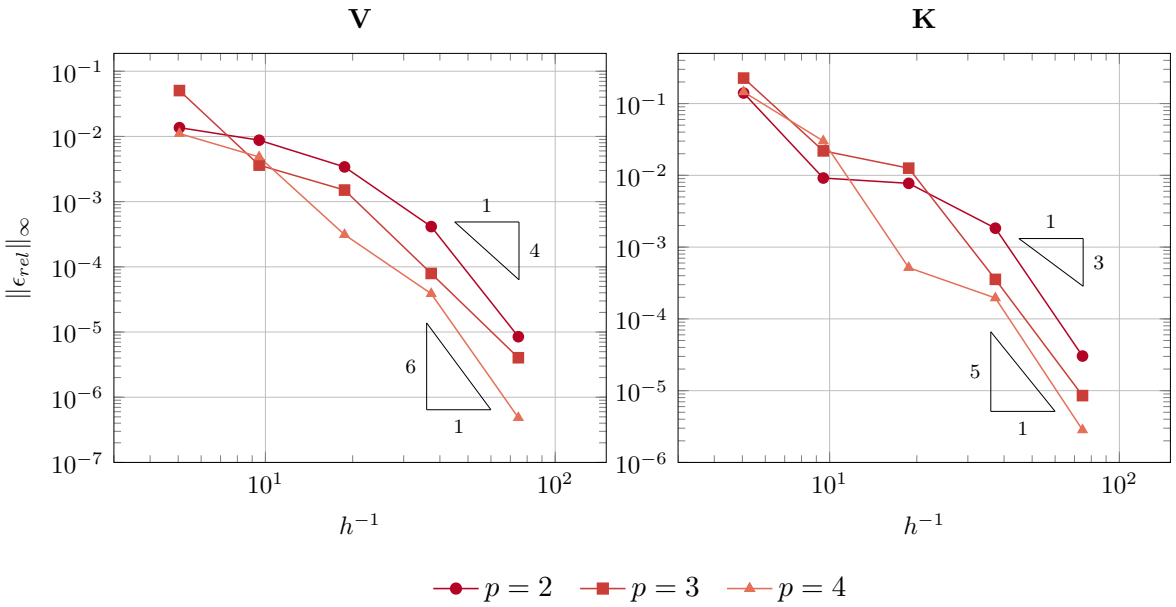

Figure 7.7: Relative error of the indirect torus example for the discrete single layer operator $\mathbf{V}$ and double layer operator $\mathbf{K}$ measured in the maximum-norm and related to the normalized element diameter h.

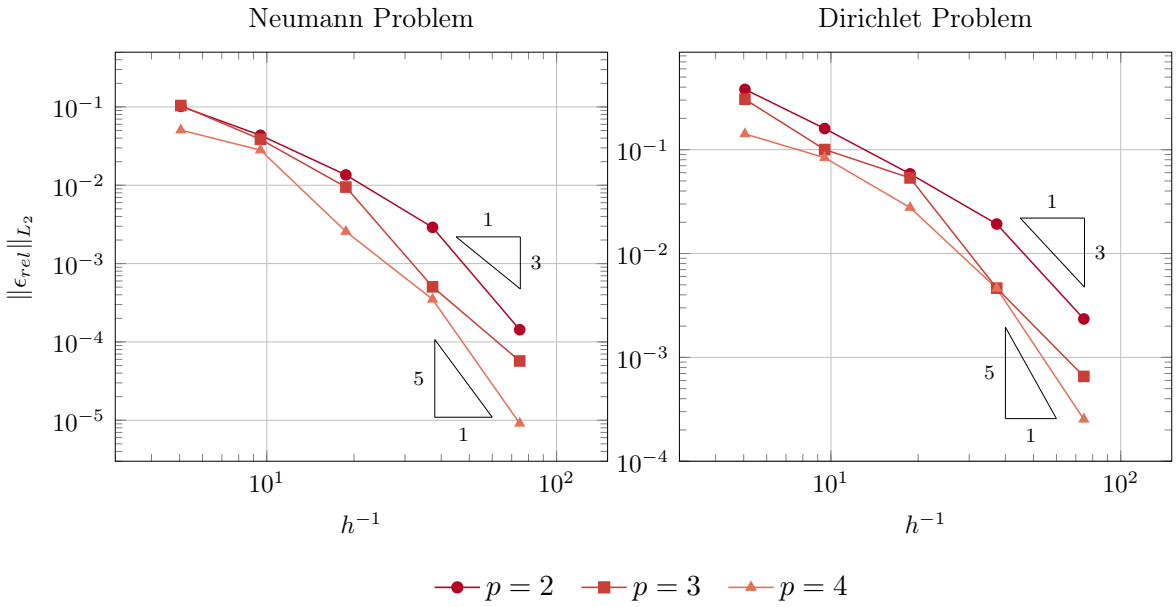

Figure 7.8: Relative error of the Neumann and Dirichlet problem on the torus geometry measured in L_2-norm and related to the normalized element diameter h.

7.1.2 Isogeometric Nyström Method

Convergence studies of the proposed locally corrected isogeometric Nyström method are provided in this section. Regions subjected to the local correction procedure are determined by the admissibility factor η specified in equation (4.13). On smooth surfaces, a rate of convergence $\mathcal{O}\left(h^{-p_q-1}\right)$ is expected for the indirect boundary integral equations with the double layer operator $\mathbf{K}$ applied to Laplace problems in two and three dimensions [5]. The literature is relatively sparse as soon as the Lamé-Navier equation is concerned. Its mathematical analysis is more involved, because the related boundary integral is evaluated in the sense of a Cauchy principal value. The indirect boundary integral equation with the single layer operator $\mathbf{V}$ requires additional attention as well. It is not compact anymore and the related fundamental solution is logarithmic for two dimensional problems [102]. Consequently, the straightforward application of the single layer operator $\mathbf{V}$ leads to linear rates, independent of the quadrature rule applied. Higher rates may be re-established by the application of kernel splitting or other techniques [31, 55] which are beyond the scope of this thesis. In addition, corners reduce the convergence rate, since the gradient of the solution becomes singular. Mesh grading towards the corner is applied according to equation (4.21) to restore higher order convergence rates.

7.1.2.1 Tunnel

The convergence of the isogeometric Nyström method on smooth geometries is investigated by solving Laplace and Lamé-Navier equations on the tunnel geometry shown in Figure 7.2(a). The Lamé constants are equal to those of Section 7.1.1.1. The study is focused on the performance of the discrete integral operators $\mathbf{V}$ and $\mathbf{K}$ by means of

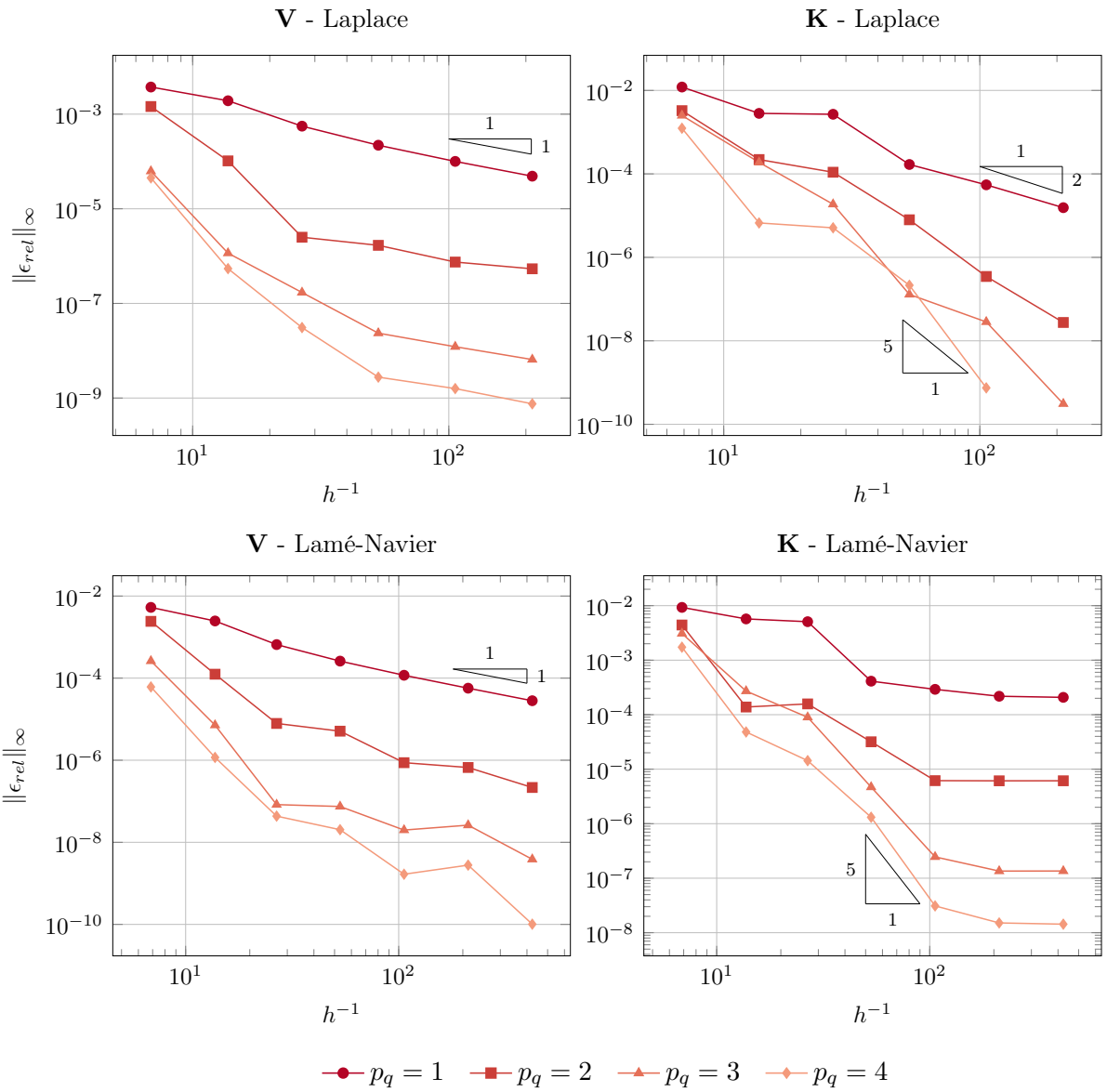

Figure 7.9: Relative error of the indirect Laplace and Lamé-Navier problems on the tunnel example for the discrete single layer operator $\mathbf{V}$ and double layer operator $\mathbf{K}$ measured in the maximum-norm with respect to the mesh parameter h.

the indirect boundary integral formulations (3.29) and (3.30). Various quadrature orders $p_q = \{1, \dots, 4\}$ are applied to uniform discretizations with decreasing element diameter h. The admissibility factor for the local correction is chosen to be $\eta = 2.0$ and the accuracy of the involved numerical integration is set up to $\epsilon_Q = 10^{-11}$.

The results are summarized in Figure 7.9. All graphs corresponding to $\mathbf{V}$ show linear behavior as expected. The discrete operator $\mathbf{K}$ obeys the theoretical higher order convergence rates for the Laplace problem, but the convergence ceases at a certain level of h-refinement in the Lamé-Navier case. However, it is noteworthy that there is a significant offset between the different discretizations with respect to the applied quadrature order p_q

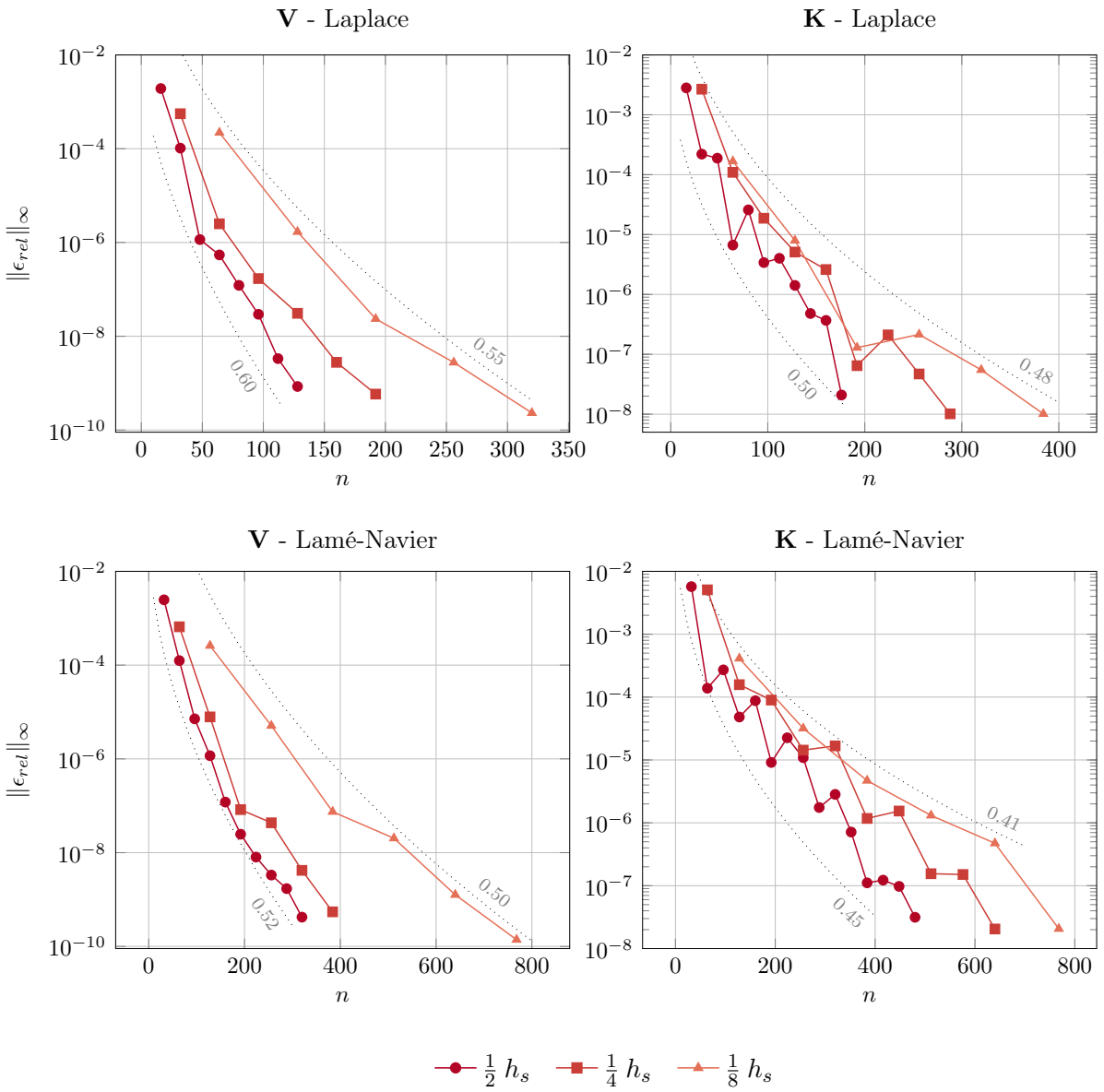

Figure 7.10: Convergence of the discrete single layer **V** and double layer potential **K** on the smooth tunnel geometry due to p-refinement. The corresponding exponential function (7.6) is indicated by dotted lines and the aligned number denotes the exponential factor s.

in all cases. Hence, p-refinement may be a preferable strategy. The related performance is shown in Figure 7.10. In particular, the first three h-refined representation of the initial mesh h_s are taken as starting point and the results of each are improved by increasing the quadrature order p_q. The observed convergence behavior can be described with respect to the degrees of freedom n by

$$\|\epsilon_{rel}\|_\infty = C \exp^{(-n^s)} . \tag{7.6}$$

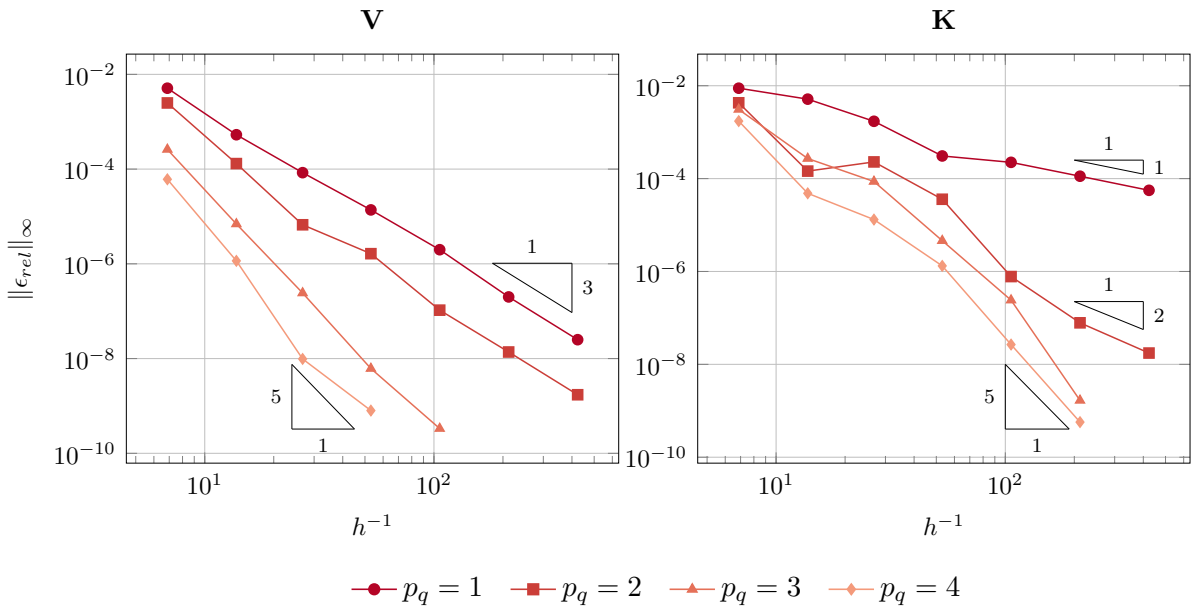

Figure 7.11: Indirect Lamé-Navier problem on tunnel example solved by the Nyström method with a very large admissibility factor η. The relative error is measured in the maximum-norm and plotted with respect to the mesh parameter h.

The constant C is determined by the mesh size and the exponential factors s varies from 0.41 to 0.60 for the numerical example investigated.

At this point, it should be emphasized that the straightforward implementation presented in this thesis does not employ regularization techniques which may improve the convergence behavior. In addition, it was observed that reasonable variation of the admissibility factor η does not cause essential impact. Nonetheless, the convergence rates improve if η is chosen such that local correction is always applied. The results related to Lamé-Navier equation are depicted in Figure 7.11. Unfortunately, this approach is not really useful since it destroys the point-wise nature of the Nyström method and increases the numerical effort significantly.

7.1.2.2 Teardrop

Due to the observations of the previous section, this example focuses on convergence of the boundary integral equations of the second kind (3.30), i.e. the discrete double layer operator $\mathbf{K}$. A Laplace problem is solved on the teardrop-shaped domain illustrated in Figure 7.2(b). The corner with opening angle $\alpha = 90°$ introduces a singularity of the solution, since its gradient becomes singular. Corresponding convergence behavior is studied for various quadrature orders $p_q = \{1, \ldots, 5\}$ and two different refinement strategies. On one hand, uniform h-refinement is applied. The other scheme employs grading towards the corner, which is determined by equation (4.21). In particular, the number of sub-elements is set to $\ell = 6$ and the Hölder constant is $\upsilon = 1$. Moreover, the admissibility factor for the local correction is chosen to be $\eta = 6.0$ to deal with small elements at the corner. The local correction is performed with an integration accuracy of $\epsilon_Q = 10^{-11}$.

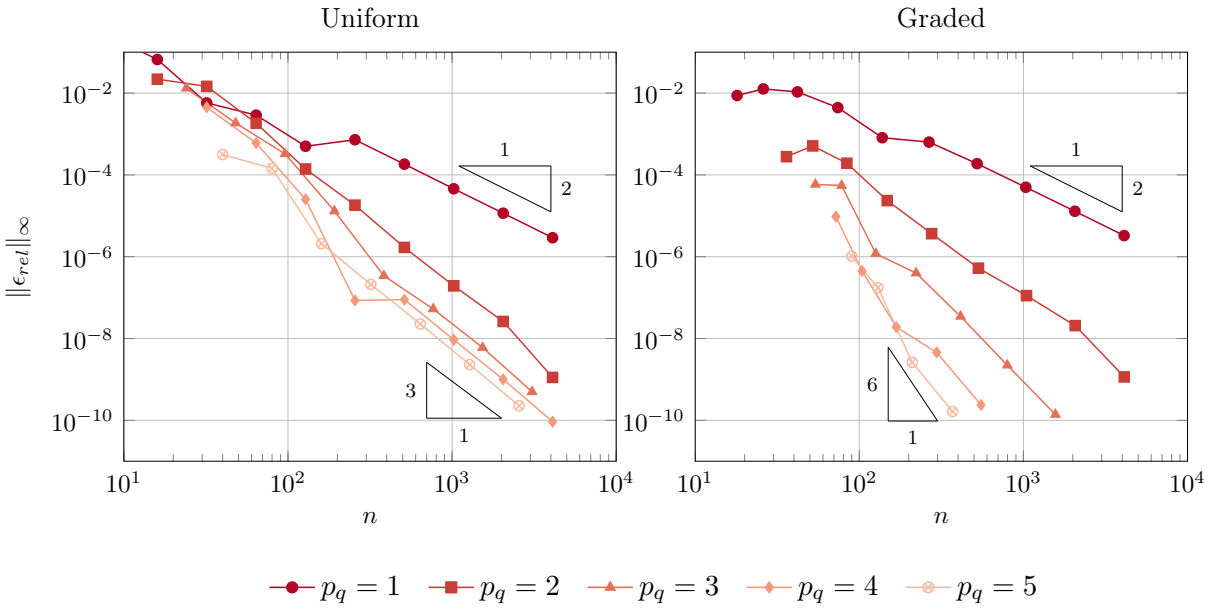

Figure 7.12: Relative error of the indirect teardrop example for the discrete double layer operator $\mathbf{K}$ measured in the maximum-norm with respect to the number of degrees of freedom n. The h-refinement has been performed either uniformly (left) or by grading towards the corner (right).

The occurring convergence rates are depicted in Figure 7.12. Note that the relative error of both discretizations is illustrated with respect to degrees of freedom n. It is apparent that higher order convergence can not be obtained by uniform h-refinement. However, it can be re-established by the proposed grading procedure. In all test cases, the full convergence of the indicate boundary integral equation with the double layer operator $\mathbf{K}$ is restored.

7.1.2.3 Torus

The Laplace and Lamé-Navier equations are solved on a torus with radii $r_m = 0.90\,\mathrm{m}$ and $r_i = 0.20\,\mathrm{m}$. The Lamé constants are given by Poisson's ratio $\nu = 0.3$ and Young's modulus $E = 1.00\,\mathrm{GPa}$. The admissibility factor for the local correction is set to $\eta = 4.0$ and the involved numerical integration is performed with a tolerance of $\epsilon_Q = 10^{-10}$.

The results for the Laplace equation are outlined for both operators in Figure 7.13. The Lamé case is shown in Figure 7.14 focusing on the indirect boundary integral equation (3.30) with the double layer operator $\mathbf{K}$. Similar to the two dimensional example of Section 7.1.2.1, convergence rates of $p_q + 1$ for $\mathbf{K}$ and linear behavior for $\mathbf{V}$ are observed. Regarding p-refinement the error follows equation (7.6) with an exponential factors $s \approx 0.3$. Note that there is no convergence plateau in the graphs of to the Lamé problem, in contrast to the two dimensional case. However, it is uncertain if this holds for further h-refinement steps.

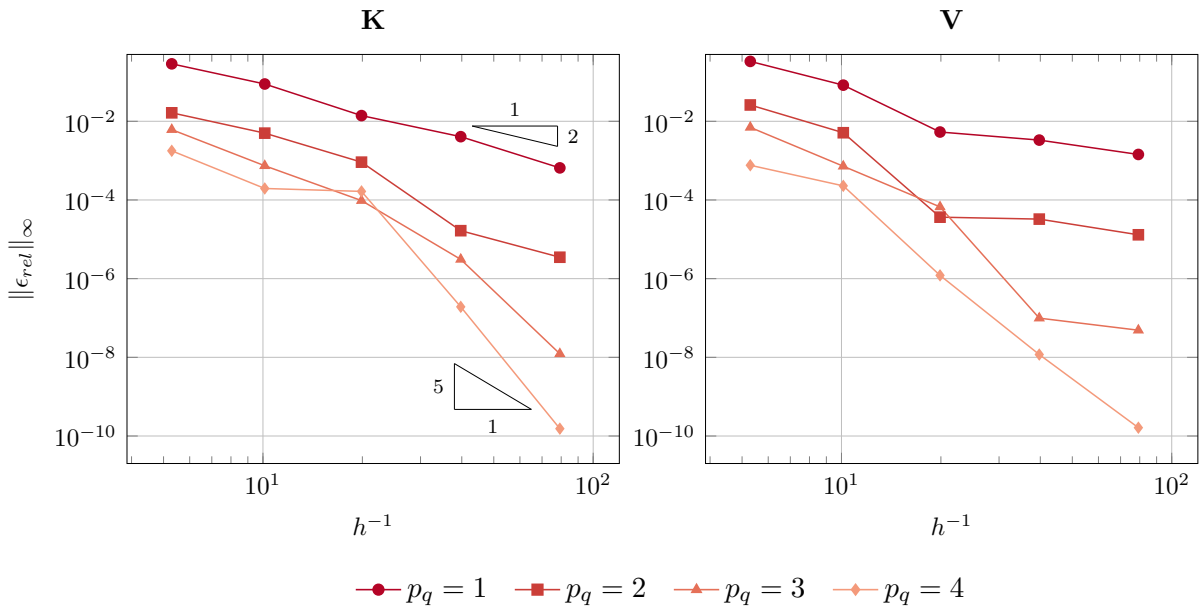

Figure 7.13: Relative error of the indirect Laplace problem on the torus for the discrete single layer operator $\mathbf{V}$ and double layer operator $\mathbf{K}$ measured in the maximum-norm with respect to the mesh parameter h.

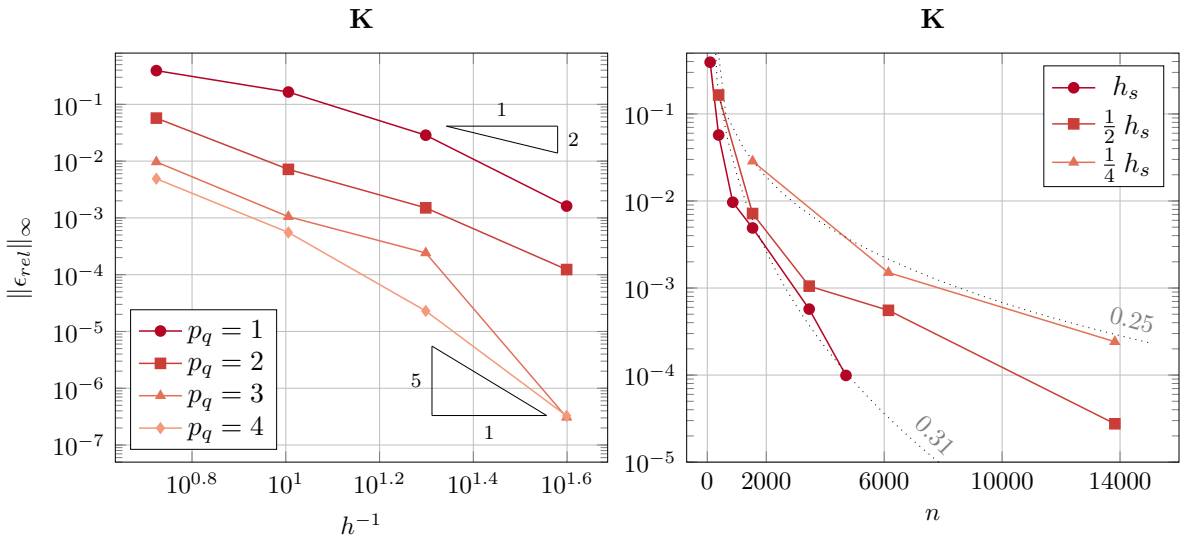

Figure 7.14: Convergence of the discrete double layer operator $\mathbf{K}$ on the torus for the Lamé-Navier problem. Results are shown for h-refinement (left) and p-refinement (right).

7.2 Computational Effort

The subsequent sections contain miscellaneous examples emphasizing features and benefits of combining isogeometric analysis, boundary integral equations and independent field approximation. Sections (7.2.1) to (7.2.3) are dedicated to the application of independent field approximation in the context of an isogeometric BEM analysis and its capability to save computational time and storage. Regarding the isogeometric Nyström method, the ability of local refinement and the influence of the admissibility factor of the local correction is outlined at the end. The direct boundary integral formulation (3.31) is applied in general.

7.2.1 Spherical Excavation

An excavation of a spherical cavity with radius $r_s = 5.00\,\mathrm{m}$ is investigated. Isotropic elastic material is considered with Poisson's ratio $\nu = 0.30$ and Young's modulus $E = 1000\,\mathrm{MPa}$. Hydrostatic stress $\sigma_0 = 1.00\,\mathrm{MPa}$ is applied as loading which leads to a uniform internal pressure along the excavation surface. The resulting radial displacement u_r can be determined analytically by

$$u_r = \sigma_0 \frac{1+\nu}{2\,E} \frac{r_s^3}{r^2} \tag{7.7}$$

where r denotes the distance of the point observed to the sphere's center. Hence, the reference solution for u_r along the boundary, i.e. $r = r_s$, is $3.25 \times 10^{-3}\,\mathrm{m}$.

The problem is solved by conventional and isogeometric BEM simulations. Both approaches employ quadratic basis functions. The conventional BEM meshes approximate the boundary of the computation domain with quadratic Serendipity elements. In the isogeometric case NURBS basis function of degree $p = 2$ are used. In fact, the geometry can be represented exactly by a single NURBS patch which has degenerated edges at each pole of the sphere. This model has been exported from the CAGD software Rhinoceros, where the precision of the exported data was set to $\epsilon_e = 10^{-8}$. Discontinuous collocation is applied in order to deal with the degenerated edges of the model.

The relative error of the radial displacement ϵ_{u_r} as well as the relative deviation of the geometry representation to an analytical sphere ϵ_{geo} are summarized in Table 7.2. Further, three numerical results and their corresponding discretizations are illustrated in Figure 7.16 and Figure 7.15, respectively.

The error ϵ_{geo} demonstrates clearly the superiority of the isogeometric concept concerning accurate geometry representations. The unrefined NURBS patch provides already a precise geometric model, while a large number of Serendipity elements is required for an adequate approximation. Note that ϵ_{geo} correlates to the accuracy of the input data ϵ_e in the isogeometric case. Moreover, the isogeometric solution provides excellent results for u_r despite of the low number of degrees of freedom n. It should, however, be noted that the example suits NURBS basis functions ideally. Such remarkable gaps between isogeometric and conventional BEM solutions can not be expected in general. Nevertheless, conic sections and their three dimensional counterparts, e.g. spheres and cylinders, are very common design elements for which NURBS surpasses the approximation quality of conventional basis functions.

Isogeometric BEM			Conventional BEM		
n	ϵ_{u_r}	ϵ_{geo}	n	ϵ_{u_r}	ϵ_{geo}
216	1.74×10^{-5}	3.42×10^{-8}	483	1.61×10^{-2}	4.76×10^{-1}
288	2.65×10^{-6}	3.42×10^{-8}	2436	1.27×10^{-3}	1.53×10^{-2}
			9312	5.58×10^{-4}	1.81×10^{-3}
			12 120	4.42×10^{-4}	1.10×10^{-3}
			21 858	1.49×10^{-4}	3.21×10^{-4}
			38 886	7.52×10^{-5}	1.08×10^{-4}

Table 7.2: Relative error of solution ϵ_{u_r} and geometry representation ϵ_{geo} of the spherical excavation measured in L_2-norm due to an isogeometric and conventional BEM analysis with quadratic basis functions.

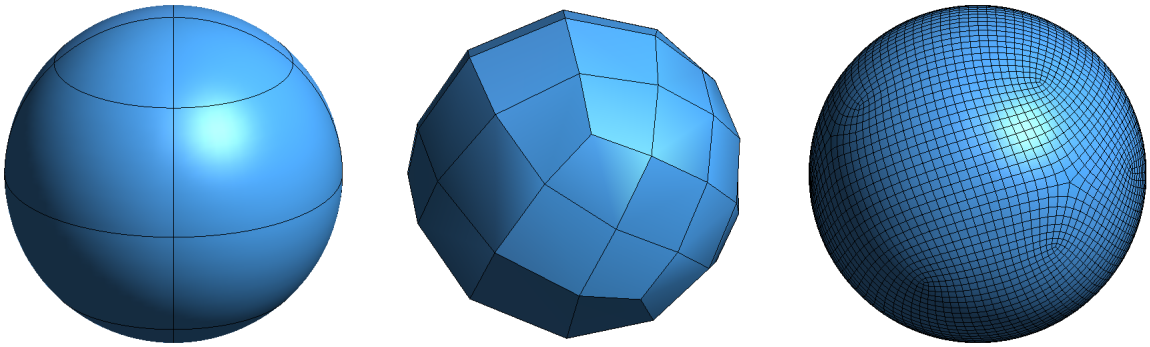

(a) $n = 288$ (b) $n = 483$ (c) $n = 38\,886$

Figure 7.15: Various unknown field discretizations of the spherical cavity with different degrees of freedom n: (a) finest isogeometric BEM, (b) coarsest and (c) finest conventional BEM analysis.

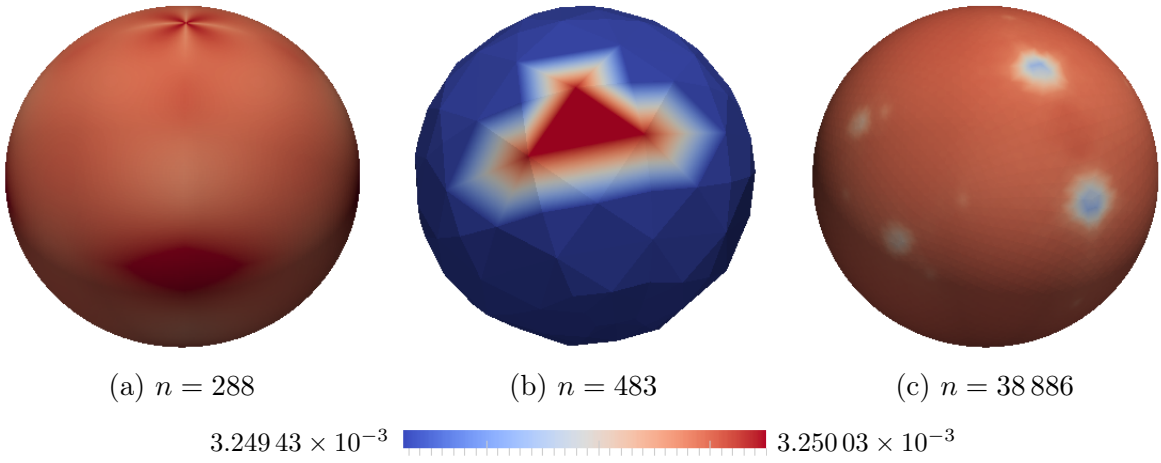

(a) $n = 288$ (b) $n = 483$ (c) $n = 38\,886$

Figure 7.16: Radial displacement u_r of various spherical excavation discretizations: (a) finest isogeometric BEM, (b) coarsest and (c) finest conventional BEM analysis.

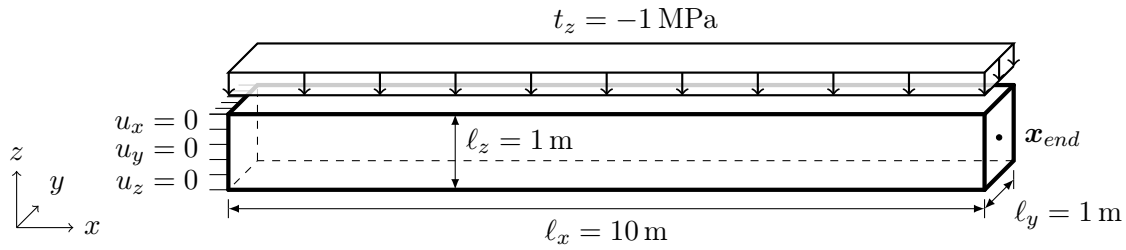

Figure 7.17: Dimensions and boundary conditions of the cantilever beam example.

7.2.2 Cantilever

A three dimensional cantilever beam is considered to investigate the quality of the results and storage requirement of the proposed subparametric discretization. Figure 7.17 illustrates the geometry and boundary conditions of the problem. The elastic material is defined by Poisson's ratio $\nu = 0.0$ and Young's modulus $E = 29\,000\,\mathrm{MPa}$. The problem is discretized with subparametric and isoparametric patches. The former refines the basis of the unknown field only, since the boundary conditions are exactly represented by the initial patch. Hence, the right hand side matrix $\mathbf{R}$ of the system of equations is approximated differently in the two approaches. The difference is expressed by the compression rate

$$c_s = \frac{\mathsf{St}(\mathbf{R}_i)}{\mathsf{St}(\mathbf{R}_s)} \tag{7.8}$$

with $\mathsf{St}(\mathbf{R}_i)$ and $\mathsf{St}(\mathbf{R}_s)$ denoting the storage requirements for the right hand side matrix

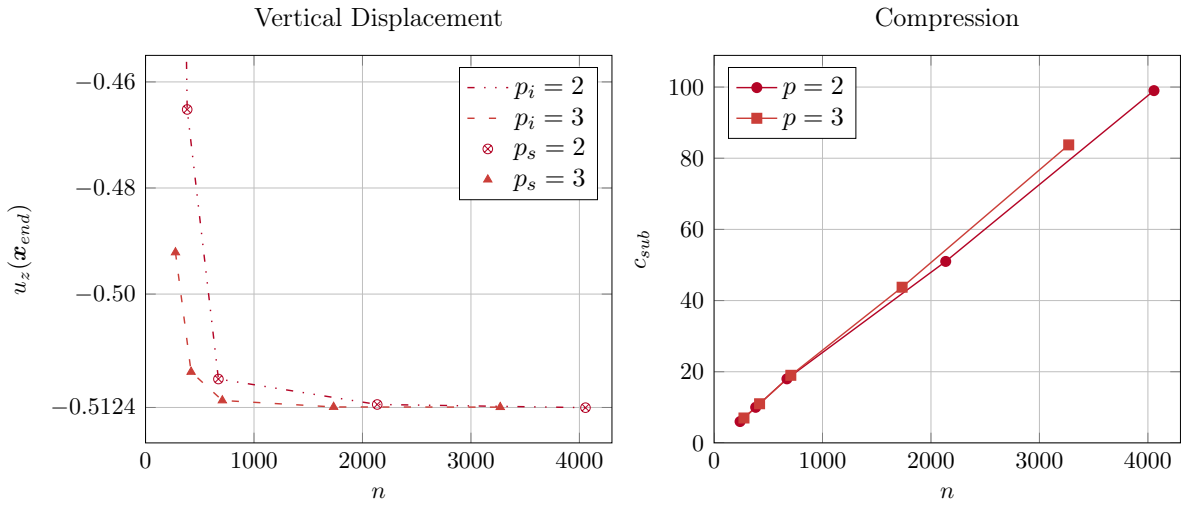

Figure 7.18: Left: vertical displacement of the cantilever beam's end $u_z(\boldsymbol{x}_{end})$ for different polynomial degrees p and degrees of freedom n. Lines indicate the results due to the isogeometric, while markers are used for the subparametric discretization. Right: compression c_s of the right hand side matrix due the application of the subparametric formulation.

due to the iso- and subparametric formulation, respectively. In both cases, matrix entries related to homogeneous boundary conditions, i.e. zero entries, are not measured. In order to verify the quality of the results the vertical displacement u_z of the endpoint $\boldsymbol{x}_{end}$ is determined. Refinement is preformed until Timoshenko's analytic solution, i.e. $u_z(\boldsymbol{x}_{end}) = -0.5214\,\mathrm{m}$, is obtained.

Comparing the resulting displacements $u_z(\boldsymbol{x}_{end})$ and related compressions c_s in Figure 7.18 demonstrates that the subparametric concept leads to almost identical results, although the storage requirements are evidently decreased. In fact, the right hand side matrix of the finest discretizations is 100 times smaller than its isoparametric counterpart.

7.2.3 Crankshaft

In this section, the concept of independent field approximation is applied to a crankshaft example. The geometry is defined by several regular NURBS patches and illustrated in Figure 7.19. Displacements are fixed at the axle and flywheel, while the crank pins are subjected to vertical loading. These boundary conditions are exactly represented by the initial discretization and do not require refinement. The material property is specified by $E = 210\,\mathrm{GPa}$ and $\nu = 0.25$. In order to handle the computational effort the system matrices are approximated by means of $\mathcal{H}$-matrices.

Subparametric and isoparametric discretizations are applied to the problem. They differ not only in the refinement procedure, but the type of basis function used for the representation of the Cauchy data. In particular, B-splines are employed in the subparametric case. The degree of the basis functions related to Cauchy data p_c is either equal to the one of the geometry representation p_g or increased by means of degree elevation, i.e. $p_c = p_g + 1$. Subsequently, knot insertion is used to improve the results. For each simulation, the analysis time t_i and t_s of the isoparametric and subparametric discretization are compared. To be precise, the runtime for the set up of the left hand side $\mathbf{L}$ and the right hand side $\mathbf{R}$ of the block system (4.31) is measured. Each analysis has been performed single-threaded, concurrently for each t_i and t_s and repeated several times. In order to achieve an acceptable computational effort for this study the $\mathcal{H}$-matrix accuracy $\epsilon_{\mathcal{H}}$ as well as the tolerance for the numerical integration ϵ_Q are set to 10^{-3}. The resulting speedup factors t_i/t_s are summarized in Figure 7.20. Figure 7.21 shows the displacements corresponding to the third h-refinement step of the case where $p_c = p_g$.

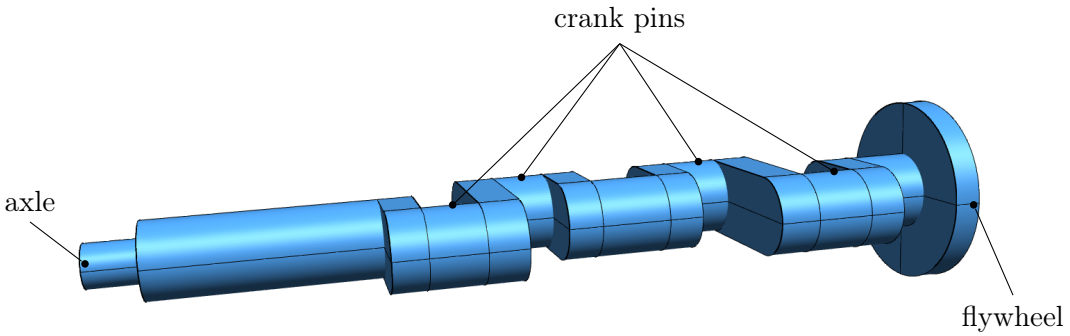

Figure 7.19: Geometry model of the crankshaft.

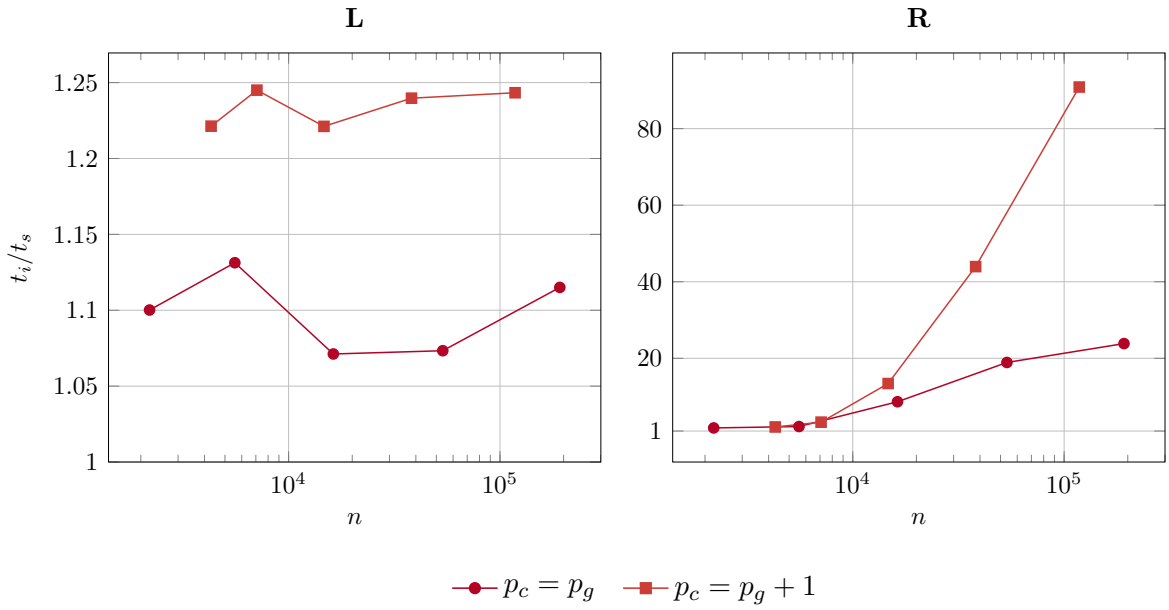

Figure 7.20: Computational time for the set up of **L** and **R** related to various discretization of the crankshaft example as a function of the degrees of freedom n. The runtime of the isoparametric discretization t_i is related to the subparametric one t_s.

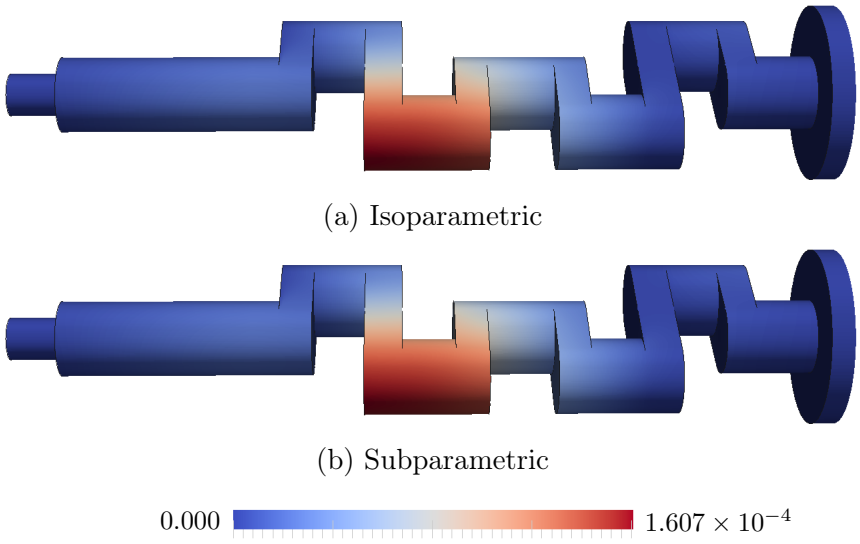

(a) Isoparametric

(b) Subparametric

Figure 7.21: The absolute displacement $|\mathbf{u}|$ of the crankshaft example without degree elevation and three h-refinement steps due to an (a) isoparametric BEM and (b) subparametric BEM discretization.

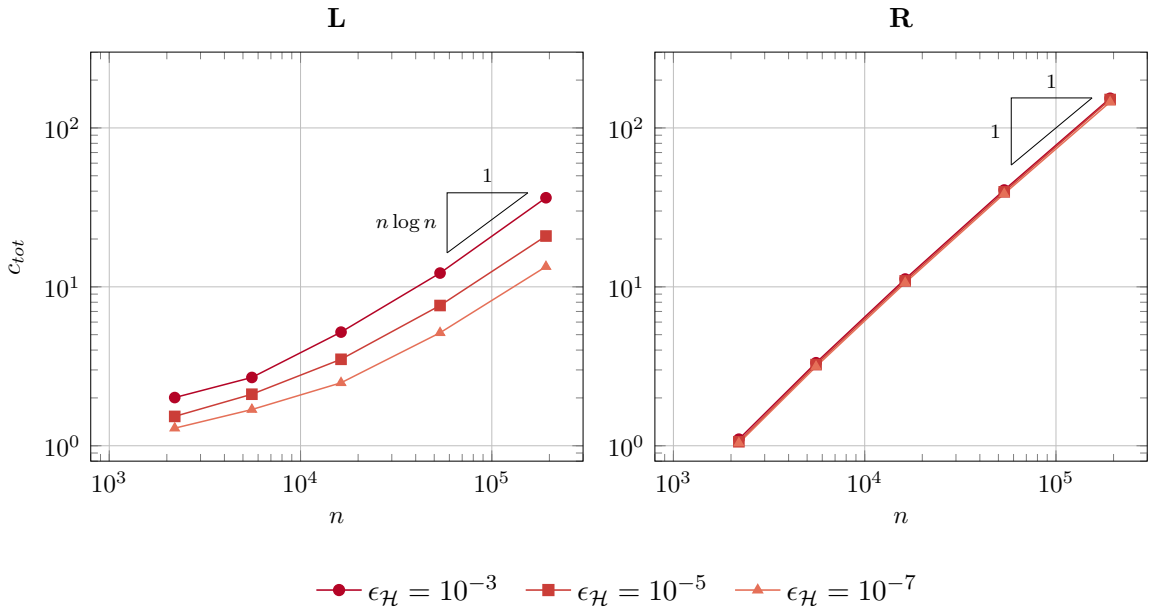

Figure 7.22: Total compression rates c_{tot} for the system matrices of the crankshaft example discretized with subparametric patches as a function of the total degrees of freedom n.

In addition, the storage requirements of the subparametric approach is investigated focusing on those discretizations which are not degree elevated. The total compression rates

$$c_{tot} = \frac{\mathsf{St}(\mathbf{L})}{\mathsf{St}(\mathbf{L}_{\mathcal{H}})} \qquad \text{and} \qquad c_{tot} = \frac{\mathsf{St}(\mathbf{R})}{\mathsf{St}(\mathbf{R}_{\mathcal{H},s})} \tag{7.9}$$

of the left hand and right hand side are compared. The former is solely determined by the $\mathcal{H}$-matrix approximation, whereas the latter is further compressed due to the application of subparametric patches. The matrix approximation is performed with different accuracies, i.e. $\epsilon_{\mathcal{H}} = \{10^{-3}, 10^{-5}, 10^{-7}\}$. The resulting c_{tot} are illustrated in Figure 7.22 with respect to the number of degrees of freedom n.

The shown results indicate that independent field approximation reduces the computational effort regarding both time and storage, especially for the right hand side of the block system of equations. The number of columns of $\mathbf{R}$ is constant for all subparametric discretizations, because known Cauchy data do not need to be refined. Hence, its storage requirement is linear with respect to n, which exceeds the almost linear behavior $\mathcal{O}(n \log n)$ of $\mathcal{H}$-matrices. The efficient geometry evaluation as well as the substitution of NURBS by B-splines are the key factor regarding the faster computation of $\mathbf{L}$ in the subparametric case. The former impact is indicated clearly by the additional offset between the graphs related to $p_c = p_g$ and $p_c = p_g + 1$ on the left hand side of Figure 7.22 and confirms the findings of Section 5.3.1.

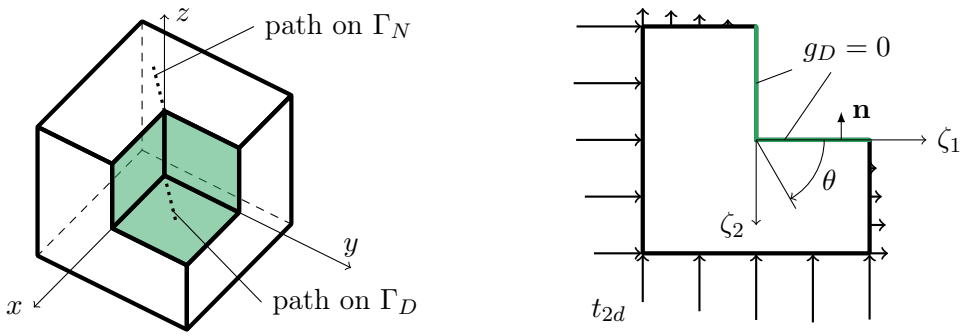

(a) Fichera Cube (b) L-shape

Figure 7.23: Geometry and boundary conditions of the Fichera cube example: (a) shape of the model where the dotted lines indicate the paths used for the comparison to the reference solution and (b) corresponding L-shape in two dimensions from which the non-zero Neumann boundary conditions are derived. In both cases, the Dirichlet boundary Γ_D is highlighted green.

7.2.4 Fichera Cube

A heat conduction problem is solved by the isogeometric Nyström method in order to verify its feasibility to perform local refinement. The admissibility factor of the local correction is set to $\eta = 6.0$ and $\epsilon_Q = 10^{-6}$ is the related tolerance of the numerical integration. The computational domain is determined by a unit cube subtracted from a larger one, i.e. $\Omega = (-1, 1)^3 - [0, 1]^3$, which is a three dimensional counterpart to a L-shape domain. The problem's geometry is illustrated in Figure 7.23(a). Homogeneous boundary conditions are applied at the Dirichlet boundary Γ_D, i.e. $g_D = 0$. The known Cauchy data along the Neumann boundary Γ_N are determined by an analytic solution of the L-shape domain in two dimensions, where the heat potential u_{2d} is given by

$$u_{2d} = r^{2/3} \sin\left(\frac{2\theta}{3}\right) \qquad \text{with} \qquad r = \sqrt{\zeta_1^2 + \zeta_2^2} \tag{7.10}$$

leading to the flux

$$t_{2d} = \mathbf{n}[i] \frac{\partial u_{2d}}{\partial \zeta_i} \qquad \text{with} \qquad i = 1, 2\,. \tag{7.11}$$

Here, ζ_i labels local coordinates of the L-shape and $\mathbf{n}$ denotes its unit outward normal vector, as depicted in Figure 7.23(b). The resulting flux t_{2d} is evaluated for each L-shape with respect to the xy-, yz- and the xz-plane. Their accumulation provides a smooth heat flux g_N on the Fichera cube which is enforced on Γ_N. The chosen boundary conditions lead to a singularity at the inverted corner. Hence, local h-refinement is preformed towards this singular point to approximate the unknown flux $t \in \Gamma_D$ accurately. Various grading steps are illustrated in Figure 7.24.

In order to verify the numerical analysis, the point-wise results of the isogeometric Nyström method are compared with a FEM solution computed with the Abaqus software package. The reference model has been adaptively refined and employs quadratic elements.

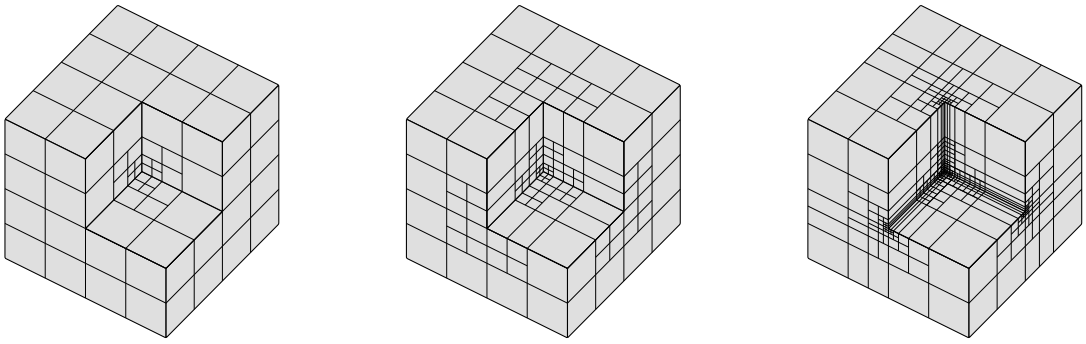

(a) 1st Refinement (b) 2nd Refinement (c) 3rd Refinement

Figure 7.24: Integration elements of the Fichera cube for different local h-refinements.

In particular, the results along two straight paths on Γ are evaluated: the variation of the heat potential u is evaluated along a line from $(0, 0, 1)$ to $(-0.5, -0.5, 1)$, whereas the heat flux t is compared along a line from $(0, 0, 0)$ to $(0.5, 0.5, 0)$. The paths are sketched in Figure 7.23(a) and the corresponding values are shown in Figure 7.25. The rise of the flux towards the singularity is slightly steeper in case of the isogeometric Nyström. On the whole, t as well as u demonstrate a very good agreement with the FEM solution.

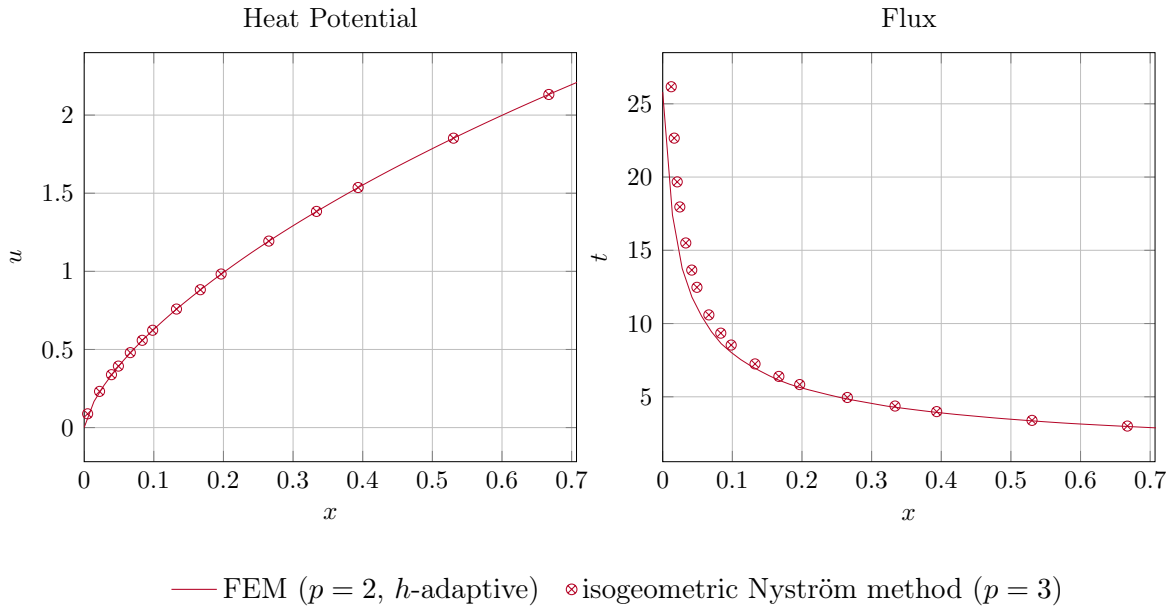

Figure 7.25: Variation of the heat potential u and heat flux t due to the finest discretization of the Fichera Cube example 7.24(c) compared with a FEM solution. The values are evaluated along the paths defined in Figure 7.23(a).

7.2.5 Spanner

The computational effort of the isogeometric Nyström method is examined. In particular, the impact of the admissibility factor for the local correction η is investigated. The analyzed

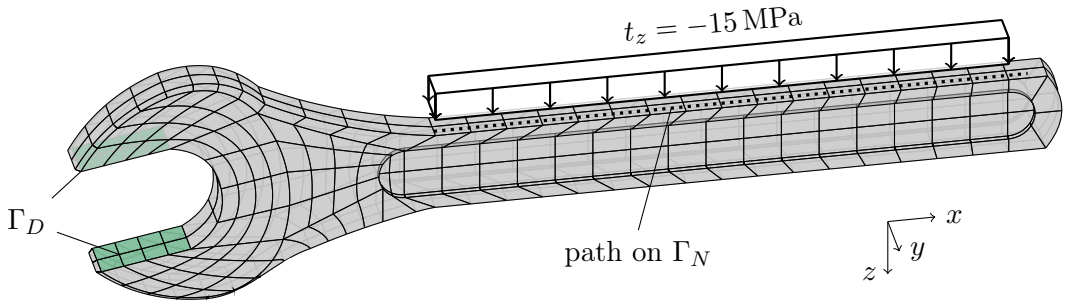

Figure 7.26: Boundary conditions of the spanner example. Black lines indicate the integration elements and the dotted line marks the path for the comparison to the reference solution. The Dirichlet boundary is highlighted in green.

model is a single-ended open-jaw spanner. Figure 7.26 illustrates the utilized partition of integration elements. Constant vertical loading is applied at the handle of the spanner and the displacements at the Dirichlet boundary Γ_D are fixed. The material properties are $\nu = 0.3$ and $E = 2.10 \times 10^5\,\mathrm{MPa}$. In the following, the local correction is performed with an integration accuracy of $\epsilon_Q = 10^{-6}$. Two different quadrature orders are applied $p_q = \{3, 4\}$ and various admissibility factor $\eta = \{1.0, \ldots, 10.0\}$ are used. The quality of the obtained results is indicated by means of the maximal displacement $|\mathbf{u}_{max}|$. The computational effort is expressed by the total number of kernel evaluations ($\#KE$) required to set up the system of equations. Note that it includes evaluations due to the local correction as well.

The resulting $|\mathbf{u}_{max}|$ and $\#KE$ are depicted in Figure 7.28. In addition, the deformation of the simulation with $p_q = 3$ and $\eta = 4.00$ is shown in Figure 7.27. The visualization uses the postprocessing strategy described in Section 4.2.5. In order to verify the numerical outcome, the results are compared with a FEM solution. To be precise, the vertical and horizontal deflection are measured along a straight line at the top of the handle, as indicated by the dotted path shown Figure 7.26. The values are compared in Figure 7.29.

The Nyström results are in excellent agreement with the FEM counterpart. However, the region subjected to local correction has to be sufficiently large. For the shown example this is the case for $\eta \geqslant 3$. At the same time, unnecessarily increasing of η yield to superfluous computational effort.

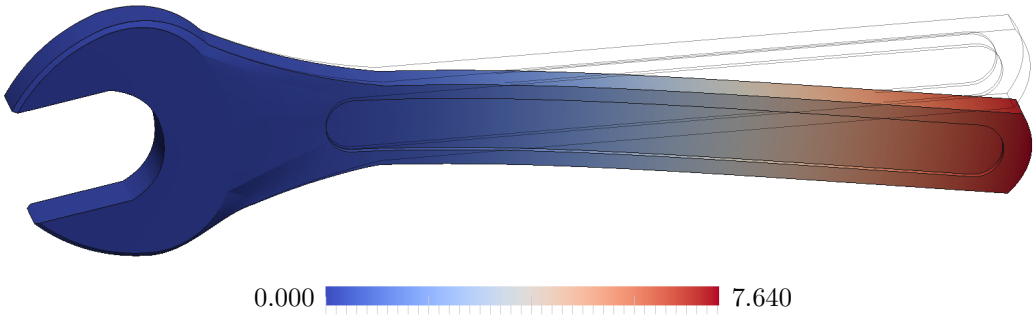

Figure 7.27: Deformation as a result of an isogeometric Nyström analysis with the degree $p_q = 3$ and the admissibility factor $\eta = 4.00$.

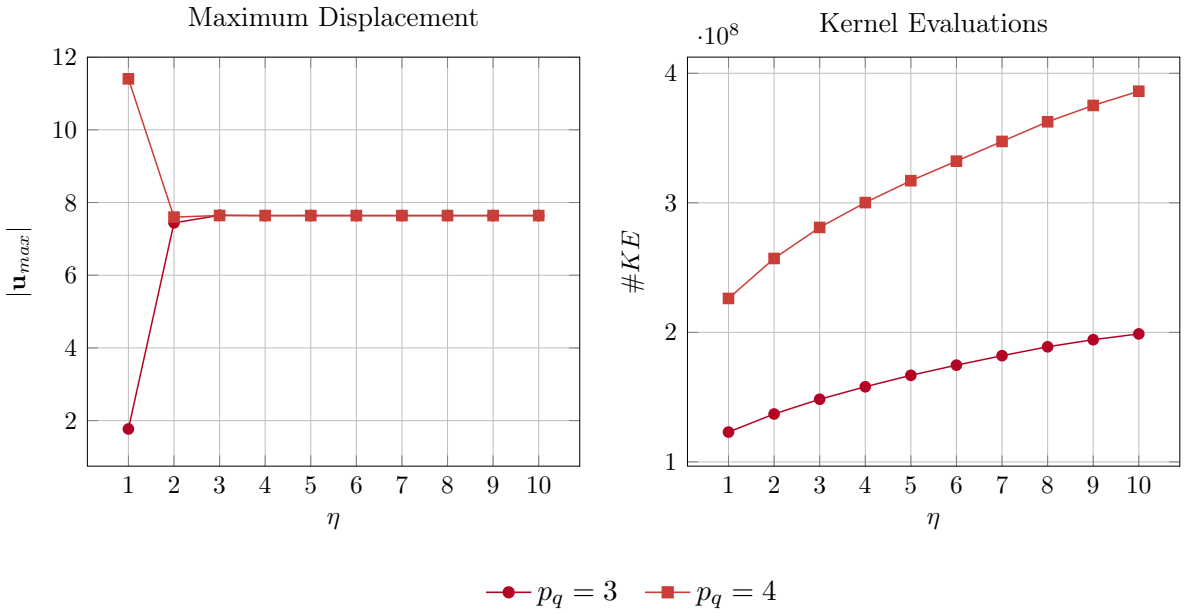

Figure 7.28: Maximal displacement $|\mathbf{u}_{max}|$ of the spanner and the corresponding numerical effort with respect to the admissibility factor for the local correction η. The numerical effort is measured by the total number of kernel evaluations ($\#KE$).

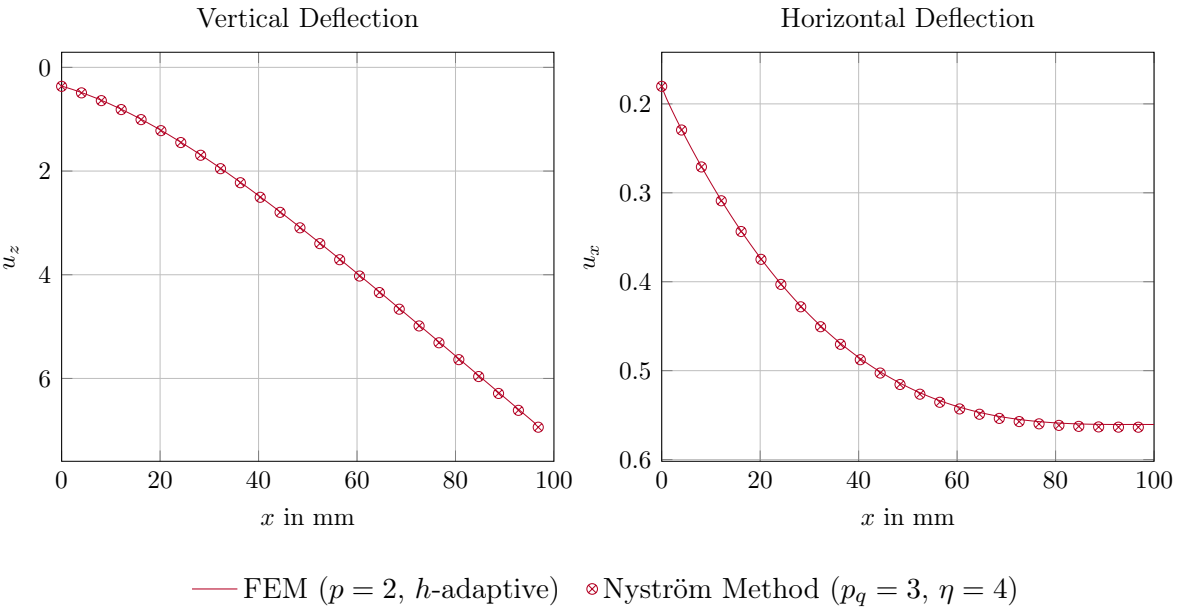

Figure 7.29: Vertical displacement u_z and horizontal displacement u_x in [mm] at the top of the spanner along the path depicted in Figure 7.26.

7.3 Trimmed Geometries

This section focuses on the integration of trimmed CAGD objects into an isogeometric BEM analysis using extended B-splines. The first example investigates the obtained approximation accuracy by studying a simple geometry represented by either regular or trimmed patches. Later, a trimmed CAGD model of a real-world object is eventually included into an isogeometric BEM simulation.

7.3.1 Trimmed Cube

In order to investigate the approximation quality of extended B-splines in the context of an isogeometric BEM analysis a unit cube is analyzed. The geometry is discretized by two different models as illustrated in Figure 7.30. One is described by 6 regular patches, whereas 4 trimmed patches are included in the other. Both represent the same geometry, i.e. $\ell_x = \ell_y = \ell_z = 1.0$, which defines the boundary Γ of an infinite domain. The boundary condition is given by

$$t(\boldsymbol{y}) = \mathsf{T}(\tilde{\boldsymbol{x}}, \boldsymbol{y}) \qquad \boldsymbol{y} \in \Gamma,\ \tilde{\boldsymbol{x}} \in \Omega^{-}. \tag{7.12}$$

In particular, a source point $\tilde{\boldsymbol{x}}$ in the center of the cube defines the boundary conditions for the exterior Neumann problem. The Laplace and Lamé-Navier equations are applied. The discretizations are set up for different degrees $p = \{1, 2, 3\}$ and knot insertion is applied to improve the solutions. The results are summarized in Figure 7.31 and Figure 7.32.

It can be observed from Figure 7.31 that the trimmed model yields essentially the same results as in the untrimmed one, for lower degree, i.e. $p = \{1, 2\}$. The graphs related to higher degree $p = 3$ demonstrate a similar converges behavior, yet with a noticeable offset in favor of the untrimmed discretization. This offset may occur due to the fact that the distance of the trimming curve to the inner knot span which provides the stable basis functions increases with the degree.

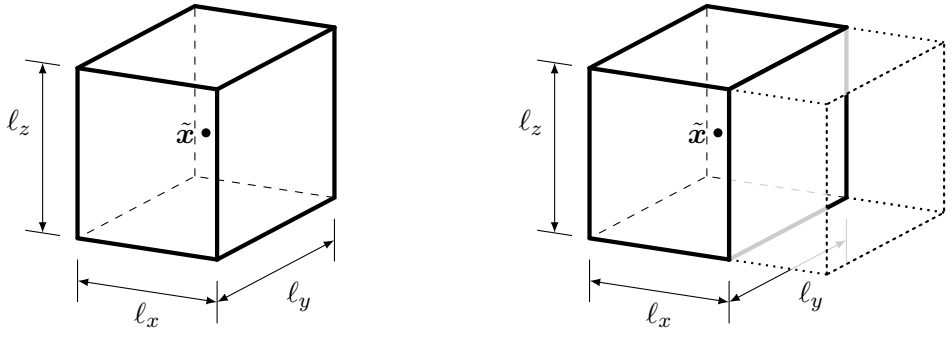

(a) Untrimmed (b) Trimmed

Figure 7.30: Discretization of a unit cube by (a) regular patches and (b) trimmed patches.

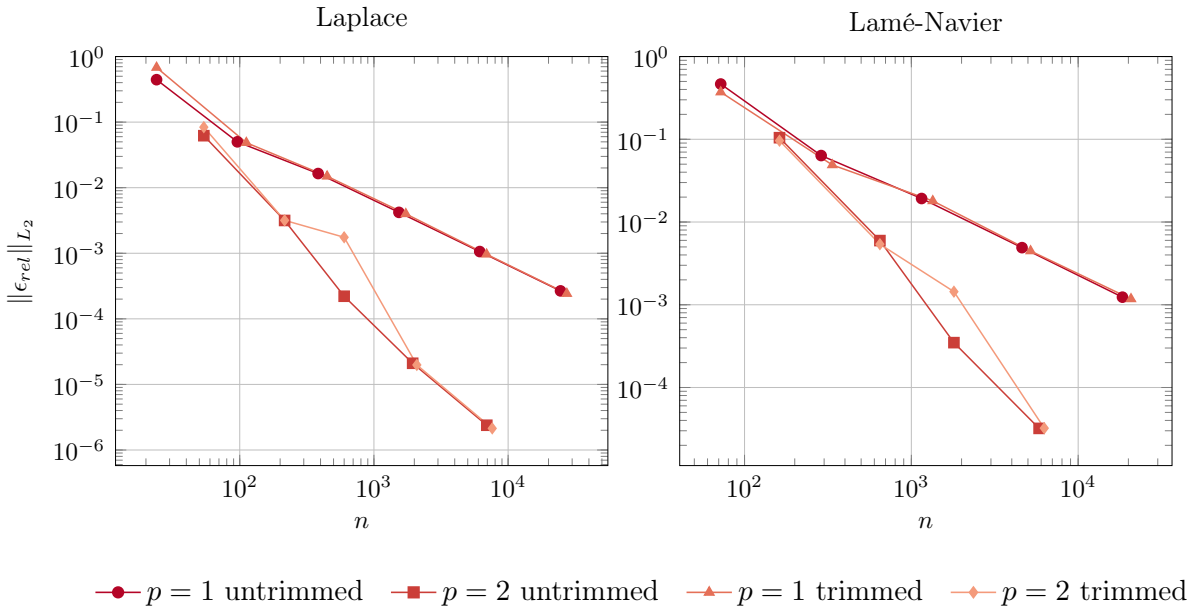

Figure 7.31: Relative L_2-error of an exterior Neumann problem on the (trimmed) cube example with respect to the number of degrees of freedom n.

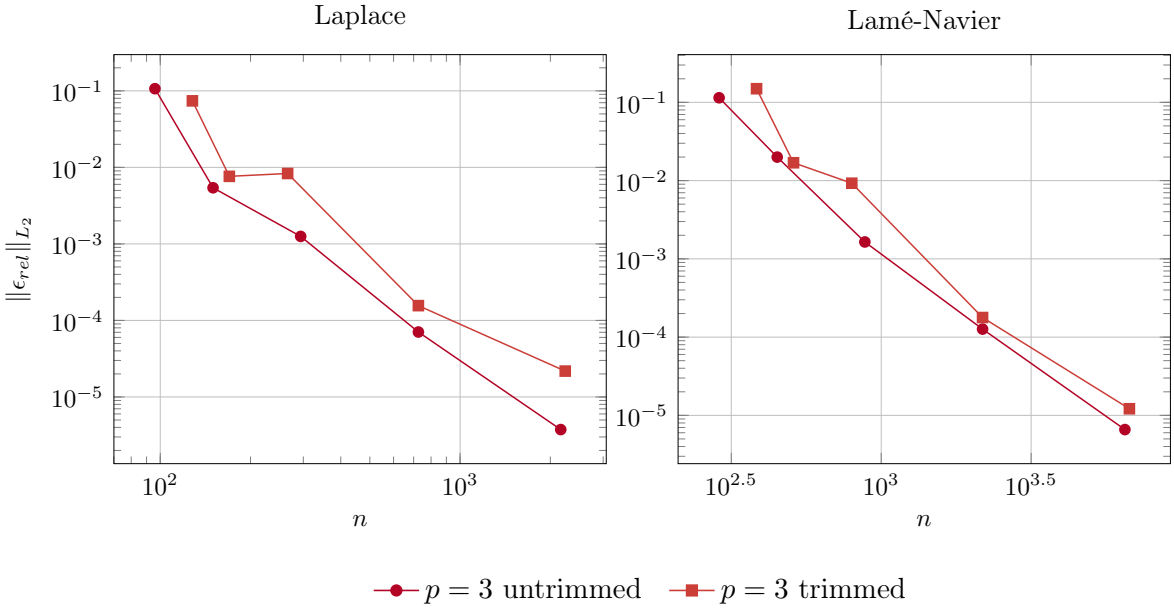

Figure 7.32: Relative L_2-error of an exterior Neumann problem on the (trimmed) cube example discretized with higher degree basis functions.

7.3.2 Tunnel Cross Passage

The excavation of a metro tunnel is analyzed. The geometry is specified by two parallel tunnel tubes which are connected by a cross passage as illustrated in Figure 7.33. The geometry model has been defined in Rhinoceros and is represented by several trimmed NURBS patches. The partition into integration elements at the trimmed regions is depicted in Figure 7.35. The soil property is determined by the Young's modulus $E = 313\,\text{MPa}$ and the Poisson ratio $\nu = 0.2$. The virgin stress field is given by $\sigma_{xx} = \sigma_{yy} = 1.38\,\text{MPa}$ and $\sigma_{zz} = 2.75\,\text{MPa}$. The resulting displacements are visualized in Figure 7.34. This real-world example verifies the capability of extended B-splines to deal with complex trimming cases.

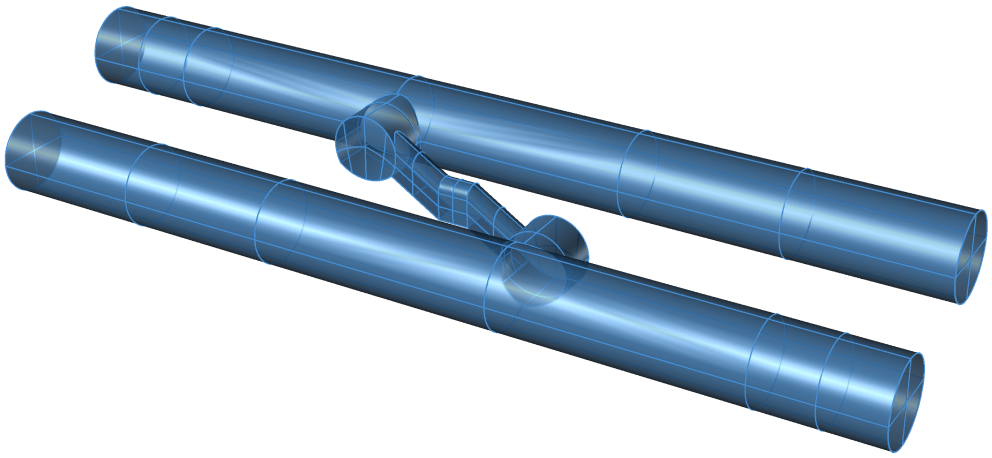

Figure 7.33: CAGD model of the tunnel example with trimmed NURBS patches.

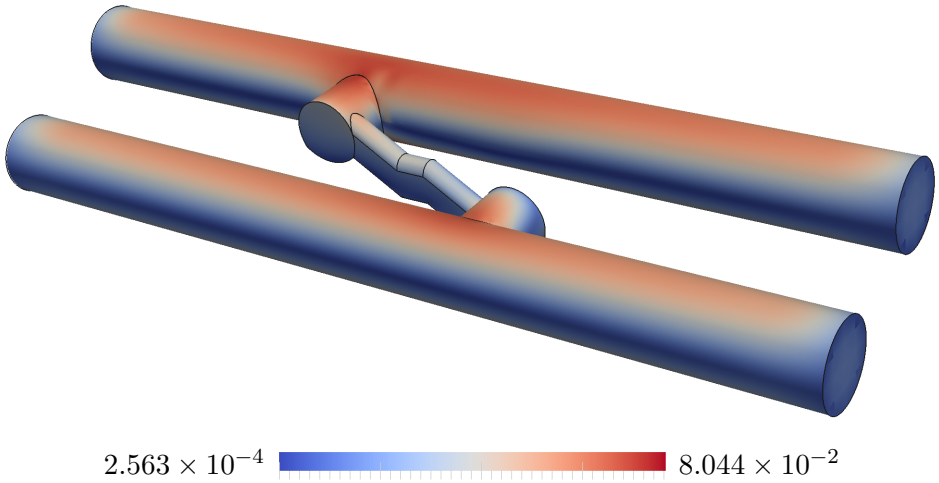

Figure 7.34: Resulting displacements of the tunnel example.

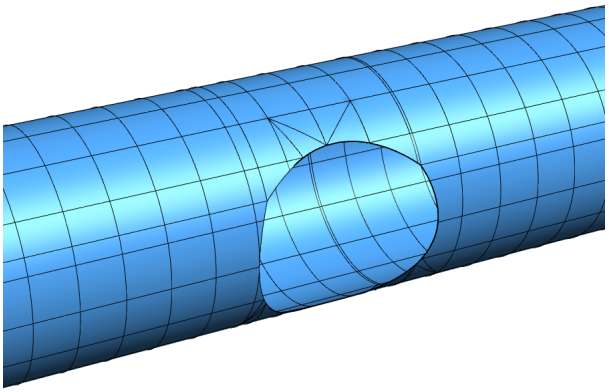

(a) Tunnel Tube

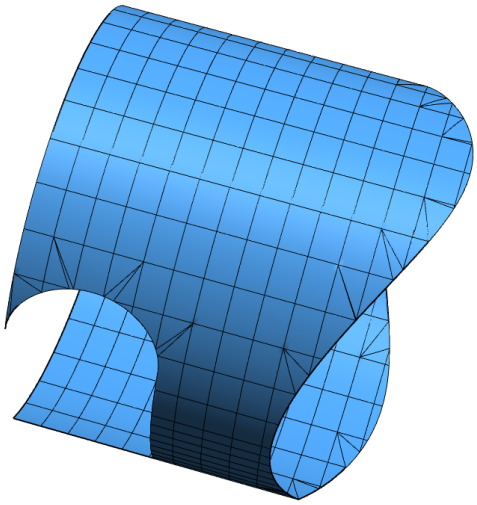

(b) Access Link

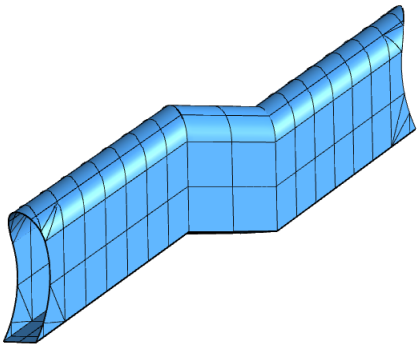

(c) Cross Passage

Figure 7.35: Discretizations of different tunnel parts. Black lines indicate the applied partition into integration elements.

8 Conclusion

In this dissertation, a seamless integration of NURBS based design models and numerical analysis is accomplished by employing boundary integral equations solved by either the Nyström or boundary element method. This includes the treatment of models with non-conforming patches and trimmed geometries. It has been demonstrated that the proposed methodology allows direct analysis of complex boundary representations without the need for mesh generation. Furthermore, the simulation methods benefit from the smoothness and accuracy of design models. In other words, isogeometric analysis and boundary integral equations complement each other extremely well. The main contributions of the presented work can be summarized as follows:

- Development of an *independent field approximation* paradigm which permits a separate approximation of integral operators.
- Application and implementation of *extended B-splines* for dealing with trimmed surfaces in an isogeometric BEM analysis.
- Formulation of a locally corrected *isogeometric Nyström method* and its application to the Laplace and Lamé-Navier equations.

Independent field approximation is a key aspect for a flexible BEM formulation, allowing mixed collocation along non-smooth boundaries, efficient evaluation of geometry values, reduction of computational effort and storage requirements. These advantages are obtained because refinement can be performed selectively and beyond, superfluous computations can be avoided. In addition, field variables can be represented by B-splines even if the geometry is described by NURBS. This capability has been utilized for the analysis of trimmed NURBS patches, where extended B-splines provide a stable basis with excellent approximation properties. Furthermore, these splines allow a straightforward definition of collocation point locations on trimmed patches and are easy to integrate into an existing isogeometric software. The concept of independent field approximation is pushed even further in the context of the Nyström method which represents field variables point-wise by means of a numerical quadrature. This discretization is not linked to basis functions defining the geometry and this has been exploited by performing local refinement of tensor product surfaces.

The convergence behavior of the implemented isogeometric BEM and Nyström method has been numerically investigated by various examples. On the one hand, the former exhibits optimal convergence in all cases. On the other hand, some convergence issues of the Nyström method have been revealed such as the impact of geometric corners and the linear convergence of the single layer operator. The most surprising observation is that the convergence of the double layer operator ceases at a certain h-refinement step in case of the Lamé-Navier equation. Nevertheless, the application of p-refinement is found to be a proper strategy for the cases investigated.

The obtained results provide a basis and thought-provoking impulse for future research directions. Independent field approximation may be beneficial in the context of a finite element analysis as well, especially the aspect of efficient geometry evaluation. In addition, it allows the analysis of design models without modifying them. The treatment of trimmed geometries by means of extended B-splines is a rather promising field and deserves to be explored in more detail. Its approximation properties for higher degrees and the combination with basis functions which allow local refinement are of particular interest. Regarding the representation of trimmed knot spans, the proposed approach may not be suitable for integration regions with a triangular topology if an evaluation at the degenerated edge of the local Coons patch is required. It has been demonstrated that the isogeometric Nyström method is capable of analyzing practical problems. Moreover, it has great potential since it is applicable in principle to any surface description which provides a valid geometrical mapping. Hence, the method can be easily adapted to forthcoming developments in CAGD. Hopefully, this motivates further mathematical analysis of the method to enhance its robustness. From a practical point of view, heuristic schemes should be developed to determine the admissibility factor for the local correction so that the integrals are accurately evaluated without superfluous computational effort.

This dissertation has neglected to address the issue of analyzing heterogeneous, time-dependent or non-linear problems. An extension of the proposed methodology to such cases would enhance its applicability to practical problems. On the design side, it has always been assumed that the analyzed solid is represented by a cohesive set of boundary surfaces. The treatment of additional geometrical details related to a boundary representation, like a manifold connecting to a solid, has not been considered.

In conclusion, the present thesis provides a methodology which allows a seamless integration of the most common design models of solids, i.e. trimmed NURBS geometries, into an analysis of linear potential and elasticity problems.

A Comparison of Greville and Demko Abscissae

A.1 Construction

Greville abscissae $\bar{r}^g$ are determined by knot averages of a knot vector Ξ according to equation (2.24). The total number of $\bar{r}^g$ is equal to the number of basis functions I. On the other hand, Demko abscissae $\bar{r}^d$ are defined by the extrema of Chebyshev splines related to Ξ. This splines oscillate constantly between their extrema which are alternately 1 and -1. In particular, a functions f of degree p given by $f(\bar{r}_i^d) = (-1)^{I-i}$ is represented by B-splines $B_{i,p}$ of $\Xi = \{r_0, \ldots, r_{I+p}\}$ such that it has max-norm 1 on $[r_0, r_{I+p}]$. The extrema of Chebyshev splines $\bar{r}^d$ are particularly suited for interpolation since they minimize the norm of the projection, similar to Chebyshev polynomials. The determination of the extrema involves the Newton-Raphson method and the Greville abscissae $\bar{r}^g$ provide a good initial guess for it. In Figure A.1, the starting point of the iterative process and the converged solution are compared for $\Xi = \{-1, -1, -1, -1, 0, 1, 1.5, 2, 2, 2, 2\}$. Note that the dashed curve related to $\bar{r}^g$ exceeds the value $|1|$, while the Chebyshev splines stays inside this bound.

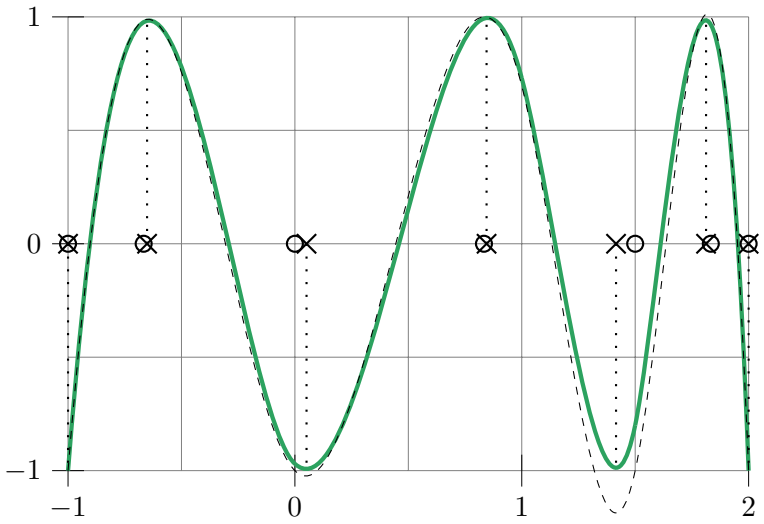

Figure A.1: Comparison of the interpolation of the oscillating function f according to Greville (dashed line, circles mark the points) and Demko abscissae (solid line, crosses mark the points).

A.2 Interpolation Quality

In the following, the interpolation property of the Demko and Greville approach are compared. In particular, three different parameter spaces with open knot vectors are investigated:

- Bézier: $\Xi = \{\dots, 0, 4, \dots\}$
- Uniform: $\Xi = \{\dots, 0, 1, 2, 3, 4, \dots\}$
- Graded: $\Xi = \{\dots, 0, 2, 3, 3.5, 4, \dots\}$

The interpolation quality of the different abscissae is determined by the norm of the inverse spline collocation matrix $\|\mathbf{A}_r^{-1}\|$. The results for various degrees $p = \{2, \dots, 9\}$ are summarized in Figure A.2.

Both approaches behave similar for moderate degrees, i.e. $p \leqslant 5$. For higher degrees the Demko abscissae leads to better results. In addition, the quality of the Greville interpolation dependents considerably on the arrangement of the interior knots. In contrast to the Demko approach which is not influenced by the knot spacing.

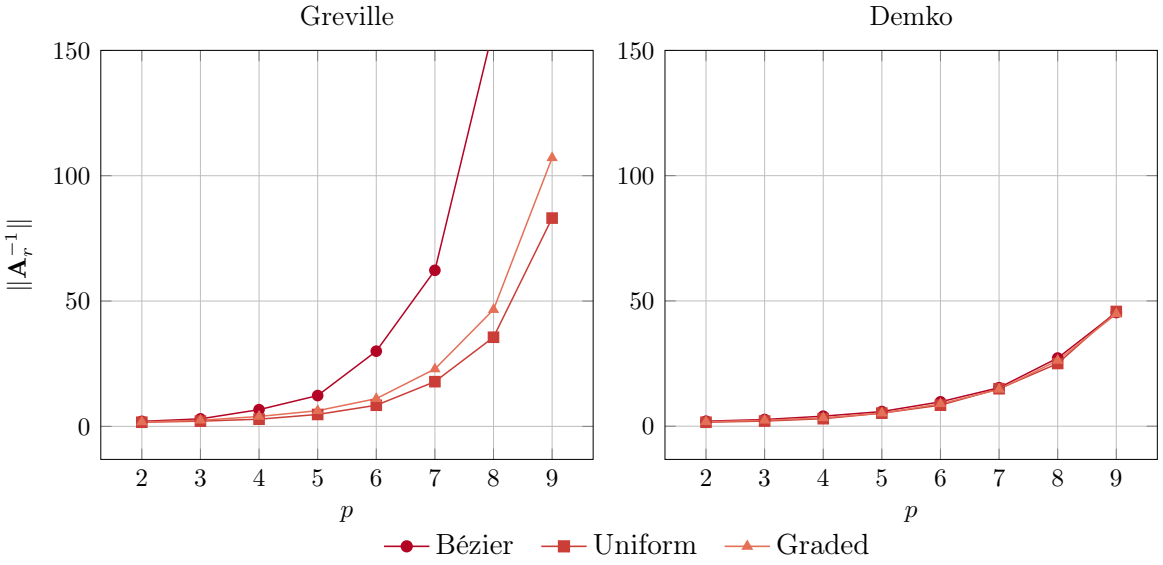

Figure A.2: Comparison of the spline interpolation matrix $\mathbf{A}_r$ according to Greville and Demko abscissae for different parameter spaces and degrees.

A.3 Collocation

The Laplace equation is solved for a Neumann problem using the isogeometric boundary element method. The geometry considered is a circle with a diameter smaller than 1. The system of equation is set up by collocation at either the Greville or Demko abscissae and the corresponding convergence for different degree $p = \{3, 4\}$ is depicted in Figure A.3. Note that not all discretizations of the Demko approach are shown. In particular, the graph related to the odd degree ends after a few refinement steps. The simulation has been stopped because two integration points got to close to each other, i.e. distance $\Delta \leqslant 10^{-7}$. In other words, an integration regions has become too small.

The parameter space and the related $\bar{r}^g$ and $\bar{r}^d$ of the canceled simulation are shown in Figure A.4. The problem occurs during the singular integration where elements τ are subdivided at the collocation point. Since some $\bar{r}^d$ are very close to knots, i.e. the boundary of τ, the subdivided elements may have a unfavorable ratio and one of them becomes very small. Using $\bar{r}^g$ results in anchors that are *on* the boundary of τ, thus, small integration regions are avoided.

It should, however, be emphasized that the issue is not the approximation quality of the Demko abscissa, but the numerical treatment of singular integrals.

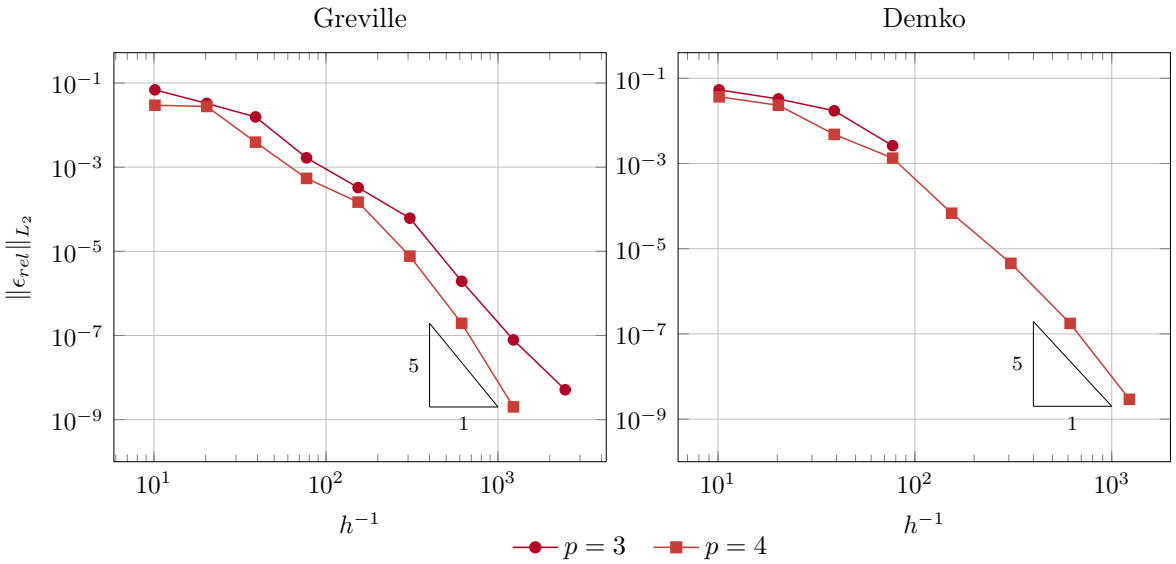

Figure A.3: Relative error of the circle example where the system of equation is set up by collocating at either the Greville or Demko abscissae.

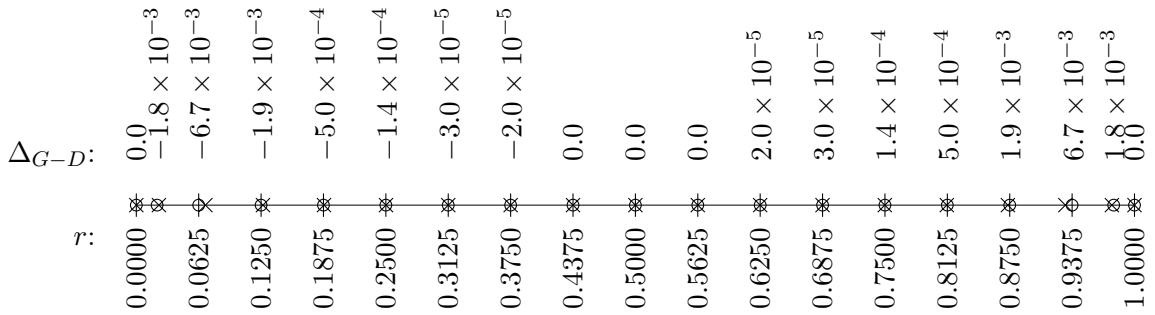

Figure A.4: Parametric space of the stopped simulation. The corresponding Greville abscissae are marked by circles, whereas crosses are used to indicate the Demko abscissae. The upper values indicate their difference Δ_{G-D}.

B Local Element Mapping

In case of the isogeometric Nyström method, local refinement can be performed even for tensor product surfaces. Here, the mapping from the initial element $\grave{\tau}_0$ defined by a tensor product of Λ_I and Λ_J to local elements $\grave{\tau}_\ell$ specified by refinement points $\grave{\boldsymbol{r}}_\ell$ is discussed. In a first step, each $\grave{\tau}_0$ is represented by means of its corner nodes, i.e. the knots of its corresponding knots span $\mathbf{s} = (s_1, s_2)^\intercal$. They are summarized in a *node matrix* $\mathbf{N}_0$ such that

$$\mathbf{N}_0 = \begin{pmatrix} \Lambda_I[s_1] & \Lambda_I[s_1+1] & \Lambda_I[s_1+1] & \Lambda_I[s_1] \\ \Lambda_J[s_2] & \Lambda_J[s_2] & \Lambda_J[s_2+1] & \Lambda_J[s_2+1] \\ 1 & 1 & 1 & 1 \end{pmatrix}. \tag{B.1}$$

The mapping from $\grave{\tau}_0$ to its $\grave{\tau}_{1,i}$ includes the translation and scaling of the corner nodes. They are assembled in a *transformation matrix* $\mathbf{T}_{1,i}$ which is defined for each $\grave{\tau}_{1,i}$ by

$$\mathbf{T}_{1,i} = \begin{pmatrix} l_{1,r_1}/l_{0,r_1} & 0 & t_{r_1} \\ 0 & l_{1,r_2}/l_{0,r_2} & t_{r_2} \\ 0 & 0 & 1 \end{pmatrix}. \tag{B.2}$$

The last column refers to the translation t of the first corner node, whereas the diagonal entries are related to the lengths of the initial (l_0) and refined element (l_1) in each parametric direction r. The construction of $\mathbf{T}_{1,i}$ due to a set of refinement points $\grave{\boldsymbol{r}}$ of the first level is summarized in Algorithm 1. Since the nodes of $\mathbf{N}_0$ are represented in homogeneous coordinates with $w = 1$, the transformation to the nodes $\mathbf{N}_{1,i}$ of local elements $\grave{\tau}_{1,i}$ can be expressed by a matrix product as

$$\grave{\tau}_{1,i} \coloneqq \mathbf{N}_{1,i} = \mathbf{T}_{1,i}\, \mathbf{N}_0. \tag{B.3}$$

If there are refinement points $\grave{\boldsymbol{r}}_\ell$ of a higher level, i.e. $\ell > 1$, within a local element $\grave{\tau}_{1,i}$ additional transformation matrices $\mathbf{T}_{2,i}$ are constructed based on $\mathbf{N}_{1,i}$ and $\grave{\boldsymbol{r}}_\ell$. The resulting local elements $\grave{\tau}_{2,i}$ are given by

$$\grave{\tau}_{2,i} \coloneqq \mathbf{N}_{2,i} = \mathbf{T}_{2,i}\, \mathbf{N}_{1,j} = \mathbf{T}_{2,i}\, \mathbf{T}_{1,j}\, \mathbf{N}_0. \tag{B.4}$$

The accumulated transformation matrices $\hat{\mathbf{T}}_{\ell,i}$ relate the final $\grave{\tau}_{\ell,i}$ due to all refinement levels to the initial knot span $\mathbf{N}_0$.

$$\grave{\tau}_{\ell,i} \coloneqq \mathbf{N}_{\ell,i} = \hat{\mathbf{T}}_{\ell,i}\, \mathbf{N}_0 \qquad \text{with} \qquad \hat{\mathbf{T}}_{\ell,i} = \prod_{k \in L} \mathbf{T}_{k,m} \tag{B.5}$$

where L denotes an index-set of all levels defining $\grave{\tau}_{\ell,i}$ which is ordered decreasingly. The set up of $\hat{\mathbf{T}}_{\ell,i}$ is described in Algorithm 2.

Algorithm 1 Set up transformation matrices for the next level

Require: Node matrix $\mathbf{N}$ and related refinement points $\grave{\boldsymbol{r}}$ of the subsequent level ℓ

$l_{r_1} = \mathbf{N}[1,3] - \mathbf{N}[1,1]$
$l_{r_2} = \mathbf{N}[2,3] - \mathbf{N}[2,1]$
initialize temporary knot vectors Λ_I and Λ_J
$\Lambda_I \leftarrow \mathbf{N}[1,k], k = 1,3$
$\Lambda_J \leftarrow \mathbf{N}[2,k], k = 1,3$
for all $\grave{\boldsymbol{r}}$ **do**
    $\Lambda_I \leftarrow \grave{\boldsymbol{r}}_i[1]$
    $\Lambda_J \leftarrow \grave{\boldsymbol{r}}_i[2]$
l_I = length of each non-zero knot spans of Λ_I
l_J = length of each non-zero knot spans of Λ_J
initialize array $\mathbf{a}_T$ for transformation matrices $\mathbf{T}$
$t_{r_2} = 0$
for all $l_j \in l_J$ **do**
    $t_{r_1} = 0$
    for all $l_i \in l_I$ **do**
        $\mathbf{T} = \mathrm{diag}(l_i/l_{r_1}, l_j/l_{r_2}, 1)$
        $\mathbf{T}[1,3] = \mathbf{N}[1,1]\,(1 - l_i/l_{r_1}) + t_{r_1}$
        $\mathbf{T}[2,3] = \mathbf{N}[2,1]\,(1 - l_j/l_{r_2}) + t_{r_2}$
        $\mathbf{a}_T \leftarrow \mathbf{T}$
        $t_{r_1} = t_{r_1} + l_i$
    $t_{r_2} = t_{r_2} + l_j$
return $\mathbf{a}_T$

Algorithm 2 Hierarchical refinement

Require: Node matrix $\mathbf{N}_0$ of an element $\tilde{\tau}$ and refinement points $\grave{\boldsymbol{r}}$ of all levels

initialize array $\mathbf{a}_T$ for transformation matrices $\hat{\mathbf{T}}_\ell \in \mathbb{R}^{3\times3}$
$\mathbf{a}_T \leftarrow \mathbf{T}_0 = \mathrm{diag}\,(1,1,1)$
for all refinement levels ℓ **do**
  initialize temporary array $\mathbf{b}_T$ for $\mathbf{T}_\ell$
  for all $\mathbf{T}_{\ell-1,k} \in \mathbf{a}_T$ **do** ▷ loop over all computed local elements $\grave{\tau}_{\ell-1}$
    $\mathbf{N}_{\ell-1,k} = \mathbf{T}_{\ell-1,k}\mathbf{N}_0$
    initialize temporary array $\mathbf{c}_{\grave{\boldsymbol{r}}}$ for refinement points
    for all $\grave{\boldsymbol{r}}_{\ell,m} \in \grave{\boldsymbol{r}}_\ell$ **do**
      if $\grave{\boldsymbol{r}}_{\ell,m}$ is inside $\grave{\tau}_{\ell-1,k}$ related to $\mathbf{N}_{\ell-1,k}$ **then**
        $\mathbf{c}_{\grave{\boldsymbol{r}}} \leftarrow \grave{\boldsymbol{r}}_{\ell,m}$
    if $\mathbf{c}_{\grave{\boldsymbol{r}}} = \emptyset$ **then**
      $\mathbf{b}_t \leftarrow \mathbf{T}_{\ell-1,k}$
    else
      $\mathbf{c}_T$ = array of $\mathbf{T}_\ell$ set up by Algorithm 1 with $\mathbf{N}_{\ell-1,k}$ and $\mathbf{c}_{\grave{\boldsymbol{r}}}$
      for all $\mathbf{T}_{\ell,r} \in \mathbf{c}_T$ **do**
        $\mathbf{b}_T \leftarrow \mathbf{T}_{\ell,r}\,\mathbf{T}_{\ell-1,k}$
  $\mathbf{a}_T = \mathbf{b}_T$
return $\mathbf{a}_T$

C Evaluation of Extrapolation Weights

C.1 Explicit Representation

The coefficients β_k of the polynomial $\psi_{j,p}$ are computed by equation (6.9). In particular, $\mathbb{T}_{k,l}$ is required which represents all k-combinations with repetition of the knots $\{r_{j+1}, \ldots, r_{j+p}\}$. For example $\mathbb{T}_{k,l}$ in case of a cubic B-spline, i.e. $p = 3$, would be given by

$$\begin{aligned} \mathbb{T}_{3,1} &= \{r_{j+1}, r_{j+2}, r_{j+3}\}, & \mathbb{T}_{2,1} &= \{r_{j+1}, r_{j+2}\}, & \mathbb{T}_{1,1} &= \{r_{j+1}\}, \\ & & \mathbb{T}_{2,2} &= \{r_{j+2}, r_{j+3}\}, & \mathbb{T}_{1,2} &= \{r_{j+2}\}, \\ & & \mathbb{T}_{2,3} &= \{r_{j+1}, r_{j+3}\}, & \mathbb{T}_{1,3} &= \{r_{j+3}\}. \end{aligned}$$

The power basis form (6.11) of the polynomial segments $\mathcal{B}_i^s$ is obtained by

$$\mathcal{B}_i^s(r) = \sum_{m=0}^{p} \alpha_m \left(r - \tilde{r}\right)^m = \tilde{\alpha}_0 1 + \tilde{\alpha}_1 r + \cdots + \tilde{\alpha}_p r^p \tag{C.1}$$

where $\tilde{\alpha}_m$ is for $p = 1$:

$$\begin{aligned} \tilde{\alpha}_0 &= 1\alpha_0 + 1\alpha_1 \left(-\tilde{r}\right), \\ \tilde{\alpha}_1 &= 1\alpha_1, \end{aligned}$$

for p= 2:

$$\begin{aligned} \tilde{\alpha}_0 &= 1\alpha_0 + 1\alpha_1 \left(-\tilde{r}\right) + 1\alpha_2 \left(-\tilde{r}\right)^2, \\ \tilde{\alpha}_1 &= 1\alpha_1 + 2\alpha_2 \left(-\tilde{r}\right), \\ \tilde{\alpha}_2 &= 1\alpha_2, \end{aligned}$$

for p= 3:

$$\begin{aligned} \tilde{\alpha}_0 &= 1\alpha_0 + 1\alpha_1 \left(-\tilde{r}\right) + 1\alpha_2 \left(-\tilde{r}\right)^2 + 1\alpha_3 \left(-\tilde{r}\right)^3, \\ \tilde{\alpha}_1 &= 1\alpha_1 + 2\alpha_2 \left(-\tilde{r}\right) + 3\alpha_3 \left(-\tilde{r}\right)^2, \\ \tilde{\alpha}_2 &= 1\alpha_2 + 3\alpha_3 \left(-\tilde{r}\right), \\ \tilde{\alpha}_3 &= 1\alpha_3 . \end{aligned}$$

It should be noted that the values in front of the coefficients α correspond to Pascals triangle, which yields to the binomial coefficient in equation (6.11). In general, if the coordinate r does not contribute to the derivative of a power basis form, e.g. $r = 0$, its evaluation simplifies to

$$\mathcal{B}_i^{s^{(k)}}(0) = k!\, \tilde{\alpha}_k \tag{C.2}$$

which has been utilized to obtain equation (6.13).

C.2 Example

The example shown in Figure 6.1 is considered to clarify the computation of extrapolation weights $e_{i,j}$. The knot vector is given by $\Xi = \{1,1,1,2,3,4,4,4\}$, the first B-spline is degenerated, i.e. $\mathbb{J} = \{0\}$, and the knot span $s = 3$ is the closest non-trimmed interval. Hence, the polynomial $\psi_{0,2}$ is determined by the knot values $\{1,1\}$ and the correspond coefficients are $\beta_k = \{1,-2,1\}$. The polynomial segments $\mathcal{B}_i^s$ obtained by equation (6.11) are given by

$$\mathcal{B}_1^3 = 0.5\,r^2 - 3\,r + 4.5, \tag{C.3}$$
$$\mathcal{B}_2^3 = -1\,r^2 + 5\,r - 5.5, \tag{C.4}$$
$$\mathcal{B}_3^3 = 0.5\,r^2 - 2\,r + 2\,. \tag{C.5}$$

The extrapolation weights are computed by different approaches: firstly, the extrapolation weights are obtained by means of spline interpolation. Next, the functional (6.7) is evaluated directly by applying Horner's method to the explicit representations (6.11) and (6.8). Finally, the simplified functional (6.13) is used.

Spline Interpolation The anchors are chosen to be $\bar{r} = \{1, 1.5, 2\}$ leading to the spline collocation matrix $\mathbf{A}_r$ and the right hand side $\mathbf{f}_i$ for each (C.3) – (C.5):

$$\mathbf{A}_r = \begin{pmatrix} 1 & 0 & 0 \\ 0.25 & 0.625 & 0.125 \\ 0 & 0.5 & 0.5 \end{pmatrix}, \quad \mathbf{f}_1 = \begin{pmatrix} 2 \\ 1.125 \\ 0.5 \end{pmatrix}, \quad \mathbf{f}_2 = \begin{pmatrix} -1.5 \\ -0.25 \\ 0.5 \end{pmatrix}, \quad \mathbf{f}_3 = \begin{pmatrix} 0.5 \\ 0.125 \\ 0 \end{pmatrix}.$$

Solving the system of equations gives

$$\mathbf{M} = \begin{pmatrix} e_{1,0} & e_{1,1} & e_{1,2} \\ e_{2,0} & e_{2,1} & e_{2,2} \\ e_{3,0} & e_{3,1} & e_{3,2} \end{pmatrix} = \begin{pmatrix} 2 & 1 & 0 \\ -1.5 & 0 & 1 \\ 0.5 & 0 & 0 \end{pmatrix}$$

where the rows correspond to (C.3) – (C.5) and the first column provides the sought extrapolation weights $e_{i,j}$ for $\mathbb{J} = \{0\}$.

Direct Evaluation of the Functional The explicit representation of $\psi_{j,p}$ can be evaluated by Horner's method for higher derivatives [84]. The procedure is summarized in Algorithm 3, which returns all values $\psi_{j,p}^{(m)}$, $m = \{0,\ldots,p\}$, collected in a vector $\mathbf{v}^{\psi}$. The same procedure can be applied to the explicit representation of $\mathcal{B}_i^s$, if β_k is substituted by $\tilde{\alpha}_k$. For the given example the position of the evaluation points is chosen to be $\mu_j = 1$ which leads to the following values

$$\mathbf{v}_1^{\mathcal{B}} = \begin{pmatrix} 2 \\ -2 \\ 1 \end{pmatrix}, \qquad \mathbf{v}_2^{\mathcal{B}} = \begin{pmatrix} -1.5 \\ 3 \\ -2 \end{pmatrix}, \qquad \mathbf{v}_3^{\mathcal{B}} = \begin{pmatrix} 0.5 \\ -1 \\ 1 \end{pmatrix} \qquad \text{and} \qquad \mathbf{v}^{\psi} = \begin{pmatrix} 0 \\ 0 \\ 2 \end{pmatrix}.$$

Applying these values to (6.7) provides the extrapolation weights

$$e_{1,0} = \frac{1}{2}\,[2 \cdot 2] = 2, \qquad e_{2,0} = \frac{1}{2}\,[2 \cdot (-1.5)] = -1.5, \qquad e_{3,0} = \frac{1}{2}\,[2 \cdot 0.5] = 0.5\,.$$

Algorithm 3 Horner's method for higher derivatives

Require: polynomial coefficients β_k of $\psi_{j,p}$ and the coordinate μ_j
1: initialize matrix $\mathbf{M} \in \mathbb{R}^{p+2 \times p+1}$
2: **for** $k = 0$ **to** p **do**
3: $\quad \mathbf{M}_{0,k} = \beta_k$
4: **for** $m = 0$ **to** p **do** $\quad \triangleright$ compute Horner coefficients
5: $\quad \mathbf{M}_{m+1,p} = \mathbf{M}_{m,p}$
6: $\quad n = p - 1$
7: $\quad$ **while** $n \geq m$ **do**
8: $\quad\quad \mathbf{M}_{m+1,n} = \mu_j\, \mathbf{M}_{m+1,n+1} + \mathbf{M}_{m,n}$
9: $\quad\quad n = n - 1$
10: initialize vector $\mathbf{v}^{\psi} \in \mathbb{R}^{p+1}$
11: **for** $m = 0$ **to** p **do** $\quad \triangleright$ compute derivatives
12: $\quad \mathbf{v}^{\psi}_{m} = m!\, \mathbf{M}_{m+1,m}$
13: **return** $\mathbf{v}^{\psi}$

Indirect Evaluation of the Functional For the given example the coefficients $\psi^{(p-k)}_{j,p} = (p-k)!\,\beta_{p-k}$ and $\mathcal{B}^{s^{(k)}}_{i} = k!\,\tilde{\alpha}_k$ of equation (6.13) are

$$\psi_{0,2} = 1 \cdot 1, \qquad \psi^{(1)}_{0,2} = 1 \cdot (-2), \qquad \psi^{(2)}_{0,2} = 2 \cdot 1,$$

respectively

$$\begin{aligned}
\mathcal{B}^{3}_{1} &= 1 \cdot 4.5, & \mathcal{B}^{3^{(1)}}_{1} &= 1 \cdot (-3), & \mathcal{B}^{3^{(2)}}_{1} &= 2 \cdot 0.5,\\
\mathcal{B}^{3}_{2} &= 1 \cdot (-5.5), & \mathcal{B}^{3^{(1)}}_{2} &= 1 \cdot 5, & \mathcal{B}^{3^{(2)}}_{2} &= 2 \cdot (-1),\\
\mathcal{B}^{3}_{3} &= 1 \cdot 2, & \mathcal{B}^{3^{(1)}}_{3} &= 1 \cdot (-2), & \mathcal{B}^{3^{(2)}}_{3} &= 2 \cdot 0.5\,.
\end{aligned}$$

Hence, the extrapolation weights are computed by

$$\begin{aligned}
e_{1,0} &= \frac{1}{2}\,[2 \cdot 4.5 - (-2) \cdot (-3) + 1 \cdot 1] = 2,\\
e_{2,0} &= \frac{1}{2}\,[2 \cdot (-5.5) - (-2) \cdot 5 + 1 \cdot (-2)] = -1.5,\\
e_{3,0} &= \frac{1}{2}\,[2 \cdot 2 - (-2) \cdot (-2) + 1 \cdot 1] = 0.5\,.
\end{aligned}$$

Bibliography

[1] Anselone, P.M. Singularity subtraction in the numerical solution of integral equations, *ANZIAM Journal*, 22:408–418, 1981.

[2] Arnold, D.N.; Saranen, J. On the asymptotic convergence of spline collocation methods for partial differential equations, *SIAM Journal on Numerical Analysis*, 21(3): 459–472, 1984.

[3] Arnold, D.N.; Wendland, W.L. On the asymptotic convergence of collocation methods, *Mathematics of Computation*, 41(164):349–381, 1983.

[4] Arnold, D.N.; Wendland, W.L. The convergence of spline collocation for strongly elliptic equations on curves, *Numerische Mathematik*, 47(3):317–341, 1985.

[5] Atkinson, K.E. *The Numerical Solution of Integral Equations of the Second Kind.* Cambridge University Press, 1997.

[6] Auricchio, F.; Beirão Da Veiga, L.; Hughes, T.J.R.; Reali, A.; Sangalli, G. Isogeometric collocation methods, *Mathematical Models and Methods in Applied Sciences*, 20(11):2075–2107, 2010.

[7] Bazilevs, Y.; Calo, V.M.; Cottrell, J.; Evans, J.A.; Hughes, T.J.R.; Lipton, S.; Scott, M.A.; Sederberg, T.W. Isogeometric analysis using T-splines, *Computer Methods in Applied Mechanics and Engineering*, 199(5-8):229–263, 2010.

[8] Beer, G. Mapped infinite patches for the NURBS based boundary element analysis in geomechanics, *Computers and Geotechnics*, 66:66–74, 2015.

[9] Beer, G.; Marussig, B. Boundary element methods. In: Beer, G.; Bordas, S., editors, *Isogeometric Methods for Numerical Simulation*, volume 561 of *CISM International Centre for Mechanical Sciences*, pages 121–172, Springer, 2015.

[10] Beer, G.; Marussig, B.; Duenser, C. Isogeometric boundary element method for the simulation of underground excavations, *Géotechnique Letters*, 3:108–111, 2013.

[11] Beer, G.; Marussig, B.; Zechner, J.; Duenser, C.; Fries, T.-P. Boundary element analysis with trimmed NURBS and a generalized IGA approach. In: *11th World Congress on Computational Mechanics, WCCM 2014, 5th European Conference on Computational Mechanics, ECCM 2014 and 6th European Conference on Computational Fluid Dynamics, ECFD 2014*, pages 2445–2456, 2014.

[12] Beer, G.; Marussig, B.; Zechner, J. A simple approach to the numerical simulation with trimmed CAD surfaces, *Computer Methods in Applied Mechanics and Engineering*, 285:776–790, 2015.

[13] Beer, G. *Advanced Numerical Simulation Methods: From CAD Data Directly to Simulation Results*. CRC Press, Leiden, 2015.

[14] Beer, G.; Smith, I.M.; Duenser, C. *The Boundary Element Method with Programming*. Springer Wien - New York, 2008.

[15] Benson, D.J.; Bazilevs, Y.; Hsu, M.C.; Hughes, T.J.R. Isogeometric shell analysis: The Reissner–Mindlin shell, *Computer Methods in Applied Mechanics and Engineering*, 199(5–8):276–289, 2010.

[16] de Boor, C. *A practical guide to splines*, volume 27 of *Applied Mathematical Sciences*. Springer, New York, 2001.

[17] Börm, S.; Grasedyck, L. HLib – a library for $\mathcal{H}$- and $\mathcal{H}^2$-matrices, 1999. URL `http://www.hlib.org`.

[18] Breitenberger, M.; Apostolatos, A.; Philipp, B.; Wüchner, R.; Bletzinger, K.-U. Analysis in computer aided design: Nonlinear isogeometric B-Rep analysis of shell structures, *Computer Methods in Applied Mechanics and Engineering*, 284:401–457, 2015.

[19] Bremer, J.; Gimbutas, Z.; Rokhlin, V. A nonlinear optimization procedure for generalized gaussian quadratures, *SIAM Journal on Scientific Computing*, 32(4):1761–1788, 2010.

[20] Bremer, J. On the Nyström discretization of integral equations on planar curves with corners, *Applied and Computational Harmonic Analysis*, 32(1):45–64, 2012.

[21] Bremer, J.; Gimbutas, Z. A Nyström method for weakly singular integral operators on surfaces, *Journal of Computational Physics*, 231(14):4885–4903, 2012.

[22] Bremer, J.; Rokhlin, V. Efficient discretization of laplace boundary integral equations on polygonal domains, *Journal of Computational Physics*, 229(7):2507–2525, 2010.

[23] Bremer, J.; Gillman, A.; Martinsson, P.-G. A high-order accurate accelerated direct solver for acoustic scattering from surfaces, *BIT Numerical Mathematics*, 55(2):367–397, 2015.

[24] Bruno, O.P.; Kunyansky, L.A. A fast, high-order algorithm for the solution of surface scattering problems: Basic implementation, tests, and applications, *Journal of Computational Physics*, 169(1):80–110, 2001.

[25] Bruno, O.P.; Ovall, J.S.; Turc, C. A high-order integral algorithm for highly singular PDE solutions in Lipschitz domains, *Computing*, 84(3-4):149–181, 2009.

[26] Cabral, J.J.S.P.; Wrobel, L.C.; Brebbia, C.A. A BEM formulation using B-splines: I- uniform blending functions, *Engineering Analysis with Boundary Elements*, 7(3): 136–144, 1990.

[27] Cabral, J.J.S.P.; Wrobel, L.C.; Brebbia, C.A. A BEM formulation using B-splines: II- multiple knots and nonuniform blending functions, *Engineering Analysis with Boundary Elements*, 8(1):51–55, 1991.

[28] Canino, L.F.; Ottusch, J.J.; Stalzer, M.A.; Visher, J.L.; Wandzura, S.M. Numerical solution of the Helmholtz equation in 2D and 3D using a high-order Nyström discretization, *Journal of Computational Physics*, 146(2):627–663, 1998.

[29] Catmull, E.; Clark, J. Recursively generated B-spline surfaces on arbitrary topological meshes, *Computer-Aided Design*, 10(6):350–355, 1978.

[30] Cheng, A.H.-D.; Cheng, D.T. Heritage and early history of the boundary element method, *Engineering Analysis with Boundary Elements*, 29(3):268–302, 2005.

[31] Cheng, R.S.-C. Some numerical results using the modified Nyström method to solve the 2-D potential problem, *Engineering Analysis with Boundary Elements*, 14(4): 335–342, 1994.

[32] Cirak, F.; Long, Q. Subdivision shells with exact boundary control and non-manifold geometry, *International Journal for Numerical Methods in Engineering*, 88(9):897–923, 2011.

[33] Costabel, M.; McLean, W. Spline collocation for strongly elliptic equations on the torus, *Numerische Mathematik*, 62(4):511–538, 1992.

[34] Costabel, M.; Stephan, E.P. On the convergence of collocation methods for boundary integral equations on polygons, *Mathematics of Computation*, 49(180):461–478, October 1987.

[35] Cottrell, J.A.; Reali, A.; Bazilevs, Y.; Hughes, T.J.R. Isogeometric analysis of structural vibrations, *Computer Methods in Applied Mechanics and Engineering*, 195(41-43):5257–5296, 2006.

[36] Cottrell, J.A.; Hughes, T.J.R.; Reali, A. Studies of refinement and continuity in isogeometric structural analysis, *Computer Methods in Applied Mechanics and Engineering*, 196(41–44):4160 – 4183, 2007.

[37] Cottrell, J.A.; Hughes, T.J.R.; Bazilevs, Y. *Isogeometric Analysis: Toward Integration of CAD and FEA*. John Wiley & Sons, Chichester, England, 2009.

[38] Demko, S. On the existence of interpolating projections onto spline spaces, *Journal of Approximation Theory*, 43(2):151–156, 1985.

[39] Dokken, T.; Lyche, T.; Pettersen, K.F. Polynomial splines over locally refined box-partitions, *Computer Aided Geometric Design*, 30(3):331–356, 2013.

[40] Doo, D.; Sabin, M. Behaviour of recursive division surfaces near extraordinary points, *Computer-Aided Design*, 10(6):356–360, 1978.

[41] Dornisch, W.; Klinkel, S.; Simeon, B. Isogeometric Reissner–Mindlin shell analysis with exactly calculated director vectors, *Computer Methods in Applied Mechanics and Engineering*, 253:491–504, 2013.

[42] Duffy, M.G. Quadrature over a pyramid or cube of integrands with a singularity at a vertex, *SIAM Journal on Numerical Analysis*, 19(6):1260–1262, 1982.

[43] Englund, J. A Nyström scheme with rational quadrature applied to edge crack problems, *Communications in Numerical Methods in Engineering*, 23(10):945–960, 2007.

[44] Farin, G. *Curves and Surfaces for CAGD: A Practical Guide*. Morgan Kaufmann, San Francisco, Calif., 5 edition, 2002.

[45] Feischl, M.; Gantner, G.; Praetorius, D. Reliable and efficient a posteriori error estimation for adaptive IGA boundary element methods for weakly-singular integral equations, *Computer Methods in Applied Mechanics and Engineering*, 290:362–386, 2015.

[46] Fleming, J.L.; Wood, A.W.; Wood, W.D., Jr. Locally corrected Nyström method for EM scattering by bodies of revolution, *Journal of Computational Physics*, 196 (1):41–52, 2004.

[47] Gaul, L.; Kögl, M.; Wagner, M. *Boundary Element Methods for Engineers and Scientists: An Introductory Course with Advanced Topics*. Springer-Verlag, Berlin-Heidelberg-New York, 2003.

[48] Gedney, S.D. Application of the high-order Nyström scheme to the integral equation solution of electromagnetic interaction problems. In: *IEEE International Symposium on Electromagnetic Compatibility*, pages 289–294, 2000.

[49] Gedney, S.D.; Young, J.C. The locally corrected Nyström method for electromagnetics. In: Mittra, R., editor, *Computational Electromagnetics: Recent Advances and Engineering Applications*, chapter 5, pages 149–198, Springer New York, 2014.

[50] Gillman, A.; Hao, S.; Martinsson, P.G. A simplified technique for the efficient and highly accurate discretization of boundary integral equations in 2D on domains with corners, *Journal of Computational Physics*, 256:214–219, 2014.

[51] Gonzalez, O. On stable, complete, and singularity-free boundary integral formulations of exterior Stokes flow, *SIAM Journal on Applied Mathematics*, 69(4):933–958, 2009.

[52] Gonzalez, O.; Li, J. A convergence theorem for a class of Nyström methods for weakly singular integral equations on surfaces in $\mathbb{R}^3$, *Mathematics of Computation*, 84(292):675–714, 2015.

[53] Gu, J.; Zhang, J.; Li, G. Isogeometric analysis in BIE for 3-D potential problem, *Engineering Analysis with Boundary Elements*, 36(5):858–865, 2012.

[54] Guiggiani, M.; Gigante, A. A general algorithm for multidimensional Cauchy principal value integrals in the boundary element method, *Journal of Applied Mechanics-Transactions of the ASME*, 57(4):906–915, December 1990.

[55] Hao, S.; Barnett, A.H.; Martinsson, P.G.; Young, P. High-order accurate methods for Nyström discretization of integral equations on smooth curves in the plane, *Advances in Computational Mathematics*, 40(1):245–272, 2014.

[56] Harbrecht, H.; Peters, M. Comparison of fast boundary element methods on parametric surfaces, *Computer Methods in Applied Mechanics and Engineering*, 261–262: 39–55, 2013.

[57] Harbrecht, H.; Randrianarivony, M. From Computer Aided Design to wavelet BEM, *Computing and Visualization in Science*, 13(2):69–82, 2010.

[58] Hardwick, M.F.; Clay, R.L.; Boggs, P.T.; Walsh, E.J.; Larzelere, A.R.; Altshuler, A. DART system analysis. Technical Report SAND2005-4647, Sandia National Laboratories, 2005.

[59] Helsing, J. Integral equation methods for elliptic problems with boundary conditions of mixed type, *Journal of Computational Physics*, 228(23):8892–8907, 2009.

[60] Helsing, J.; Ojala, R. Corner singularities for elliptic problems: Integral equations, graded meshes, quadrature, and compressed inverse preconditioning, *Journal of Computational Physics*, 227(20):8820–8840, 2008.

[61] Heltai, L.; Arroyo, M.; DeSimone, A. Nonsingular isogeometric boundary element method for Stokes flows in 3D, *Computer Methods in Applied Mechanics and Engineering*, 268:514–539, 2014.

[62] Höllig, K.; Reif, U.; Wipper, J. Weighted extended B-spline approximation of Dirichlet problems, *SIAM Journal on Numerical Analysis*, 39(2):442–462, 2002.

[63] Höllig, K. *Finite Element Methods with B-Splines*, volume 26 of *Frontiers in Applied Mathematics*. SIAM, 2003.

[64] Höllig, K.; Reif, U. Nonuniform web-splines, *Computer Aided Geometric Design*, 20 (5):277–294, 2003.

[65] Höllig, K.; Hörner, J.; Hoffacker, A. Finite element analysis with B-splines: Weighted and isogeometric methods. In: Boissonnat, J.-D.; Chenin, P.; Cohen, A.; Gout, C.; Lyche, T.; Mazure, M.-L.; Schumaker, L., editors, *Curves and Surfaces*, volume 6920 of *Lecture Notes in Computer Science*, pages 330–350, Springer Berlin Heidelberg, 2012.

[66] Hughes, T.J.R.; Cottrell, J.A.; Bazilevs, Y. Isogeometric analysis: CAD, finite elements, NURBS, exact geometry and mesh refinement, *Computer Methods in Applied Mechanics and Engineering*, 194(39–41):4135–4195, October 2005.

[67] Khodakovsky, A.; Litke, N.; Schröder, P. Globally smooth parameterizations with low distortion, *ACM Transactions on Graphics*, 22(3):350–357, 2003.

[68] Kiendl, J.M. *Isogeometric Analysis and Shape Optimal Design of Shell Structures*. PhD thesis, Technische Universität München, 2010.

[69] Kim, H.-J.; Seo, Y.-D.; Youn, S.-K. Isogeometric analysis for trimmed CAD surfaces, *Computer Methods in Applied Mechanics and Engineering*, 198(37-40):2982–2995, 2009.

[70] Kim, H.-J.; Seo, Y.-D.; Youn, S.-K. Isogeometric analysis with trimming technique for problems of arbitrary complex topology, *Computer Methods in Applied Mechanics and Engineering*, 199(45–48):2796–2812, 2010.

[71] Kress, R. A Nyström method for boundary integral equations in domains with corners, *Numerische Mathematik*, 58(1):145–161, 1990.

[72] Kress, R. *Linear Integral Equations*, volume 82 of *Applied Mathematical Sciences*. Springer, Berlin, 3 edition, 2014.

[73] Lachat, J.C.; Watson, J.O. Effective numerical treatment of boundary integral equations: A formulation for three-dimensional elastostatics, *International Journal for Numerical Methods in Engineering*, 10:991–1005, 1976.

[74] Li, J.; Gonzalez, O. Convergence and conditioning of a Nyström method for Stokes flow in exterior three-dimensional domains, *Advances in Computational Mathematics*, 39(1):143–174, 2013.

[75] Li, K.; Qian, X. Isogeometric analysis and shape optimization via boundary integral, *Computer-Aided Design*, 43(11):1427–1437, 2011.

[76] Ligget, J.A.; Salmon, J.R. Cubic spline boundary elements, *International Journal for Numerical Methods in Engineering*, 17(4):543–556, 1981.

[77] Liu, Y.J.; Mukherjee, S.; Nishimura, N.; Schanz, M.; Ye, W.; Sutradhar, A.; Pan, E.; Dumont, N.A.; Frangi, A.; Saez, A. Recent advances and emerging applications of the boundary element method, *Applied Mechanics Reviews*, 64(3):030802-030802-38, 2011.

[78] Maniar, H.D. *A three dimensional higher-order panel method based on B-splines*. PhD thesis, Massachusetts Institute of Technology, 1995.

[79] Mantic, V. A new formula for the C-matrix in the Somigliana identity, *Journal of Elasticity*, 33:191–201, 1993.

[80] Marussig, B.; Duenser, C.; Beer, G. Isogeometric boundary element methods for tunneling. In: *Symposium of the International Association for Boundary Element Methods, IABEM 2013*, pages 100–106, 2013.

[81] Marussig, B.; Beer, G.; Duenser, C. Isogeometric boundary element method for the simulation in tunneling, *Applied Mechanics and Materials*, 553:495–500, 2014.

[82] Marussig, B.; Zechner, J.; Beer, G.; Fries, T.-P. Fast isogeometric boundary element method based on independent field approximation, *Computer Methods in Applied Mechanics and Engineering*, 284:458–488, 2015.

[83] Marussig, B.; Zechner, J.; Beer, G.; Fries, T. Fast isogeometric boundary element method based on independent field approximation, *CoRR*, arXiv:1406.0306v3 [cs.NA], 2015.

[84] Mathews, J.H. Module for horner's method, 9 2015. URL `http://mathfaculty.fullerton.edu/mathews/n2003/HornerMod.html`.

[85] May, S.; Kästner, M.; Müller, S.; Ulbricht, V. A hybrid IGAFEM/IGABEM formulation for two-dimensional stationary magnetic and magneto-mechanical field problems, *Computer Methods in Applied Mechanics and Engineering*, 273:161–180, 2014.

[86] McLean, W. *Strongly Elliptic Systems and Boundary Integral Equations*. Cambridge University Press, Cambridge, 2000.

[87] Nagy, A.P.; Benson, D.J. On the numerical integration of trimmed isogeometric elements, *Computer Methods in Applied Mechanics and Engineering*, 284:165–185, 2015.

[88] Nyström, E.J. Über die praktische Auflösung von linearen Integralgleichungen mit Anwendungen auf Randwertaufgaben der Potentialtheorie, *Acta Mathematica*, 54(1): 185–204, 1930.

[89] Parreira, P. On the accuracy of continuous and discontinuous boundary elements, *Engineering Analysis*, 5(4):205–211, 1988.

[90] Patterson, C.; Sheikh, M.A. Interelement continuity in the boundary element method. In: Brebbia, C.A., editor, *Topics in Boundary Element Research*, chapter 6, pages 123–141, Springer US, 1984.

[91] Peake, M.J.; Trevelyan, J.; Coates, G. Extended isogeometric boundary element method (XIBEM) for two-dimensional Helmholtz problems, *Computer Methods in Applied Mechanics and Engineering*, 259:93–102, 2013.

[92] Peterson, A.F.; Bibby, M.M. *An Introduction to the Locally-Corrected Nyström Method*. Synthesis Lectures on Computational Electromagnetics Morgan & Claypool, 2009.

[93] Piegl, L.; Tiller, W. *The NURBS Book*. Springer, New York, 2 edition, 1997.

[94] Politis, C.; Ginnis, A.I.; Kaklis, P.D.; Belibassakis, K.; Feurer, C. An isogeometric BEM for exterior potential-flow problems in the plane. In: *SIAM/ACM Joint Conference on Geometric and Physical Modeling*, SPM '09, pages 349–354, 2009.

[95] Rank, E.; Ruess, M.; Kollmannsberger, S.; Schillinger, D.; Düster, A. Geometric modeling, isogeometric analysis and the finite cell method, *Computer Methods in Applied Mechanics and Engineering*, 249–252:104–115, 2012.

[96] Rivas, F.; Valle, L.; Cátedra, M. A moment method formulation for the analysis of wire antennas attached to arbitrary conducting bodies defined by parametric surfaces, *Applied Computational Electromagnetics Society Journal*, 11(2):32–39, 1996.

[97] Rogers, D.F. *An Introduction to NURBS: With Historical Perspective*. Morgan Kaufmann, San Francisco, 2001.

[98] Rüberg, T. Stabilisation of a B-splines basis. Working notes, 11 2014.

[99] Rüberg, T.; Cirak, F. Subdivision-stabilised immersed b-spline finite elements for moving boundary flows, *Computer Methods in Applied Mechanics and Engineering*, 209–212(0):266–283, 2012.

[100] Saranen, J. The convergence of even degree spline collocation solution for potential problems in smooth domains of the plane, *Numerische Mathematik*, 53(5):499–512, 1988.

[101] Saranen, J.; Wendland, W.L. On the asymptotic convergence of collocation methods with spline functions of even degree, *Mathematics of Computation*, 45(171):91–108, 1985.

[102] Sauter, S.A.; Schwab, C. *Boundary Element Methods*, volume 39 of *Springer Series in Computational Mathematics*. Springer Berlin Heidelberg, 2011.

[103] Schillinger, D.; Dedè, L.; Scott, M.A.; Evans, J.A.; Borden, M.J.; Rank, E.; Hughes, T.J.R. An isogeometric design-through-analysis methodology based on adaptive hierarchical refinement of NURBS, immersed boundary methods, and T-spline CAD surfaces, *Computer Methods in Applied Mechanics and Engineering*, 249–252:116–150, 2012.

[104] Schlemmer, E.; Rucker, W.M.; Richter, K.R. Boundary element computations of 3D stationary and time-dependent problems using Bézier-spline elements, *IEEE Transactions on Magnetics*, 30(5):2901–2906, 1994.

[105] Schmidt, G. On ε-Collocation for pseudodifferential equations on a closed curve, *Mathmatische Nachrichten*, 126:183–196, 1986.

[106] Schmidt, R.; Kiendl, J.; Bletzinger, K.-U.; Wüchner, R. Realization of an integrated structural design process: analysis-suitable geometric modelling and isogeometric analysis, *Computing and Visualization in Science*, 13:315–330, 2010.

[107] Schmidt, R.; Wüchner, R.; Bletzinger, K.-U. Isogeometric analysis of trimmed NURBS geometries, *Computer Methods in Applied Mechanics and Engineering*, 241–244:93–111, 2012.

[108] Schneider, R. Stability of a spline collocation method for strongly elliptic multidimensional singular integral equations, *Numerische Mathematik*, 58(8):855–873, 1991.

[109] Scott, M.A.; Simpson, R.N.; Evans, J.A.; Lipton, S.; Bordas, S.P.A.; Hughes, T.J.R.; Sederberg, T.W. Isogeometric boundary element analysis using unstructured T-splines, *Computer Methods in Applied Mechanics and Engineering*, 254:197–221, 2013.

[110] Scott, M.A. *T-splines as a design-through-analysis technology*. PhD thesis, University of Texas at Austin, 2011.

[111] Sederberg, T.W.; Zheng, J.; Bakenov, A.; Nasri, A. T-splines and T-NURCCs, *ACM Transactions on Graphics*, 22(3):477–484, 2003.

[112] Simpson, R.N.; Bordas, S.P.A.; Trevelyan, J.; Rabczuk, T. A two-dimensional isogeometric boundary element method for elastostatic analysis, *Computer Methods in Applied Mechanics and Engineering*, 209–212:87–100, 2012.

[113] Simpson, R.N.; Scott, M.A.; Taus, M.; Thomas, D.C.; Lian, H. Acoustic isogeometric boundary element analysis, *Computer Methods in Applied Mechanics and Engineering*, 269:265–290, 2014.

[114] Sloan, I.H. Analysis of general quadrature methods for integral equations of the second kind, *Numerische Mathematik*, 38(2):263–278, 1981.

[115] Sloan, I.H. Error analysis of boundary integral methods, *Acta Numerica*, 1:287–339, 1992.

[116] Steinbach, O. *Numerical Approximation Methods for Elliptic Boundary Value Problems: Finite and Boundary Elements*. Springer, New York, 2008.

[117] Strain, J. Locally corrected multidimensional quadrature rules for singular functions, *SIAM Journal on Scientific Computing*, 16(4):992–1017, 1995.

[118] Takahashi, T.; Matsumoto, T. An application of fast multipole method to isogeometric boundary element method for Laplace equation in two dimensions, *Engineering Analysis with Boundary Elements*, 36(12):1766–1775, 2012.

[119] Tausch, J. Nyström discretization of parabolic boundary integral equations, *Applied Numerical Mathematics*, 59(11):2843–2856, 2009.

[120] Thurston, W.P. Three dimensional manifolds, kleinian groups and hyperbolic geometry, *Bulletin (New Series) of the American Mathematical Society*, 6(3):357–381, 1982.

[121] Tong, M.S.; Chew, W.C. Nyström method for elastic wave scattering by three-dimensional obstacles, *Journal of Computational Physics*, 226(2):1845–1858, 2007.

[122] Turco, E.; Aristodemo, M. A three-dimensional B-spline boundary element, *Computer Methods in Applied Mechanics and Engineering*, 155(1-2):119–128, 1998.

[123] Ushatov, R.; Power, H.; Rêgo Silva, J. Uniform bicubic B-splines applied to boundary element formulation for 3-D scalar problems, *Engineering Analysis with Boundary Elements*, 13(4):371–381, 1994.

[124] Valle, L.; Rivas, F.; Catedra, M. Combining the moment method with geometrical modeling by NURBS surfaces and Bézier patches, *IEEE Transactions on Antennas and Propagation*, 42(3):373–381, 1994.

[125] Vazquez, R.; Buffa, A.; Di Rienzo, L. NURBS-based BEM implementation of high-order surface impedance boundary conditions, *IEEE Transactions on Magnetics*, 48 (12):4757–4766, 2012.

[126] Vuong, A.-V.; Giannelli, C.; Jüttler, B.; Simeon, B. A hierarchical approach to adaptive local refinement in isogeometric analysis, *Computer Methods in Applied Mechanics and Engineering*, 200(49–52):3554–3567, 2011.

[127] Wang, Y.-W.; Huang, Z.-D.; Zheng, Y.; Zhang, S.-G. Isogeometric analysis for compound B-spline surfaces, *Computer Methods in Applied Mechanics and Engineering*, 261–262:1–15, 2013.

[128] Wang, Y.; Benson, D.J.; Nagy, A.P. A multi-patch nonsingular isogeometric boundary element method using trimmed elements, *Computational Mechanics*, 56(1):173–191, 2015.

[129] Watson, J.O. Boundary elements from 1960 to the present day, *Electronic Journal of Boundary Elements*, 1(1):34–46, 2003.

[130] Ying, L.; Zorin, D. A simple manifold-based construction of surfaces of arbitrary smoothness, *ACM Transactions on Graphics*, 23(3):271–275, 2004.

[131] Ying, L.; Biros, G.; Zorin, D. A high-order 3D boundary integral equation solver for elliptic PDEs in smooth domains, *Journal of Computational Physics*, 219(1):247–275, 2006.

[132] Yu, M.; Kuffel, E. Spline element for boundary element method, *IEEE Transactions on Magnetics*, 30(5):2905–2907, 1994.

[133] Zechner, J.; Marussig, B.; Beer, G.; Duenser, C.; Fries, T.-P. Isogeometric boundary element method with hierarchical matrices. In: *11th World Congress on Computational Mechanics, WCCM 2014, 5th European Conference on Computational Mechanics, ECCM 2014 and 6th European Conference on Computational Fluid Dynamics, ECFD 2014*, pages 2457–2468, 2014.

[134] Zechner, J.; Marussig, B.; Beer, G.; Fries, T.-P. The isogeometric Nyström method, *CoRR*, arXiv:1506.03914 [cs.NA], 2015.

[135] Zechner, J. *A Fast Boundary Element Method with Hierarchical Matrices for Elastostatics and Plasticity*. PhD thesis, Graz University of Technology, 2012.